DISSERTATION

DENSITY FUNCTIONAL THEORY AND GREEN'S FUNCTION APPROACH TO INVESTIGATE CADMIUM TELLURIDE BASED THIN FILM PHOTOVOLTAICS

Submitted by

Anthony P. Nicholson

Department of Mechanical Engineering

In partial fulfillment of the requirements

For the Degree of Doctor of Philosophy

Colorado State University

Fort Collins, Colorado

Summer 2020

Doctoral Committee:

Advisor: Walajabad S. Sampath
Co-Advisor: Chris Weinberger

Ketul Popat
James Sites
Umberto Martinez

ABSTRACT

DENSITY FUNCTIONAL THEORY AND GREEN'S FUNCTION APPROACH TO INVESTIGATE CADMIUM TELLURIDE BASED THIN FILM PHOTOVOLTAICS

In recent years, cadmium telluride (CdTe) based thin film photovoltaics (PV) have exhibited remarkable improvements in overall efficiency and device performance. As the most notable thin film PV technology, CdTe PV is developed and manufactured in the U.S. as the leading cost-competitive option for electricity generation in comparison to other PV technologies such as silicon and CIGS PV. However, CdTe PV faces major challenges that limit its achievable performance during the solar energy conversion process. It has become increasingly evident that to improve PV efficiency, an understanding of surfaces and interfaces is necessary. Therefore, high-fidelity quantum-based atomistic simulations will be used to calculate energy band alignment of CdTe thin film surfaces and interfaces to resolve the issues found in such problematic areas and advance PV efficiency. *Ab initio* simulation models will implement density functional theory (DFT) coupled with Green's function (GF) for investigating the electronic and structural properties of thin film surfaces and interfaces within CdTe PV device configurations. Comprehensive studies on spatially-dependent energy band alignments with respect to plane orientation, terminated surfaces, carrier concentrations and elemental composition were computationally evaluated to determine their possible effect on CdTe solar cell device performance. A total of 14 unique CdTe-based surfaces and 3 different CdTe/Te interfaces were simulated to determine their effect on energy band alignment. A number of key insights were gained that include: 1) the band bending directions dictated by the termination layer based on surface theory; 2) the role of surface reconstruction in flattening the CdTe surface energy band alignments while neutralizing surface states due to the fulfillment of the electron counting rule; 3) the formation of a cusp energy potential feature along the CdTe{111} plane oriented energy band alignments as observed by external literature studies

within the CdTe/Te interface. Results to date indicate that the DFT+GF atomistic modeling approach to constructing energy band alignments matches closer to experiments than conventional band alignment methods. State-of-the-art DFT+GF calculations on CdTe-based thin film surfaces and interfaces provide a methodology for studying quantum mechanical effects in thin film PV devices such as high-efficiency single junction CdTe solar cells and tandem solar cells.

ACKNOWLEDGEMENTS

The current research is based upon work supported by the National Science Foundation Graduate Research Fellowship Program under Grant No. DGE-1321845, INTERN Program under Grant No. 1540007, and Industry-University Cooperative Research Centers Program under Grant No. 1821526. Any opinions, findings, and conclusions or recommendations expressed in this material are those of the author(s) and do not necessarily reflect the views of the National Science Foundation. This work utilized the Summit supercomputer, which is supported by the National Science Foundation (awards ACI-1532235 and ACI-1532236), the University of Colorado Boulder, and Colorado State University. The Summit supercomputer is a joint effort of the University of Colorado Boulder and Colorado State University.

I would personally like to thank my co-advisors Prof. Walajabad Sampath and Prof. Chris Weinberger for their expertise and willingness to help me understand concepts related to CdTe photovoltaics, materials science, and first-principles computational modeling. My gratitude is given to Prof. James Sites for his thought-provoking discussions on photovoltaic device physics and interactions during our weekly research meetings. I am thankful as well to Prof. Jose de la Venta for providing me with his instructive lectures in the Introduction to Solid State Physics course. I am also grateful to Prof. Ketul Popat for taking the time to provide critique on my research work. I am deeply appreciative to Umberto Martinez for his mentorship and patience throughout my Ph.D. research. His contribution to our DFT research group's progress would not have been at all possible without him. I also wanted to extend my thanks and greetings to all employees at Synopsys Denmark for providing our research group with such an invaluable computational modeling software package as QuantumATK. A humbled thank you goes out to Prof. Ken Durose from the University of Liverpool for his key insight on the importance of surface polarity in CdTe surfaces. I would like to thank my DFT colleagues Aanand Thiyagarajan and Akash Shah for the thought-provoking discussions and support along the research journey. I also want to give a special thanks to Dr. Amit Munshi and Dr. Tushar Shimpi for their willingness to generate interesting discussions and

share their experimental findings on CdTe-based PV devices. I give a big thanks to all my fellow research colleagues in the CSU PV lab and all my collaborators. I want to give a special thank you to everyone involved in the development of the LaTeX-based package for writing my dissertation. I want to warmly thank my parents Patrick and Dora as well as other family and friends for their support along the way. Most of all, I want to thank my God Jehovah for always being there when I need him most, for teaching me to stay focused on the "more important things", and making known his Grand Sovereignty over the entire universe to time indefinite.

TABLE OF CONTENTS

LIST OF TABLES

LIST OF FIGURES

LIST OF DFT TERMS

Kohn-Sham	Single-particle representation of the Schrödinger equation that is used in the DFT calculations.
Basis Set	Set of functions that describe the wavefunction of an electron (eigenstates) within the KS representation of the system. For LCAO representations of DFT, the basis functions are defined as atomic orbitals and are dictated by size, range, and shape.
Density Mesh Cutoff	Value used to determine the grid spacing of the real-space representation of the simulation domain that controls numerical accuracy of a calculation.
k-points	Sampling points of the Brillouin zone in reciprocal space of the simulation domain that directly influence the accuracy of the converged solution for total energy.
Pseudopotential	A modified weaker potential that replaces the Coulomb potential of electrons near the atomic nuclei that creates the same screening effect that the core electrons had on the valence electrons.
Hartree Potential	A classical description of the electrostatic interactions between electrons within the KS formulation.
Exchange-Correlation	Regarding exchange-correlation functional, it is the term that accounts for the quantum mechanical nature of interactions between electrons within the KS formulation.
(Projected) Bandstructure	Bandstructure describes the electronic levels that an electron can exist for a given crystal structure. The bands are plotted within the first Brillouin zone of reciprocal space along high symmetry k-point directions. "Projected" bandstructure plots the bands with respect to orbitals as represented by a visual color scheme.
Geometry Optimization	Minimization of the forces acting on the selected atoms within the geometry optimization region. After GO, the SCF convergence is more stable as the system has reached a lower local minima for total energy than prior to GO. DFT+GF surface and interface calculations were conducted without and with GO to evaluate the effects of relaxation on the regions of interest.

Projected Local Density of States An analysis feature in QuantumATK that plots the density of states in an energy vs. distance format to easily visualize the energy band alignment of the calculation. PLDOS is constructed as the averaged projection of the device density of states along the longest part of the simulation domain, resulting in the energy band alignment representation of both the surface (one-probe) and interface (two-probe) models.

Mulliken Population An analysis feature in QuantumATK that displays the electron charge for a given atomic species in the system and is simply another representation of the electron density. The Mulliken charge on the atoms themselves and/or the charge present within the bonding arrangement is taken from the Mulliken population analysis.

Hartree Difference Potential An analysis feature in QuantumATK that quantifies the difference between the evaluated Hartree potential of the converged system at point $\mathbf{r}$ to the Hartree potential of a neutral atom in the same location $\mathbf{r}$.

LIST OF EQUATION TERMS

Equation	Term	Description
(1.1)	ΔE_C	Conduction band offset
	q	Electronic charge
	$\chi_{1,2}$	Electron affinity of material $1, 2$
(1.2)	ΔE_g	Band gap energy difference between thin film layers
	ΔE_V	Valence band offset
(1.3)	$f_0(E)$	Fermi-Dirac probability
	E_F	Fermi energy level
	k_B	Boltzmann constant
	T	Temperature
(2.1)	m_e	Electron effective mass
	M_I	Nuclei mass
	$\mathbf{r_i}$, $\mathbf{r_j}$	Coordinate position of electron i, j
	$\mathbf{R_I}$, $\mathbf{R_J}$	Coordinate position of nuclei I, J
	Z_I, Z_J	Atomic numbers for atoms I, J
	Ψ	Many-body wavefunction
	E_{tot}	Ground-state total energy of many-body system
(2.2)	$V_H(\mathbf{r})$	Hartree potential
	$V_n(\mathbf{r})$	Electron-ion and external potential
	$V_{xc}(\mathbf{r})$	Exchange-Correlation potential
	$\phi_i(\mathbf{r})$	Single-particle wavefunction i
	ϵ_i	Ground-state total energy of single-particle i
(2.3)	E_{GS}	Ground-state total energy for Kohn-Sham formulation
	$n(\mathbf{r})$	Electron density at position r
	$E_{xc}[n]$	Exchange-Correlation energy
(2.4)	$\phi_{Inlm}(\mathbf{r})$	LCAO basis set of atomic site I where n, l, m denote respective principle, angular, and magnetic quantum numbers
	$R_{Iln}(\lvert\mathbf{r_I}\rvert)$	Radial part of basis set in LCAO representation
	$Y_{lm}(\hat{\mathbf{r}}_\mathbf{I})$	Spherical harmonic part of basis set in LCAO representation
(2.5)	$\phi_i(\mathbf{r})$	Basis set within LCAO representation
	c_ν	Non-orthogonal coefficient at composite index ν
	$\varphi_\nu(\mathbf{r})$	Compact notation of basis function

(2.6)	$\mathcal{H}$	Hamiltonian matrix
	$\mathcal{S}$	Overlap matrix
(2.7)	$E_{xc}^{LDA}[n]$	Exchange-Correlation energy functional based on local density approximation
	$\epsilon_{xc}^{unif}(n(\mathbf{r}))$	Exchange-Correlation energy functional of a homogeneous electron gas
(2.8)	$E_{xc}^{GGA}[n]$	Exchange-Correlation energy functional based on generalized gradient approximation
(2.9)	E_U	Hubbard-U energy
	U_μ	On-site Coulomb repulsion energy
	n_μ	Projection onto atomic shell μ
(3.1)	$V(z)$	Electrostatic potential at position z from the surface
	N_A	Number of ionized acceptors in a p-type semiconductor
	ϵ	Dielectric constant of p-type semiconductor
	z_{dep}	Depletion width measured from the surface
(4.1)	γ_{int}	Interfacial energy
	$E_{tot,int}$	Total energy of the interface system
	$E_{tot,CdTe}$	Total energy of the bulk CdTe system
	$N_{cr,CdTe}$	Number of equivalent CdTe unit cells in central region
	$N_{bulk,CdTe}$	Equivalent CdTe unit cell forming left bulk electrode
	$E_{tot,Te}$	Total energy of the bulk Te system
	$N_{cr,Te}$	Number of equivalent Te unit cells in central region
	$N_{bulk,Te}$	Equivalent Te unit cell forming right bulk electrode

PHYSICAL CONSTANTS

Reduced Planck's Constant	$\hbar = 1.05457180 \times 10^{-34}$ J-s
Boltzmann Constant	$k = 1.38064852 \times 10^{-34}$ J-K^{-1}
Elementary Charge	$e = 1.60217662 \times 10^{-19}$ C
Vacuum Permittivity	$\epsilon_0 = 8.85418781 \times 10^{-12}$ F-m^{-1}

Chapter 1

Introduction

Energy sustainability constitutes one of the grand challenges facing modern society. The energy generated from fossil fuels and other environmentally harmful sources are not considered sustainable options. That is why various sustainable energy systems are being investigated and developed to determine which ones are easily accessible, abundant and affordable while at the same time minimizing their environmental impact. This does not limit the energy demands associated with the possible options to only affluent populations. Rather, energy demands should be addressed for both developed and developing countries across the globe. One suitable candidate that meets the crucial standards for energy sustainability is solar renewable energy.

In recent years, solar renewable energy generated by photovoltaic (PV) systems has manifested itself as an essential contributor to the initiative for global-scale electricity generation. The Sun is an abundant energy resource with enormous harnessing potential, ideally suited to meet all consumer energy demands. It has been estimated that the Sun provides enough energy on Earth for the entire annual global energy consumption in approximately one hour. Despite such a promising energy source, the greatest issue has been to develop optimized PV technologies capable of harnessing a majority of the incoming energy from the Sun and efficiently convert it into useful energy. Much effort in the 20th and 21st centuries has focused on addressing the limitations in solar energy conversion efficiency, which has led to remarkable improvements in solar energy technologies. Today, the solar energy industry continues to make new efficiency breakthroughs and develop innovative processes that advance existing PV technologies while paving the way for new ones.

Substantial growth in the production and deployment of PV systems suggest that solar renewable energy will continue to be economically feasible for years to come. Current PV installations due to manufacturing-scale implementations have significantly decreased the cost of PV electricity generation. As a result, general forecasts for new PV installation capacity reveal that more than 100 Gigawatts (GW) were installed in 2018 [1, 2] and are expected to increase through 2023 as shown

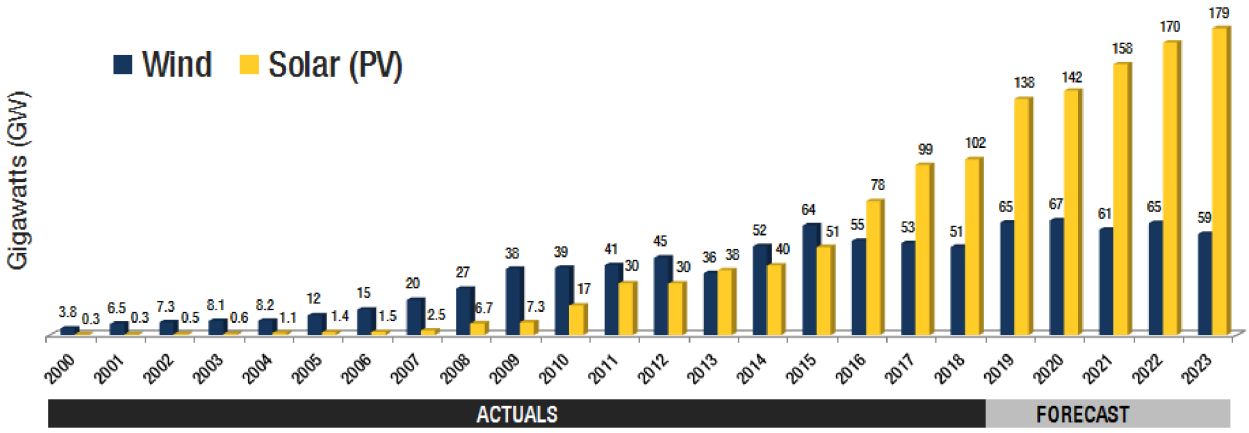

Figure 1.1: Newly installed PV capacity on an annual basis with actual data extending up to 2017. Projected forecasts from 2018 to 2023 are also included (taken from [5]);

in Figure 1.1. Another report in 2017 has shown a continuous declination of the unsubsidized levelized cost of energy (LCOE) prices as low as $0.04 per Kilowatt-Hour (kWh) for utility-scale solar technologies [3]. In terms of future growth, PV global capacity is projected to reach nearly 10 Terawatts (TW) by 2030 while achieving upwards of 30 to 70 TW by 2050 [4]. The future outlook for PV technologies is not merely a conceptualized idea but rather a proven result from the current trends demonstrated within the PV energy market.

The very low environmental impact and increased accessibility of PV technologies further indicate how solar renewable energy can improve the quality and standard of living in various ways. The environmental life-cycle assessment between PV and conventional energy systems reveals that PV produces significantly less greenhouse gas emissions, toxic emissions and heavy metal emissions than conventional power generation technologies [6]. Furthermore, strategic assessments such as the SunShot initiative developed by the U.S. Department of Energy (DOE) show the environmental and health benefits stemming from PV installations in the U.S. [7] Lastly, the modular design of PV technologies allow it to be deployed and operated in a range of locations and climate conditions that are not easily accessible. It is evident that PV systems ensure the health and environmental safety of energy consumers while facilitating their accessibility to energy resources.

Solar PV is redefining the standards for electricity generation throughout the planet. As an abundant and clean renewable energy source, PV will continue to see significant growth in the

energy market. The vast economic and environmental benefits demonstrated by PV technologies confirm the viability of solar renewable energy as a promising energy contributor worldwide. However, very few PV technologies have consistently maintained good efficiencies, developed achievable goals for increased device performance, and expanded their production to utility-scale sizes. One specific PV technology that successfully addresses these requirements while fulfilling the electricity generation demands is known as cadmium telluride (CdTe) based thin film PV. The overall purpose of this work is to explore important details within CdTe thin film PV devices that will further improve its usage as a leading PV technology for electricity generation.

1.1 Cadmium Telluride Thin Film PV

1.1.1 A Present Glance

Thin film PV technologies incorporating the CdTe semiconductor compound have proven to be advantageous for a number of reasons that include: 1) lower utility-scale production cost [3], 2) exceptional reliability compared to other solar cell materials such as crystalline silicon [8], 3) reduced environmental impacts throughout its entire life-cycle process [6], and 4) increased module efficiency from 9 to 18% within the last decade [9]. As shown in Figure 1.2, CdTe PV is economically competitive in relation to fossil fuels with a LCOE between \$0.03 and \$0.06/kWh as projected by the most notable CdTe manufacturing company First Solar Inc. (FSLR) [10]. FSLR alone by 2018 has installed more than 17 GW of solar capacity worldwide and characterizes how quickly the solar technology is expanding. CdTe PV is also among the few PV technologies exhibiting well-behaved long-term power generation performance within climate zones that have high potential to degrade them [8, 11]. The recent success seen in CdTe PV is now enabling new ways to explore innovative system solutions such as economically advantageous building integrated PV systems [12] and solar mobility within the transportation sector [1]. From the few highlighted points, it is evident that CdTe thin film PV is a cost competitive technology and viable solution for energy sustainability.

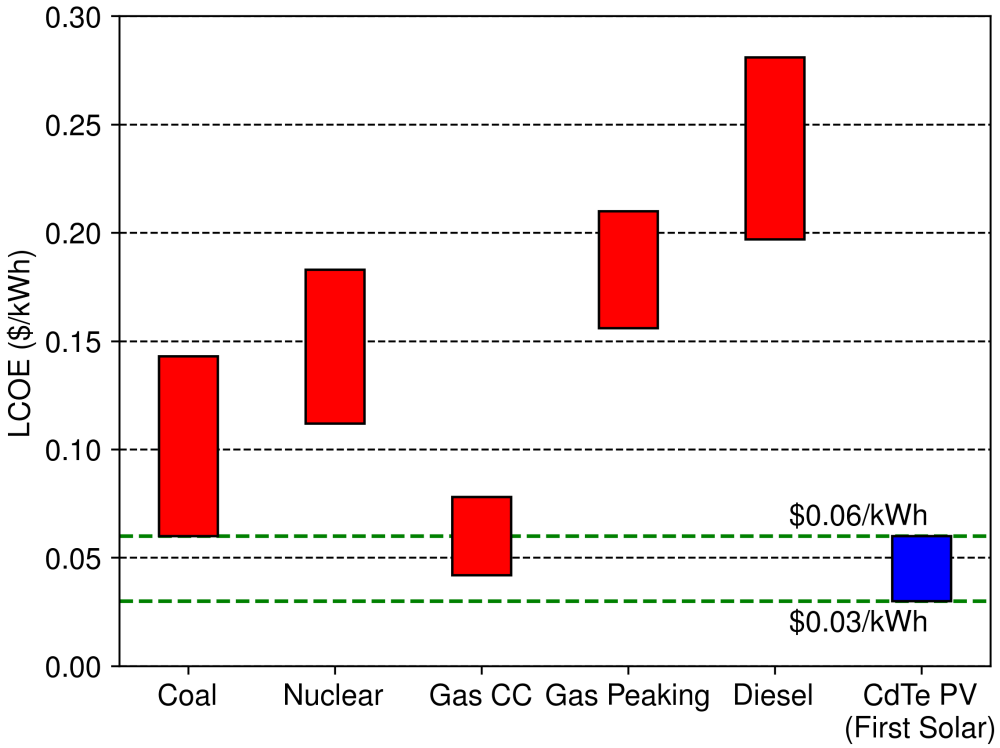

Figure 1.2: LCOE for utility-scale CdTe PV (FSLR) in comparison to fossil fuel electricity costs (data taken from [3, 10]).

A well-established and repeatable process is necessary for each thin film layer incorporated in the CdTe PV device to work together as intended. CdTe solar cell fabrication processes have developed over time to include sequential deposition of layers, passivation treatments, post-annealing, doping, and contacting that yield rapidly increasing CdTe cell efficiencies [13]. The typical research-grade CdTe solar cell structure includes a glass superstrate with a transparent conductive oxide, window layer, p-type CdTe absorber layer, and a back electrode for completing the device. Arguably the most important step to the fabrication process is the cadmium chloride passivation treatment since without it the CdTe device efficiency is severely compromised [14–17]. Other notable additions such as the replacement of the cadmium sulfide window layer with a magnesium zinc oxide (MZO) buffer layer [18, 19] and the use of a tellurium back-contact have led to further CdTe PV device improvements as well. An example of a typical CdTe PV device con-

figuration, but certainly not the most optimized device structure to-date, is provided in Figure 1.3. Advancements to CdTe PV technology have led to the highest recorded CdTe efficiency of 22.1% achieved by FSLR [20]. At Colorado State University, thin film CdTe-based PV device efficiencies of 19.2% have been achieved and are the highest outside of FSLR. However, there still remains to be seen much improvement to the CdTe device performance as predicted by the upper theoretical CdTe efficiency of ~32-33% derived from the Shockley-Queisser limit [21]. Several limitations throughout the CdTe PV device are currently being addressed in the CdTe solar community in an effort to optimize the device structure. A brief description follows on the initiative for higher thin film CdTe PV efficiencies.

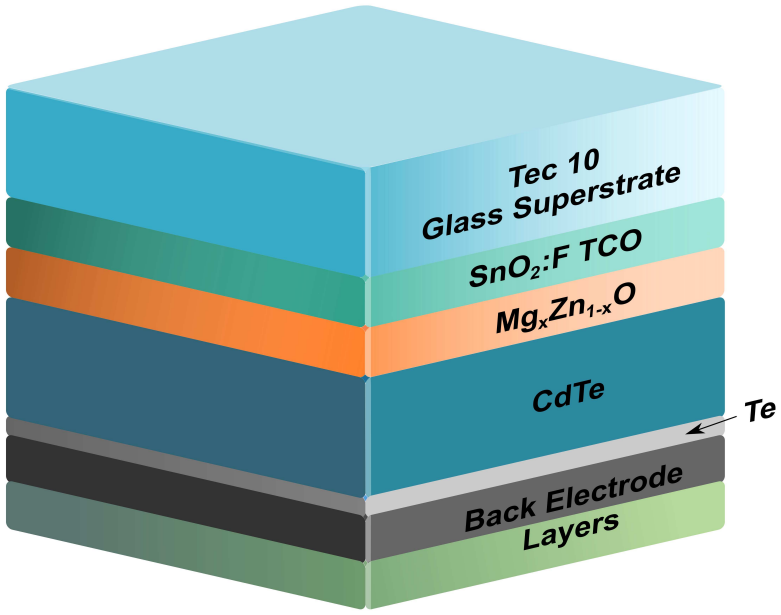

Figure 1.3: Illustration of a typical CdTe PV device superstrate configuration (not to scale).

1.1.2 Research Initiatives

The general PV community has developed technological roadmaps that evaluate the challenges in solar renewable energy while identifying possible solutions to progress the technology. One major initiative for developing solar energy capacity in the U.S. is known as the DOE SunShot

goal. With CdTe PV being one of the primary technologies leading the DOE SunShot goal, it has become crucial for researchers to find ways to enhance CdTe PV device efficiencies. A survey published in 2018 by DOE's Office of Energy Efficiency & Renewable Energy [22] reports multiple technical challenges that need to be addressed within the CdTe-based PV technology. The scope of these challenges focuses on various functional areas throughout the solar cell such as absorbers, defects, surface passivation and interfaces. Much progress has been made on absorbers with the implementation of $CdSe_xTe_{1-x}$ layers for higher current collection [23, 24] and promising group V dopants such as arsenic [25, 26]. As the overall bulk characteristics of CdTe-based solar cells improve, surface passivation and interfacial behaviors are expected to play a greater role in the journey toward CdTe PV efficiencies greater than 25% [27].

Surfaces and interfaces are both complex and interesting regions that can easily influence the overall CdTe efficiency. The electronic properties seen in both areas often dictate the semiconductor device physics within the CdTe PV device. However, a detailed description of the mechanisms causing such losses within surfaces and interfaces are not completely understood. The DOE survey has categorized several key, yet under-utilized, computational techniques that are expected to aid in the understanding of the science and engineering behind PV surfaces and interfaces. Among them is atomistic modeling, a high-fidelity computational technique directly applicable to many of the problem areas outlined in the DOE survey. Atomistic modeling based on quantum mechanics enables are more accurate description of electronic features such as energy band alignment within CdTe PV surfaces and interfaces. Energy band alignment in CdTe solar cells is of upmost importance for interpreting and predicting how devices will behave under certain conditions. That is why the use of atomistic modeling to calculate energy band alignments is essential to the advancement of solar energy technologies within the PV research community and industry as a whole.

1.2 Theoretical Energy Band Alignment in CdTe PV

The overall device performance of PV technologies is dependent upon the electronic and structural properties that make up the energy band alignment diagram throughout the entire device. The

energy band alignment governs the charge transport phenomena seen in thin film heterostructures, so it is essential that the physical concepts encompassing band alignment construction are accurately described across the thin film regions. Solid state physics states that since there are a large number of atoms in the thin film layer, the small interatomic distances between atoms relative to the spatial extensions of their discrete energy levels leads to interactions of the energy states. These interactions of states eventually "split" into allowed energy bands with a forbidden energy zone in between so as to obey the Pauli exclusion principle [28]. In semiconductor materials, the resulting forbidden energy region where no electrons can exist due to splitting of the bands is called the band gap. The valence band (VB) denotes an allowed energy band that contains all valence electrons at T = 0 K. The conduction band (CB) describes the allowed energy band where electrons can go when they are thermally excited (T > 0 K) at an energy greater than the band gap energy width.

The energy band alignment of interfaces developed between two dissimilar thin film layers becomes quite a unique challenge as there are many complex characteristics involved at the junction. A number of theoretical band alignment models have been conceived over the years [29], one of which being the most commonly used known as the Anderson Rule [30] or Electron Affinity Rule [31]. The Anderson Rule conceptualizes the idea that the band alignment is determined by the electron affinity χ (or work function if the material is a metal) of both layers as referenced from vacuum level. The electron affinities can be used to determine the conduction band offset ΔE_C and is given as:

$$\Delta E_C = q\left(\chi_2 - \chi_1\right) \tag{1.1}$$

where q is simply the electronic charge. As long as the band gaps E_{g_1} and E_{g_2} are known, then construction of the band alignment at the interface obeys the following simple relation expressed in (1.2):

$$\Delta E_g = \Delta E_C + \Delta E_V \tag{1.2}$$

where ΔE_g and ΔE_V are the differences in band gap as well as the valence band offset between the two layers. ΔE_V can be thus easily calculated by the difference between ΔE_g and ΔE_C. Equation (1.2) is a simplistic attempt to construct a band diagram using only band offsets of the materials but remains the common option for making energy band diagrams of heterostructures.

Before creating a band diagram at equilibrium via the Anderson Rule, an important concept that relates to the occupancy of quantum states within the VB and CB needs to be included in the equilibration process. The Fermi-Dirac probability function derived from statistical mechanics defines the probability of finding an electron somewhere in the VB or CB and is dependent upon the energy of the occupied state as well as the temperature of the system. The Fermi-Dirac function for electrons in the case of non-degenerate semiconductors is defined as:

$$f_0(E) = \frac{1}{1 + e^{(E-E_F)/k_B T}} \tag{1.3}$$

where E_F is the Fermi level, k_B is the Boltzmann constant, and T is temperature within the semiconductor material. The Fermi level E_F is the energy level at which the probability of an electron occupying a quantum state is 1 at T = 0 K and 1/2 at T > 0 K. If two thin film layers are semiconductors, then the Fermi level E_F of each semiconductor (or more generally the chemical potential μ [32] of the thin film layer) needs to be determined before the Anderson Rule can be applied to the heterostructure. The Fermi level is influenced by p or n-type carrier concentrations resulting from intrinsic or extrinsic (i.e. impurity doping) effects within the semiconductor layers and thus change the Fermi-Dirac probability function.

Once all the important values above are obtained, the Anderson Rule then constructs the band alignment in four steps [33]:

1. Place the band energy values of the thin film layers on a common vacuum level prior to equilibration

2. Create a flat Fermi level joined between the two layers to denote the completion of equilibrium

3. Adjust the band offset energy positions in relation to the doping ratio that exists between the two layers

4. Connect the band edges of both layers starting with the majority carrier related band edges first and then the remaining band edges

Figure 1.4 has been adapted from [33] and shows the steps in a schematic format for band alignment of a CdTe absorber layer and a Te back contact layer. Using experimental band gap E_g values for CdTe and Te of 1.49 and 0.33 eV, respectively [34], and a valence band offset ΔE_V of 0.50 eV [33], the conduction band offset can be calculated with (1.2) to construct the theoretical CdTe/Te band diagram.

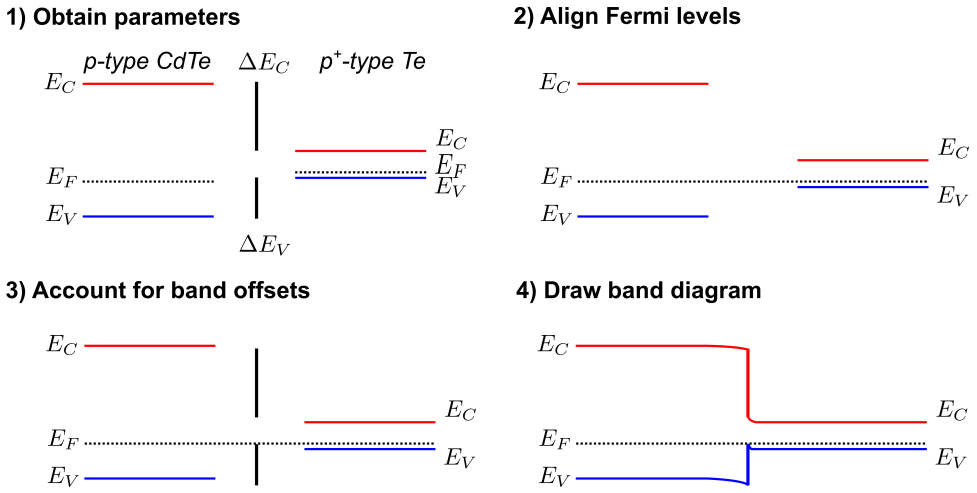

Figure 1.4: Illustrated four step example of band alignment of a p-type CdTe absorber layer with a p^+-type Te back contact layer using experimental values to determine ΔE_g, ΔE_C, and ΔE_V (adapted from [33]).

Despite the popular use of the Anderson Rule, the simplistic assumptions found within it cause major drawbacks at the interfacial regions. The limitations present in the Anderson Rule include the absence of chemical inter-mixing and charge-dependent effects at the interface. Furthermore, there is no suitable description for how plane orientations and terminated surfaces of the layers affect band alignment. In addition, the Anderson Rule cannot provide a complex description of defects (bulk and/or interface) residing in the thin film layers. In terms of surfaces, the Anderson

Rule is incapable of describing the surface band alignment as there is no "conduction band offset" that forms without a junction forming between two layers. Therefore, it is proposed that an atomistic approach to calculating energy band alignment at surfaces and interfaces within CdTe PV devices will satisfy the limitations seen in the Anderson Rule. The suggested computational method for atomistic modeling will be based on Density Functional Theory (DFT) coupled with a Green's function formalism to investigate both the surface and interface regions (details on DFT and Green's function are looked at more extensively in Chapter 2). The following section will provide a further description of the motivation behind this work.

1.3 Motivation

The proposed research topic addresses how to accurately determine energy band alignment at the surfaces and interfaces of CdTe-based thin film PV devices using quantum-based atomistic modeling. As previously mentioned, the surfaces and interfaces remain some of the biggest challenges and limitations of CdTe-based thin film PV. It is evident from the PV research community that atomistic modeling, being one of the top proposed computational techniques, should be applied to PV research and development initiatives [22]. As the CdTe-based PV technologies continue to decrease in size and increase in fabrication processing complexity, it is becoming more essential to understand the *atomic-scale* features of thin film semiconductor device architectures. The simplistic Anderson Rule is not equipped to fully describe the energy band alignment features found at the surfaces and interfaces within CdTe PV. The current research work asserts the importance of atomistic modeling of surfaces and interfaces to accurately determine energy band alignment in CdTe-based thin film PV devices. Atomistic modeling using DFT coupled with Green's function will be the computational method of choice for evaluating the validity of the assertion.

1.3.1 Key Questions and Hypotheses

The aim of the research work is governed by four key questions pertaining to energy band alignment of surfaces and interfaces in CdTe-based thin film PV devices. Each key question was

chosen to ascertain the primary mechanisms influencing energy band alignment while providing new details applicable to real-world problems in CdTe solar technologies:

1. How do the {111} and {100} plane orientations in CdTe thin film layers impact electronic characteristics at the CdTe surface?

2. Which CdTe termination layers affect the defect density residing at the CdTe surface?

3. What does chlorine (Cl) and/or tellurium dioxide (TeO_2) do to the surface states found on CdTe terminated surfaces?

4. How will atomistic modeling of energy band alignment across the CdTe/Te interface look in comparison to precursor surface models as well as band alignments predicted by the Anderson Rule?

Hypotheses were developed in relation to the key questions to describe the expected outcomes with limited prior knowledge in atomistic modeling. Each hypothesis is provided in sequence with its respective key question above as follows:

1. The CdTe{111} and {100} plane orientations will exhibit similar energy band alignment profiles as they both terminate along a plane of the same atomic species (either Cd or Te).

2. The Cd-terminated CdTe surface will not have detrimental surface states present at the surface but will cause the bands to bend downward according to surface theory. On the other hand, Te is known to have dangling bonds, so atomistic modeling is expected to reflect the same features by creating several surface electronic states at the surface while bending the bands upward.

3. Chlorine is predicted to passivate the Te surface states due to its lower valency than Te. The density of states within the band gap near the surface are expected to be reduced in proportion to the amount of Cl concentration present at the CdTe surface. A native TeO_2 layer is anticipated to further reduce the surface states in combination with Cl.

4. The energy band alignment constructed from an atomistic modeling approach for the unrelaxed and relaxed CdTe/Te interfaces will adopt similar band bending and defect state features as calculated for the individual CdTe and Te surfaces. The interface region will simply be a superposition of the original unrelaxed/relaxed CdTe and Te surfaces with any additional charging effects that depends on termination layer (Cd or Te).

The four hypotheses will be systematically evaluated throughout the present study. It is expected that atomistic modeling will give a detailed description of the electronic features within CdTe thin film PV surfaces and interfaces that the commonly used Anderson Rule cannot address.

1.3.2 Literature Survey

Literature published on CdTe using DFT have been ***extensively investigated for electronic properties pertaining to bulk CdTe***. One of the main goals for using DFT for bulk CdTe is to reveal the complex characteristics within the CdTe electronic structure that offer insight into electrical behaviors seen in the CdTe absorber layer of thin film PV devices. However, default functional schemes within the DFT methods are not good descriptors of the band gap values seen in experimental results (see Section 2.1.4). A number of studies show that the CdTe band gap values obtained in DFT need to be in agreement with experimental measurements in order to accurately define the electronic structure in semiconductors with localized electronic states [35–37]. Well-defined electronic properties of the bulk semiconductor material are essential to problems that incorporate surfaces or interfacial effects using *ab initio* methods.

DFT simulations on point defect formations in the CdTe absorber layer have found a series of intrinsic defects that involve vacancies, substitutions of antisites and interstitials of the Cd and Te species for Te-rich and Cd-rich p-type CdTe layers [38–42]. The calculated transition energy levels of the point defects explain why certain defect states are detrimental to CdTe devices. Point defects often lead to recombination paths where an electron in the CB is relaxed to the defect energy level and then again relax to the VB to recombine with a hole, known as Shockley-Read-Hall recombination. DFT-based studies on self-compensation and pair complexes involving copper

and/or chlorine atoms during doping and passivation of CdTe have suggested plausible mechanisms that mitigate issues caused by point defects [43,44]. Experimental studies within the DFT literature have supported the conclusions found in DFT calculated defect formation and self-compensation in CdTe. It is evident that DFT has been useful in providing further insights on issues in bulk CdTe.

By extension, some DFT studies have looked at defects that exist at the CdTe grain boundaries (GB) [39, 41]. One common feature amongst the studies is that Te atoms cause deep energy level defects along certain GB orientations due to their dangling bonds. The passivation of such detrimental Te atoms has been shown clean up the defects in ways that improve the device performance. The conclusions obtained from the study of CdTe GBs suggest the importance for chemical passivation treatments of the GBs during the CdTe device fabrication process.

In recent years, a shift toward ***studying surfaces and interfaces is becoming prominent in the CdTe PV research community*** as both are essential for the advancement of CdTe PV technologies. In terms of surfaces, various DFT studies along certain CdTe plane orientations have primarily focused on the likelihood for the formation of surface reconstructions [45–48] and adatom diffusion [49, 50]. As for CdTe-based interfaces, studies have sparsingly investigated topics ranging from Schottky barrier heights between CdTe/metal interfaces [51] to heterojunctions created between the p-type CdTe absorber layer and metal chalcogenide layers [52, 53]. The underlying trait that these studies have in common is that the electronic properties associated with band alignment differ between the interface and the bulk, which result from the calculated surface and interface defect states. From the brief literature review, the following statement is clearly evident: ***electronic properties found at the interface in CdTe-based PV devices cannot be accurately determined a priori with the Anderson Rule and must be calculated using an atomistic modeling approach***.

1.3.3 Methodology

In this work, atomistic simulation models based on DFT coupled with Green's function (GF) will be developed to capture the structural and electronic phenomena in relevant CdTe-based sur-

faces and interfaces. The *ab initio* framework will enhance the fundamental understanding of energy band alignment in ways that are not possible from the Anderson Rule.

The *ab initio* modeling software chosen to perform all DFT+GF simulations will be QuantumATK. QuantumATK is a commercial software developed by employees under Synopsys Denmark that contains an integrated set of computational modeling tools for electronic structure calculations. The reason for choosing the QuantumATK software is primarily because the software platform is specifically developed to provide a state-of-the-art and user-friendly simulation package that consists of atomic modeling techniques suitable for the investigation of surfaces and interfaces [54]. Synopsys Denmark consists of development and support teams that maintain the functionality of QuantumATK while progressively enhancing the software capabilities for various applications that include solar cell technologies [55].

The complexity of the problems within the current work require suitable computational hardware to efficiently solve. Thus, high performance computing resources on the Rocky Mountain Advanced Computing Consortium (RMACC) Summit cluster [56], provided by the University of Colorado Research Computing organization, has been utilized as the main tool for DFT+GF simulations of surfaces and interfaces. Parallelization within the QuantumATK platform has been executed for decreasing the computational time necessary to converge simulations. However, careful planning on the modeling system size and parameters have been evaluated beforehand to ensure the computational efficiency and accuracy of the calculations.

A firm understanding of the concepts involved in DFT as well as a systematic procedure for obtaining the electronic bulk properties of CdTe with DFT needs to be established prior to investigating the main problems identified in the research. Chapter 2 elaborates on the fundamental background of DFT as evidence of knowledge gained in quantum-based atomistic modeling and its applicability to the research questions listed in Section 1.3.1. The chapter also includes converged DFT results for the electronic properties of CdTe that include band gap and are later used for the surface and interface atomic models.

In relation to the four key questions, the CdTe surface and CdTe/Te interface have been investigated to extract the detailed features of the energy band alignment for each modeling case. Chapter 3 evaluates the theoretical understanding of surfaces and verifies the capabilities of the QuantumATK software to determine complex CdTe surface features not included in the theoretical models. The simulation modeling cases are categorized by plane orientation (i.e. CdTe{100} and CdTe{111}), terminated surface (i.e. Cd and Te), surface relaxation and stable reconstructions within a given plane orientation to systematically verify the first two hypotheses. Additionally, the impact from Cl and TeO_2 formation on the CdTe surface band alignment is studied to confirm or negate the third hypothesis in the work.

Chapter 4 involves the validation of the fourth hypothesis in regards to energy band alignment within the CdTe/Te interface. An extension of the first and second key questions on the effect of plane orientation and termination layer will also be investigated at the CdTe/Te interface. Most importantly, the interface calculations will be compared to the original CdTe surface calculations to answer the final key question of the research effort. The main reason for choosing the CdTe/Te interface is the wealth of accessible experimental results at the selected interfacial region. Secondly, atomistic modeling of CdTe/Te is expected to provide insights on why a Te back contact has shown dramatic improvements in CdTe PV device performance. Both the outlined hypotheses and unknown mechanism for improved charge transport at the CdTe/Te interface make a compelling scenario for studying such an important region in CdTe PV.

A summary of results to date is provided in Chapter 5 to evaluate how current results either approve or disprove the hypotheses. Future work is proposed in the chapter to consider how computationally derived energy band alignments from DFT+GF can be implemented in synergistically driven research initiatives that predict CdTe PV device performance.

The current work on surface and interface simulations of CdTe PV devices is at the forefront of interfacial exploration using quantum-based computational methods. It is our expectation that the current *ab initio* framework of CdTe surfaces and interfaces will directly contribute to an efficient and progressive development of optimized CdTe-based PV technologies.

Chapter 2

Density Functional Theory Coupled with Green's Function

The atomistic modeling approach performed throughout this study enables the invesigation of electronic and structural properties of CdTe-based thin film surfaces and interfaces. The DFT+GF method is chosen to verify all hypotheses mentioned in Section 1.3.1 and ultimately reveal how atomic-scale characteristics potentially affect CdTe solar cell device performance. The following sections will briefly describe the details associated with the DFT computational scheme and Green's function formalism implemented for accurate descriptions of surfaces and interfaces. The chapter will also provide simulated results for the bulk CdTe properties that are later used for the more computationally advanced surface and interface calculations.

2.1 Density Functional Theory

DFT can be generally described as an *ab initio* method that accounts for quantum mechanical effects to predict the electronic behavior of materials. More specifically, DFT calculates material properties based on a first-principles derivation of the total ground-state energy of the system. Computational results obtained from DFT have made it possible to study atomic-scale properties without designing costly experimental setups to measure each system's physical property [57]. In combination with accuracy, DFT simulations converge to solutions relatively quick depending on the available computational hardware used for the calculations. Even modest computer hardware setups allow the user to explore various atomic-scale systems and their attributes with relatively small computational time. This is especially advantageous for real-world applications that rely on precise and insightful details of nanoscale features within the materials. DFT continues to prove its feasibility as a high-fidelity simulation method not only for university research problems but also for rapidly growing applications and technologies within areas such as the semiconductor industry.

DFT is derived from the time-independent many-body Schrödinger equation [58] used to describe the fundamental quantum mechanical theory of materials (the terms found within each equation from here onward are described in the preliminary pages under "LIST OF EQUATION TERMS"):

$$\Bigg[-\overbrace{\sum_i \frac{\hbar^2}{2m_e}\nabla_i^2}^{e^-\ kinetic\ energy} - \overbrace{\sum_I \frac{\hbar^2}{2M_I}\nabla_I^2}^{nuclei\ kinetic\ energy} + \overbrace{\frac{1}{2}\sum_{i\neq j}\frac{e^2}{4\pi\epsilon_0}\frac{1}{|\mathbf{r_i}-\mathbf{r_j}|}}^{e^- - e^-\ interaction} + \overbrace{\frac{1}{2}\sum_{I\neq J}\frac{e^2}{4\pi\epsilon_0}\frac{Z_I Z_J}{|\mathbf{R_I}-\mathbf{R_J}|}}^{nuclei\ interaction} - \overbrace{\sum_{i,I}\frac{e^2}{4\pi\epsilon_0}\frac{Z_I}{|\mathbf{r_i}-\mathbf{R_I}|}}^{e^- - nuclei\ interaction}\Bigg]\Psi = E_{tot}\Psi \tag{2.1}$$

The labels above each component in (2.1) denote the energy term that contributes to the total ground-state energy in the system. In its current form, the many-body Schrödinger equation is practically impossible to solve in systems with elements other than hydrogen. That is why many researchers have made diligent efforts to circumvent the issue of solving (2.1) by developing approximations that considerably simplify the calculations while maintaining accuracy. The general approximations made for the Schrodinger equation are as follows:

1. *Born-Oppenhemier approximation:* According to the Born-Oppenheimer or clamped nuclei approximation, the nuclei of the atoms are so heavy that they are considered immobile in relation to the electrons. Thus, the nuclei kinetic energy term can be neglected and the nuclei interaction can be simplified to a constant value.

2. *Independent electron approximation:* The many-body wavefunction cannot be computationally solved due to the complexity of the eigenvalue problem. In order to remedy the issue, the independent electrons approximation is applied so that the many-body wavefunction (Figure 2.1a) can be redefined to be a product of single-particle wavefunctions.

3. *Mean-field approximation:* The electron interaction is restored within the many-body system using a mean-field approximation, which applies an averaged electrostatic potential defined

in its energetic form, known as a "Hartree Potential" ($V_H(\mathbf{r})$), to interact with each single-electron (Figure 2.1b).

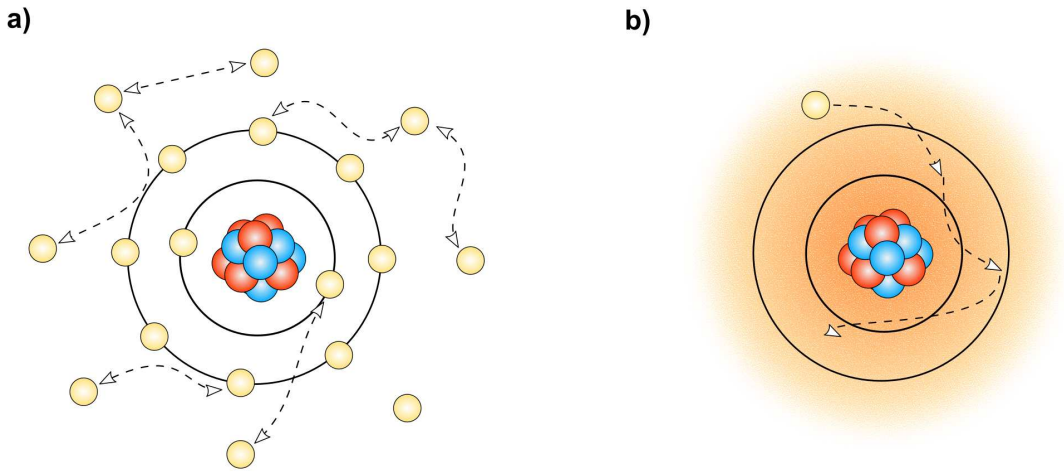

Figure 2.1: Schematic of the (a) complex many-body electron system, and (b) a single-particle representation of the many-body system where each single electron interacts with an averaged Hartree potential.

All major simplifications made to the Schrödinger equation lead to the well-known Kohn-Sham (KS) representation of the single-particle wavefunctions. The KS formulation defines the electronic system as a non-interacting electron gas that exists within an effective potential containing the classical electron-electron interactions $V_H(\mathbf{r})$, electron-ion and external interactions $V_n(\mathbf{r})$, and a newly introduced exchange-correlation potential $V_{xc}(\mathbf{r})$ as shown below:

$$\left[-\frac{1}{2}\nabla^2 + V_H(\mathbf{r}) + V_n(\mathbf{r}) + V_{xc}(\mathbf{r})\right]\phi_i(\mathbf{r}) = \epsilon_i\phi_i(\mathbf{r}) \tag{2.2}$$

where the potentials are defined at position $\mathbf{r}$, ϕ_i is the single-particle wavefunction, and ϵ_i is the ground-state energy for particle i. The summation of the ground-state eigenenergies ϵ_i will provide the ground-state total energy E_{GS}. The simple expression $n(\mathbf{r}) = \sum_i |\phi_i|^2$ is used to calculate the electron density $n(\mathbf{r})$ throughout the modeling domain. The Hohenberg-Kohn theorem states that the ground-state energy E_{GS} of a many electron system is a functional of the electron density

$n(\mathbf{r})$ [58]. Thus E_{GS} can be formally described as a functional of the electron density $n(\mathbf{r})$ using the KS formulation in (2.2) as the foundation to the DFT calculation:

$$E_{GS} = \overbrace{\int d\mathbf{r}\; n(\mathbf{r})V_n(\mathbf{r})}^{e^- - nuclei\ interaction} - \overbrace{\sum_i \int d\mathbf{r}\phi_i^*(\mathbf{r})\frac{\nabla^2}{2}\phi_i(\mathbf{r})}^{e^-\ kinetic\ energy} + \overbrace{\frac{1}{2}\int\int d\mathbf{r}d\mathbf{r}'\frac{n(\mathbf{r})n(\mathbf{r}')}{|\mathbf{r}-\mathbf{r}'|}}^{e^- - e^-\ interaction} + E_{xc}[n] \qquad (2.3)$$

where the first three terms account for the electron-nuclei interactions, electron kinetic energy, and electron-electron interactions. The final term denoted as $E_{xc}[n]$ is the most important term for quantum mechanical effects called the exchange-correlation energy. $E_{xc}[n]$ restores the "avoidance criterion" in a many-body system linked to how an electron avoids another electron as they each move throughout the electron density. The KS formulation is solved self-consistently (known as self-consistent field (SCF) process) as shown in the upper part of Figure 2.2 by calculating the electron density $n(\mathbf{r})$ based on the solved eigenfunctions. The electron density is then used to solve for the potential terms that give the ground-state energy E_{GS}. This iterative loop continues until the difference in total energies with respect to SCF steps is below the specified convergence threshold. The KS representation now enables the DFT calculations to converge to accurate electronic structures of atomic systems without the insurmountable complexity involved in the Schrödinger equation.

The convergence process can be taken one step further by means of a force minimization procedure known as *geometry optimization* (GO). The force $\mathbf{F_i} = -dE[n]/d\mathbf{R_i}$ for each atomic site I selected during the GO process is minimized via the L-BFGS optimizer algorithm within QuantumATK. The GO process is illustrated in the lower part of Figure 2.2 as an iterative framework similar to the SCF process above it. After the GO process has been converged at the specified force threshold, the resulting electron density can be used to perform further analysis of the material properties within the simulation domain. Throughout the CdTe surface and interface studies, domains without and with GO were compared to evaluate how any atomic relaxation may change the electronic characteristic at the regions of interest. Both the SCF and GO processes sustain the

convergence behavior of the KS formulation so as to achieve an accurate ground-state electron density. The following subsections will now briefly evaluate some of the terms involved in (2.2) as well as how they contribute to the DFT methodology used in the present research study.

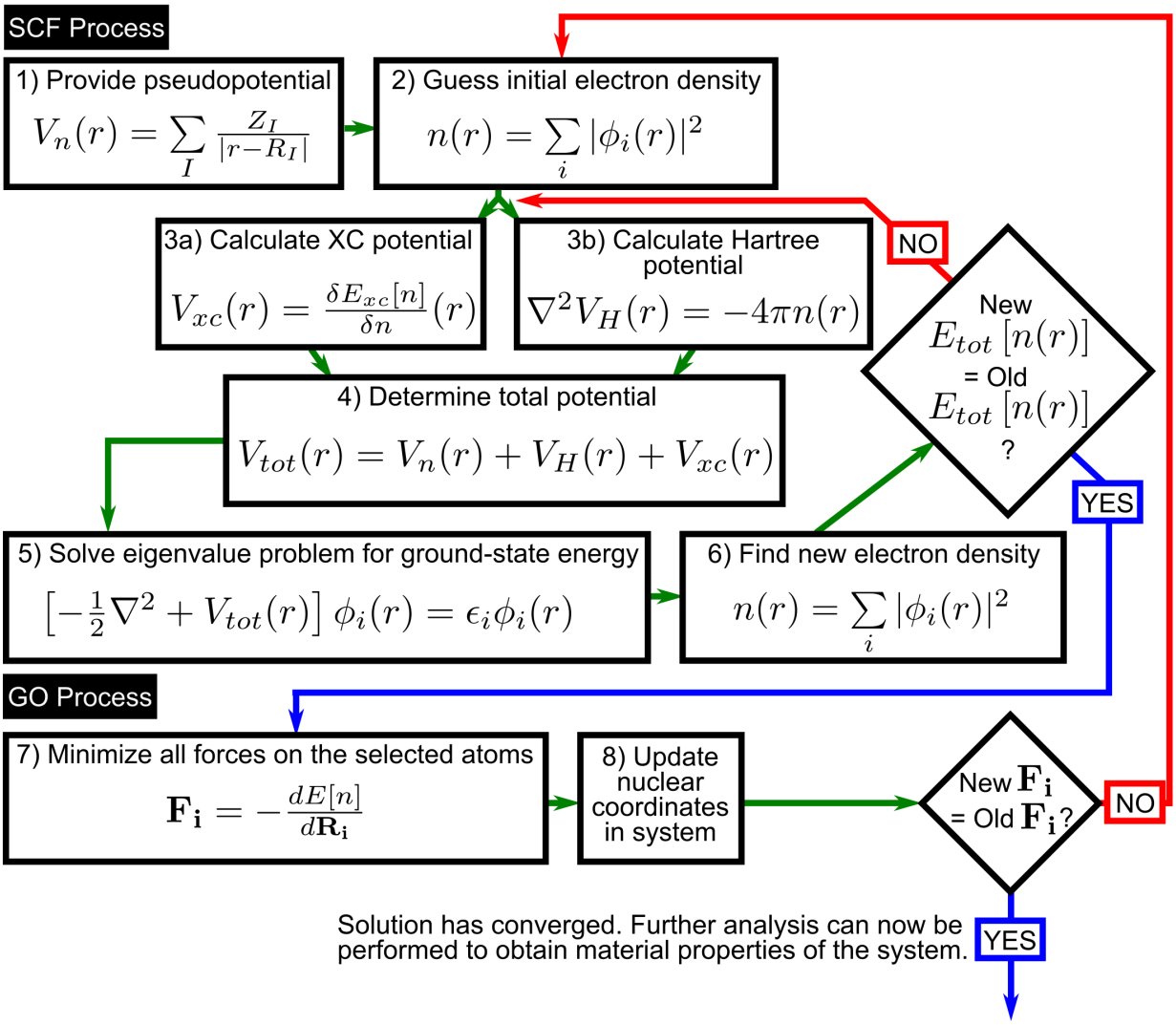

Figure 2.2: Schematic flowchart of the SCF process for solving the KS formulation.

2.1.1 Linear Combination of Atomic Orbitals Representation

The numerical procedure in a DFT calculation plays a crucial role in the reliability and scalability of the model itself. One must ensure that the basis set used to describe the many-body wavefunction adheres to a precise representation of the KS equation while minimizing the compu-

tational demand required to model the system of interest. The development of Linear Combination of Atomic Orbitals (LCAO) stems from the approach of creating well-defined basis functions that are localized to a given region indicative of certain atomic orbitals [59]. Although Plane-Wave (PW) based DFT remains the most popular form for calculating KS periodic systems, LCAO offers several advantages over PW that make it a versatile representation for numerous simulation cases. First, LCAO basis functions converge quickly since the localized nature of the basis make the orbitals confined to regions where their interactions are expected. Strictly localized orbitals avoid the numerical instabilities that PW suffers at shorter ranges (although this is remedied by additional core electron descriptors such as pseudopotentials). As a result, the number of basis functions required to describe the system is quite small in comparison to the PW basis. Secondly, LCAO basis sets are well-suited for being used in non-periodic surface or interface calculations when coupled with a Green's Function formalism [60–63]. PW basis sets are restricted to periodic systems, thus requiring a sufficiently large modeling domain perpendicular to the surface/interface to properly converge the quantum mechanical features within that region. By extension, LCAO DFT can be used for nonperiodic nonequilibrium conditions formed by finite voltage bias of electrodes with differing chemical potentials [64].

LCAO Basis Sets

Efficiency and accuracy are a necessity in the basis that are incorporated in the LCAO-DFT method for various simulation environments. In order to ensure the efficiency-accuracy dichotomy [65], efforts by those using LCAO in the DFT community have developed optimized basis orbitals for each atom in the periodic table. These basis orbitals are centered around the atoms and summed together to self-consistently calculate the electronic structures of materials. Electronic eigenstates ϕ_i are expanded as a linear combination of atomic-like states in the form of orbitals. These states make up the LCAO basis sets used to solve for the total ground-state energy E_{GS} in (2.3). The following equation format describes the LCAO representation in its index form:

$$\phi_{Inlm}(\mathbf{r}) = R_{Inl}(|\mathbf{r_I}|)Y_{lm}(\hat{\mathbf{r}}_\mathbf{I}) \tag{2.4}$$

where $R_{Inl}(|\mathbf{r_I}|)$ and $Y_{lm}(\hat{\mathbf{r}}_\mathbf{I})$ denote the radial part and spherical harmonics part of the LCAO basis, respectively. The subscripts n, l, and m are the respective principle, angular, and magnetic quantum numbers associated with the basis set of a given atomic site I in the system. Both the radial and spherical harmonics terms contribute to the optimization of the basis functions for each species in the system while achieving *transferability* (i.e. basis functions for a single species system should work for another system with a more complex and/or inhomogeneous environment). The three main considerations to optimizing LCAO basis functions are size, shape, and range. The size of the basis is defined as the number of atomic orbitals per atom that are used during the hamiltonian matrix calculations. The number of pre-defined radial (i.e. single-ζ, double-ζ) and polarization functions control the size of the basis. The range of the basis is the spatial extension of the atomic orbitals and is directly modified by a cutoff radius. The cutoff radius is crucial for accuracy and computational efficiency in the LCAO scheme. Shape of the basis must be optimized in a manner that does not influence the core region (pseudopotential is used to account for core electrons interacting with the atomic nuclei and each other), yet produces a function that has a continuous derivative throughout its region of existence (between some internal radius r_i and the cutoff radius r_c). A soft confinement potential $V(r)$ is implemented to the basis [59] of the LCAO representation in the software package QuantumATK [66] so that basis shape is optimized.

Basis Set Expansion to Solve KS Equations

The term "linear combination" in LCAO refers to the superposition of basis functions for each atomic species within the computational domain. The basis functions $\phi_{Inlm}(\mathbf{r})$ must be summed over all the atoms I and its respective quantum numbers within the computational domain [58] to form was is known as the basis set. The resulting basis set $\phi_i(\mathbf{r})$ used in s (2.2) and (2.3) can be written as an expansion of the basis functions as follows:

$$\phi_i(\mathbf{r}) = \sum_\nu c_\nu \varphi_\nu(\mathbf{r}) \tag{2.5}$$

where $\varphi_\nu(\mathbf{r}) = \phi_{Inlm}(\mathbf{r} - \mathbf{R_I})$ acts as a compact notation of the basis function and ν is a composite index identifying the atomic site I and quantum numbers n, l, m. The unknown coefficients c_ν are non-orthogonal coefficients that are important for solving the KS equations throughout the SCF calculation. If the φ notation is used in (2.3) and the equation is multiplied by φ^*_μ, a "generalized eigenvalue problem" for the LCAO representation can be conveniently expressed as:

$$\sum_\nu \left(\mathcal{H} - \epsilon_i \mathcal{S}\right)_{\mu\nu} c_{i\nu} = 0 \tag{2.6}$$

with $\mathcal{H}$ as the Hamiltonian matrix,

$$\left(\mathcal{H}\right)_{\mu\nu} = \int d\mathbf{r} \varphi^*_\mu(\mathbf{r}) \left[-\frac{1}{2}\nabla^2 + V_H(\mathbf{r}) + V_n(\mathbf{r}) + V_{xc}(\mathbf{r})\right] \varphi_\nu(\mathbf{r})$$

and $\mathcal{S}$ as the overlap matrix,

$$\left(\mathcal{S}\right)_{\mu\nu} = \int d\mathbf{r} \varphi^*_\mu(\mathbf{r}) \varphi_\nu(\mathbf{r})$$

The LCAO representation requires an overlap matrix to account for the non-orthogonality that exists in the numerical procedure of the basis set (i.e. $\int d\mathbf{r} \varphi^*_\mu(\mathbf{r}) \varphi_\nu(\mathbf{r}) \neq 0$). The transition from a differential form to a matrix form of the KS formulation permits the DFT calculation to solve the expansion coefficients c_ν and later to determine the electron density throughout the domain.

2.1.2 Pseudopotential

Various researchers of DFT algorithms have sought ways to simplify the required computational demands prevalent during the calculations. One area where further approximations have been applied is the description of core electrons and their interactions with the nuclei of the system. Wavefunctions near the nuclei of the atoms do not affect the overall chemical, mechanical, or electronic properties as much as wavefunctions representing the valence electrons in the system. Therefore a weaker effective potential known as a pseudopotential replaces the coulomb potential near the nucleus to account for the nuclear and core electron interactions.

Any constructed pseudopotential must ensure that the resulting atomic valence pseudo-orbital is identical with the corresponding atomic orbital in an equivalent system calculated by an all-electron method. Pseudopotentials reduce the overall computational demand by decreasing the basis set required to fully describe the system for a given simulation. The atomic basis sets have been optimized together with the pseudopotential description in the QuantumATK software. Several pseudopotential options were briefly investigated for the CdTe bulk simulations as shown in Table 2.1 and Table 2.2 of Section 2.2 that include the Fritz-Haber Institute (FHI), OpenMX (OMX) [67, 68], FHI+OMX and SG15 [69] norm-conserving pseudopotentials. The SG15 pseudopotential has proven to be accurate and transferable for metal chalcogenide and some ternary compound systems [69]. However, a combination of the FHI and OMX pseudopotentials was selected as it gave both consistent structural and electronic properties during CdTe surface and interface DFT calculations.

2.1.3 Exchange-Correlation Functional

The total ground-state energy E_{GS} as expressed in (2.3) includes an energy term E_{xc}, known as the exchange-correlation (XC) energy functional. As mentioned earlier, E_{xc} is an approximated term in a many-body system that restores the quantum mechanical effects within the system. It primarily accounts for how one electron avoids another as it moves throughout the electron density. The XC functional is described by two parts: 1) an exchange part that relates to the Pauli exclusion principle, and 2) a correlation part that captures how every electron pushes on the other electrons surrounding it in the form of Coulomb repulsion. Such an approximation has to be accurate and feasible for all computations so that the method can accomodate for binding between atoms. The simplest method of the exchange-correlation functional is known as the local density approximation (LDA), which is expressed as follows:

$$E_{xc}^{LDA}[n] = \int d^3r \; n(\mathbf{r})\epsilon_{xc}^{unif}(n(\mathbf{r})) \tag{2.7}$$

where $\epsilon_{xc}^{unif} n(\mathbf{r})$ denotes the XC energy per electron of a homogeneous gas. Equation (2.7) is valid when the electronic density changes slowly with respect to position [70]. Although it is possible to obtain an exact, analytical expression for the exchange energy in the uniform electron gas, an approximation for the correlation energy must be used as no exact solution is obtainable. The LDA variant used in the current work is based on the parametrization developed by Perdew and Zunger [71]. LDA is suprisingly accurate for its simplistic formulation as its embedded constraints obey the XC hole restriction. More improvements have been made using the Local Spin Density Approximation to include the spin dependence of the electron density.

Higher order terms can be included within the XC functional to provide greater accuracy to the XC energy. Among these is the XC functional known as Generalized Gradient Approximation (GGA), which additionally depends on the gradient of the electron density and is defined as:

$$E_{xc}^{GGA}[n] = \int d^3r \; n(\mathbf{r}) f\left(n(\mathbf{r}), \nabla n(\mathbf{r})\right) \tag{2.8}$$

Both the LDA and GGA XC functionals are among the popular options for re-establishing the quantum mechanical effects in DFT calculations. However, further corrections to both the LDA and GGA XC functionals are necessary to account for the self-interaction error inherent to both approaches as well as their poor description of CB energy levels. The next subsection will briefly describe the semi-empirical correction used to accommodate the limitations of the local approximations to the XC energy.

2.1.4 Hubbard-U Correction

All DFT calculations in the research work require an accurate representation of the band gaps for the CdTe-based modeling systems. It is widely known that the common LDA and GGA XC functionals underestimate band gaps seen in experimental literature, mostly due to the delocalization of valence electrons [72]. That is why a semi-empirical method known as the Hubbard-U correction is applied to the Hamiltonian matrix as a means of re-introducing the localized nature of

valence electrons found in metal chalcogenide compounds like CdTe [35]. The simplified version of the Hubbard-U formalism [72] is described using the following format:

$$E_U = \frac{1}{2} \sum_{\mu} U_{\mu} \left(n_{\mu} - n_{\mu}^2 \right) \tag{2.9}$$

where n_{μ} is the projection onto an atomic shell and U_{μ} is the on-site Coulomb repulsion energy parameter that is semi-empirically chosen to reproduce the bandgap E_g of the bulk material. The Hubbard-U correction within the current study was implemented for two reasons:

1. Re-establish the CdTe band gap at areas where the material exhibits bulk-like electronic and structural behavior.

2. Ensure the transferability of CdTe between more complex simulation environments such as CdTe surfaces and interfaces.

The Hubbard-U formalism allows for an appropriate representation of the CdTe band gap so that an accurate construction of energy band alignment may be ascertained from the atomistic models. Hubbard-U has a moderate computational cost in comparison to other hybrid functionals while maintaining the descriptive behavior of the electron-electron interactions. Various DFT studies have investigated the structural and electronic effects caused by applying the Hubbard-U formalism to metal chalcogenide systems [35–37, 73]. In this work, the on-site Hubbard-U formalism is used, which is available in the QuantumATK software program.

The next section will look at the comparison between several pseudopotentials without and with Hubbard-U correction for investigating the CdTe bulk structural and electronic properties. The main purpose for evaluating a number of pseudopotentials and Hubbard-U values was to identify any discrepancies between them in accuracy as well as to decide which one or a combination of them was appropriate to use throughout the research work.

2.2 CdTe Bulk Investigation

Different computational setups were evaluated for their accuracy in calculating structural and electronic properties of bulk CdTe. The total energy difference per parameter change (denoted as $|\delta E_{tot}|$) was minimized for both the Perdew-Zunger (PZ) [71] and Perdew-Burke-Ernzerhof (PBE) [74] forms of the LDA and GGA XC functionals, respectively, using different k-point and density mesh cutoff E_{mesh} values as shown in Figure 2.3. The convergence criterion was selected to be 2.5 meV/cell to ensure that the bulk CdTe DFT results were independent of changes to the convergence parameters. Figure 2.3a shows that both XC functionals converge quickly after n = 6 k-pts along each reciprocal lattice direction using an E_{mesh} value of 2200 eV. However, Figure 2.3b shows that there are significant differences in the convergence behavior between XC functionals. The top subfigure represents the LDA-PZ convergence with respect to E_{mesh} value, while the bottom subfigure is for the GGA-PBE XC functional convergence. It is obvious that LDA-PZ converges more quickly than GGA-PBE with respect to the E_{mesh} value. The LDA-PZ converges around 2000 eV for most pseudopotentials while GGA-PBE requires a E_{mesh} value > 3000 eV to properly converge below the 2.5 meV/cell threshold. It is also obvious from the difference in scaling on the ordinate axes that LDA-PZ requires a lower E_{mesh} compared to GGA-PBE. Although only LDA-PZ successfully converged at such conditions, it was decided that a density mesh cutoff of 2200 eV and a k-pt density of 11 $\times$ 11 $\times$ 11 would be used for all other bulk calculation comparisons moving forward. For any simulations that included GO, a force threshold of 0.001 eV/Ang was utilised for such calculations. Structural and electronic properties analyses were performed on the conventional CdTe unit cell as illustrated in Figure 2.4 and will be briefly considered in the following subsections.

2.2.1 Structural Properties

Various CdTe structural properties after applying geometry optimization to the CdTe unit cell in Figure 2.4 were calculated such as equilibrium lattice constant a_{eq} and symmetrized elastic tensors (C_{11}, C_{12}, and C_{44}). The parameters were compared between each XC functional and

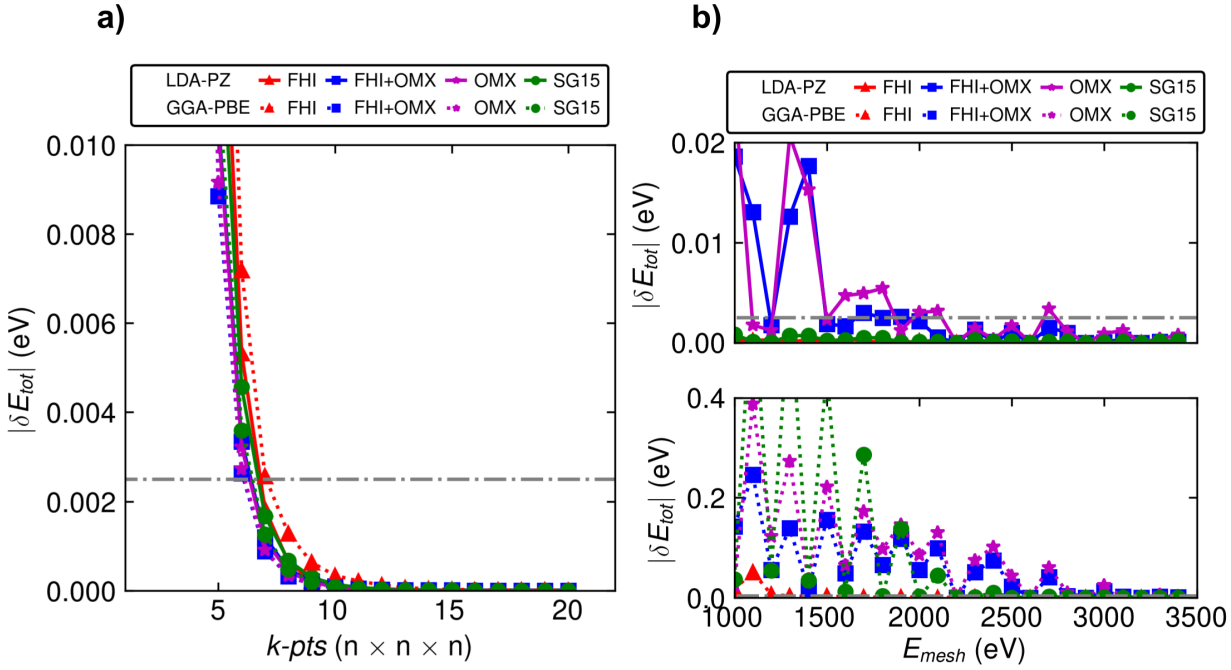

Figure 2.3: Convergence testing for different XC functionals and pseudopotentials with respect to a) varied k-point densities at density mesh cutoff E_{mesh} = 2200 eV and b) varied E_{mesh} values at 11 × 11 × 11 k-points. The gray line marks the 2.5 meV/cell threshold for the absolute difference in total energy. The CdTe bulk primitive cell with a fixed lattice constant of 6.480 Ang was utilized for all calculations.

pseudopotential combination as shown in Table 2.2. Although mechanical properties are not primarily focused within the scope of the current research, the analysis was simply done to verify how close the calculated values were to the experimental values determined for the zinc-blende CdTe bulk crystal. It must be noted that all DFT simulation values were evaluated at temperature T = 0 K, which will differ from the experimental values determined at room temperature.

In general, both the LDA and GGA calculations yield a lattice parameter within 5% of the experimental value with the LDA-PZ OMX set having the smallest error at 0.17%. All of the XC+pseudopotential combinations except for the LDA-PZ SG15 set overestimate the lattice constant a_{eq}. Looking the the symmetrical elastic tensors C_{ij}, there is significantly more variation and thus higher error from the experimental values. For example, the term C_{11} is predicted to be down to 27% lower for the GGA-PBE + FHI combination and up to 14% higher for the LDA-PZ + OMX combination than the experimental values from Reference [75]. The wide variation in elastic prop-

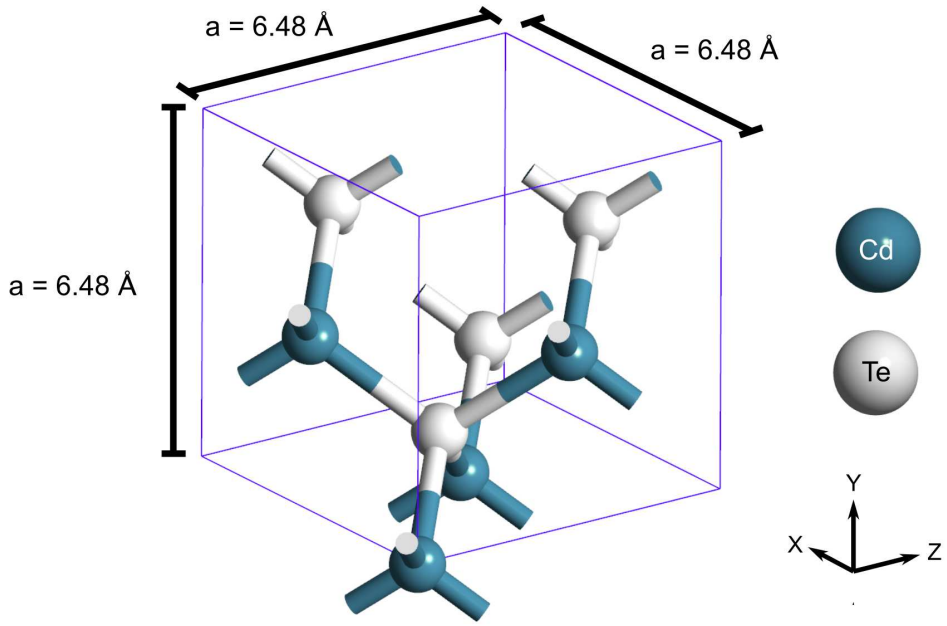

Figure 2.4: Illustration of the conventional CdTe unit cell used for the DFT-based structural and electronic properties calculations

erties have been seen within other DFT studies [76], which show the difficulty of converging all specific aspects of CdTe bulk system. A more intricate method that properly describes the elastic properties of the CdTe would be necessary as such properties appear to be an inherent limitation of the used XC functionals. As mentioned beforehand, the CdTe bulk mechanical properties were not the primary focus in the current research study, but more so the electronic properties that dictate energy band alignment. The rest of the section will concentrate on the CdTe electronic characteristics with the addition of a Hubbard-U correction to establish transferability in more complex systems.

2.2.2 Electronic Properties

Suitable DFT parameters that firmly establish the electronic properties within the CdTe bulk system must be carefully selected prior to using them in surface and interface calculations. Different combinations of XC functionals and pseudopotentials were tested for two essential parameters crucial to the solid state physics seen in semiconductor compounds: effective mass m^* and semiconductor band gap E_g.

Table 2.1: Comparison of the CdTe structural properties for the LDA-PZ and GGA-PBE functionals with various pseudopotentials after GO. The experimental (Expt.) values are provided in the last row with the references located at the bottom of the table.

XC	Pseudopotential	Lattice Constant, a_{eq} (Ang)	Elastic Tensor (GPa) C_{11}	C_{12}	C_{44}
LDA-PZ	FHI	6.536	58.70	42.23	20.28
	FHI+OMX	6.635	40.11	37.85	20.79
	OMX	6.491	61.56	42.66	18.64
	SG15	6.450	59.68	41.06	18.87
GGA-PBE	FHI	6.624	39.09	29.70	14.23
	FHI+OMX	6.746	40.19	25.74	25.27
	OMX	6.746	40.19	25.74	25.27
	SG15	6.647	44.68	31.54	16.57
Expt.[a]		6.480			
Expt.[b]			53.8	37.4	20.18
Expt.[c]			53.51	36.81	19.94

[a]Ref. [77].
[b]Ref. [75].
[c]Ref. [78].

Effective mass can be simply described as the apparent mass of a semi-classical particle (either an electron or hole) as it interacts with other particles and the periodic potential created within the crystal structure. It is an important parameter for semiconductors since it determines the curvature of the band edges formed by the density of quantum states within the Brillouin zone of the reciprocal unit cell. With the band edges (valence and conduction bands) usually assumed to be parabolic, the effective mass assists in quantifying the number of allowed electronic states in the CB (using m_e) and VB (using m_h). Table 2.2 reveals the effective mass and band gap results for each investigated DFT setup combination. The results show that there is no clear DFT setup that accurately calculates all CdTe parameters. All of the setups, except the LDA-PZ and FHI combination, underestimate the experimental electron effective mass m_e of 0.11. Even the other computational studies [73, 79] do not predict the electron effective mass precisely. It is obvious that the semi-local functionals do not correctly address the CdTe effective masses as intended for a first-principles approach.

Table 2.2: Comparison of the CdTe electronic properties for the LDA-PZ and GGA-PBE functionals with various pseudopotentials after GO. Outside experimental (Expt.) and computational (Comp.) references for the effective mass and band gap for bulk CdTe are provided as well below the table. For Ref. [73], the calculation was based on PW-DFT (LDA Purdue Zunger XC functional, without spin-orbit coupling). For Ref. [79], the calculation used the Full Potential Augmented PW-DFT (LSDA Perdew Wang XC functional).

XC	Pseudopotential	Effective Mass, m^* (m/m_0)					Band Gap,
		m_e	$m_{lh,[100]}$	$m_{hh,[100]}$	$m_{lh,[111]}$	$m_{hh,[111]}$	E_g (eV)
LDA-PZ	FHI	0.298	0.064	0.469	0.056	0.993	0.00
	FHI+OMX	0.065	0.067	0.511	0.058	1.091	0.87
	OMX	0.065	0.067	0.511	0.058	1.091	0.87
	SG15	0.047	0.047	0.487	0.043	1.058	0.59
GGA-PBE	FHI	0.024	0.022	0.520	0.021	1.140	0.00
	FHI+OMX	0.059	0.060	0.635	0.055	1.348	0.67
	OMX	0.056	0.057	0.631	0.052	1.333	0.64
	SG15	0.047	0.047	0.580	0.044	1.249	0.53
Expt.[a]							1.49
Expt.[b]		0.11					
Comp.[c]		0.03	0.33	0.39	0.35	0.54	0.48
Comp.[d]		0.047	0.051	0.879	0.038	1.555	

[a]Ref. [34].
[b]Ref. [80].
[c]Ref. [73].
[d]Ref. [79].

The same issue arises when calculating the CdTe band gap E_g. The least accurate DFT setup was the FHI pseudopotential-based calculations which predicted a metallic-like behavior for the CdTe system. It is clear that the LDA and GGA XC functionals severly underestimate the CdTe band gap. The band gap limitation is an inherent problem in semi-local exchange-correlation functionals as previously described in Section 2.1.4. Early on in the research process, the GGA-PBE XC functional and SG15 pseudopotential along with the Hubbard-U correction was used for more complex interface calculations of energy band alignment [81]. The choice gave encouraging results as it has been used in published literature for DFT-LCAO calculations of related solar cell thin-film layers [55, 82]. However, other important properties such as the cleavage energy of plane-oriented single crystal CdTe surfaces were not accurate compared to the LDA-PZ and

FHI+OMX combination. Thus, it was decided to use the LDA-PZ XC functional, FHI+OMX pseudopotential combination and the Hubbard-U correction for all reported surface and interface calculations. LDA-based DFT with a Hubbard-U correction not only improves the band gaps of *sp*-hybridized semiconductors like CdTe, but it also improves the electron and light-hole effective mass descriptions at the high symmetry Γ-point within the CdTe Brillouin zone [83].

The CdTe effective masses and band gaps were analyzed before and after the Hubbard-U correction was applied to the CdTe bulk conventional unit cell. Both of those conditions were evaluated without and with geometry optimization enabled at the same threshold as mentioned earlier. This was done to decouple the changes on the calculated bandstructures due to relaxation effects. Table 2.3 shows the compiled results for each DFT setup using the LDA-PZ and FHI+OMX combination. The chosen U-values for the Cd-4d and Te-5p orbitals were U_{Cd-4d} = 4.6 eV and U_{Te-5p} = 2.55 eV. The U_{Te-5p} value was selected since it was used in another DFT-based study on the zinc-blende CdTe structure [36]. The U_{Cd-4d} value was swept across different magnitudes until an appropriate CdTe band gap was obtained.

Table 2.3: Comparison of the CdTe effective masses and band gaps (eV) for the LDA-PZ exchange-correlation functional and FHI+OMX pseudopotential combination with and without an applied Hubbard-U correction. The U-values used were U_{Cd-4d} = 4.6 eV and U_{Te-5p} = 2.55 eV. DFT+U calculations without GO have a lattice parameter set equal to the experimental value of 6.48 Å, while DFT+U after GO applies the Hubbard-U values during the optimization process of the CdTe structure.

Setup	Effective Mass, m^* (m/m_0)					Band Gap, E_g (eV)
	m_e	$m_{lh,[100]}$	$m_{hh,[100]}$	$m_{lh,[111]}$	$m_{hh,[111]}$	
LDA (no GO)	0.060	0.060	0.457	0.053	0.974	0.79
LDA (with GO)	0.065	0.067	0.511	0.058	1.091	0.87
LDA+U (no GO)	0.125	0.122	0.575	0.099	1.250	1.49
LDA+U (with GO)	0.106	0.147	0.646	0.101	1.459	1.15

Prior to GO, both the electron effective mass and band gap for CdTe were further away from the experimental values than with GO applied. Greater differences were seen between the heavy-hole effective masses $m_{hh,[111]}$ and contribute to the slight band gap difference of 0.08 eV between the

two simulation setups. However, the biggest change in band gap occurred for both the unrelaxed and relaxed versions of the LDA+U simulations. Both simulations had a much closer electron effective mass magnitude to the experimental one (0.11 [80]) while at the same time increasing the CdTe band gap value. The simulation without GO restored the band gap to the experimental value of 1.49 eV [34] while the GO simulation was smaller by 22.8%. Both relaxation and Hubbard-U correction play a crucial role to the calculated electronic properties in CdTe systems.

Further analysis by means of calculated bandstructure and electron densities were done to verify how the Hubbard-U values were causing such noticeable changes to the CdTe band gap. Figure 2.5 shows the CdTe bandstructure without and with a Hubbard-U correction applied to the unrelaxed CdTe bulk conventional unit cell. The band gap for CdTe was re-established near the Γ-point after using Hubbard-U by the downward and upward shift in the VBM and CBM, respectively. It is worth noting that both the VB and CB curvatures have been modified after the Hubbard-U correction, indicative of a change in the effective masses that are closer in agreement with experimental values. The accurate CdTe bulk band gap description seen in Figure 2.5 after the Hubbard-U correction allowed for a valid construction of band alignment of the CdTe-based thin-film surfaces and interfaces performed in this research.

Similarly, the partial electron density difference analysis found in Figure 2.6 provided a deeper glimpse into how the calculated partial charge densities visually determine which atoms contributed to the bands found in the bandstructure. The analysis was performed by first evaluating the partial electron densities at VBM and CBM, then taking the difference between them as CBM - VBM in CdTe bulk. Therefore, the colormaps can be interpreted as blue and red marking the VBM and CBM, respectively. Various planes mapped across the [100] direction in terms of fractional coordinates are plotted in each subfigure. There are interesting characteristics within the density difference plots that resemble the probabilistic nature and shape of the Cd-4d and Te-5p orbitals. Figure 2.6b is plotted at $X = 0.0$ along the Cd-terminated CdTe(100) plane, which shows the highest CBM electron density $n(r)$ (red color) around the Cd atomic sites. Inside the red regions are four inner regions at the Cd atomic sites that have a magnitude closer to the VBM (blue color).

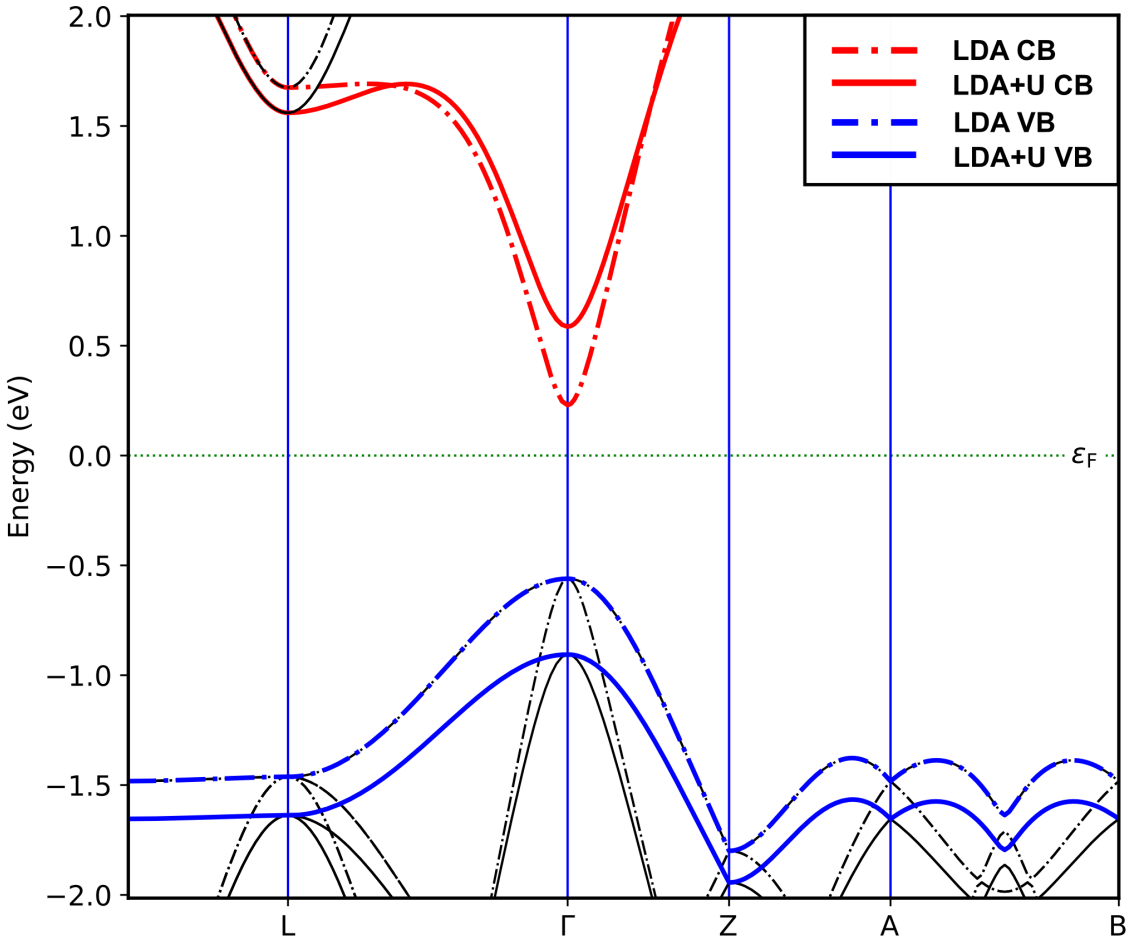

Figure 2.5: Calculated CdTe bandstructure using the LDA-PZ XC functional without and with the Hubbard-U correction applied to the Cd-4d and Te-5p shells. The blue curves mark the valence band while the red curves mark the conduction band.

The inner regions give a d-like orbital character that represent one of the Cd-4d orbitals bisected along that plane. Due to the symmetry of the Cd and Te atoms within the conventional unit cell, the characteristics of Figure 2.6c ($X = 0.1$) and Figure 2.6f ($X = 0.4$) are similar in nature, which show interactions between the Cd and Te atoms near the planes at those X fractional coordinates. The projected region of the Te valence electrons is marked in blue, depicting a small p-orbital shape that expands outward closer to the Te atom. Both Figure 2.6d and Figure 2.6e are closest to the Te atom position along the X [100] axis. The p-orbital character is quite apparent and adopts a blue color, indicating its primary role in the VBM of CdTe. Lastly, the features seen in Figure 2.6g for the Cd atomic sites are similar to Figure 2.6b. From the results, it is strong correlation with

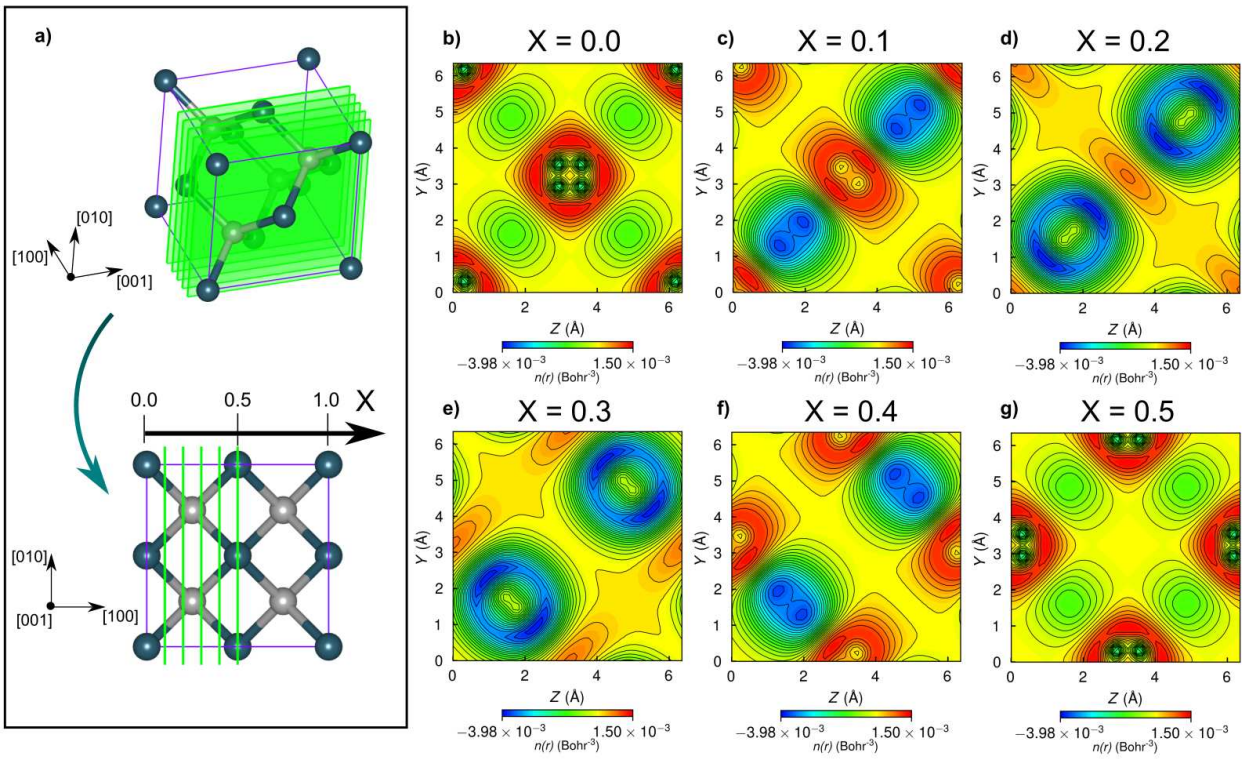

Figure 2.6: Partial charge density difference analysis at the CBM and VBM across the CdTe conventional unit cell after incorporating the Hubbard-U correction to the LDA-based DFT calculation. Subfigure (a) illustrates green-colored planes tracing where the six partial density plots were measured along the [100] direction of the unit cell (the first plane at X = 0.0 is omitted for clarity). All other subfigures (b) through (g) reveal the partial density differences with the fractional X-coordinate labeled above them.

the orbitals residing around the Cd and Te atomic sites with there contribution to the CBM and VBM, respectively, which accounts for the effect of the Hubbard-U correction in CdTe band gap calculations.

Extra insight is gained by evaluating the CdTe projected bandstructure by distinguishing which curves are formed due to the Cd and Te orbital bands. Figure 2.7 gives a detailed bandstructure due to the Cd-4d and Te-5p bands without and with the Hubbard-U correction applied to the LDA-PZ XC functional for CdTe. The visual color scheme maps the areas where the certain bands contribute to the curves that make up the bandstructure. In Figure 2.7a and Figure 2.7b, the Cd-5s band is strongly present in the CB, justifying it to be the main contributor to the CB edge at the

Γ-point. The Hubbard-U correction is readily seen by comparing Figure 2.7c to Figure 2.7d. The Cd-4d bands without Hubbard-U have a pronounced effect on the CdTe VB and thus prevent the Te-5p bands from localizing properly as shown in Figure 2.7e, resulting in the CdTe band gap being underestimated at 0.79 eV. On the other hand, using a Hubbard-U value of U_{Cd-4d} = 4.60 eV on the Cd-4d bands will cause the curves where they reside most to shift downward on the energy scale (Figure 2.7d) and thus have a decreased effect on the Te-5p localization of bands. Lastly, looking at Figure 2.7e and Figure 2.7f reveals that a Hubbard-U value of U_{Te-5p} = 2.55 eV used on the Te-5p bands allow the bands to sit in the correct energy position so that the CdTe band gap is re-established at 1.49 eV. It can be said with certainty that the Hubbard-U correction is properly localizing the Cd-4d and Te-5p bands to improve the electronic structure of bulk CdTe.

Lastly, verification of the accuracy in using the LDA+U method for the electronic properies in CdTe bulk was made by comparing energy positions of the U-corrected atomic subshells determined by a projected density of states (DOS) analysis to experimental literature [84] as shown in Figure 2.8. A similar approach using photoemission spectra to compare the binding energy positions of the Cd-4d and Te-5p bands after using the Hubbard-U correction has been done [37], which was also followed in this study. According to Figure 2.8b, the Hubbard-U values of 4.60 eV and 2.55 eV for the Cd-4d and Te-5p bands, respectively, have caused the Cd-4d band to shift downward (left direction) and Te-5p band to be properly localized within the CdTe bandstructure. At the same time, the energy positions for the Cd-4d and Te-5p bands are in good agreement with various photoemission spectra data [84, 85], confirming that the chosen U-values are sufficient for bulk CdTe.

In summary, two important consequences can be immediately drawn from the results. First, the effect of GO on the CdTe bulk electronic properties is somewhat noticeable due to the re-sizing of the CdTe unit cell and associated atomic displacements to minimize the CdTe total energy. Any GO applied to CdTe will cause the band gap to change accordingly, which will certainly affect the energy band alignment in more complex simulation domains. Second, the chosen Hubbard-U values significantly increase the CdTe band gap as well as lead to effective masses that are closer to

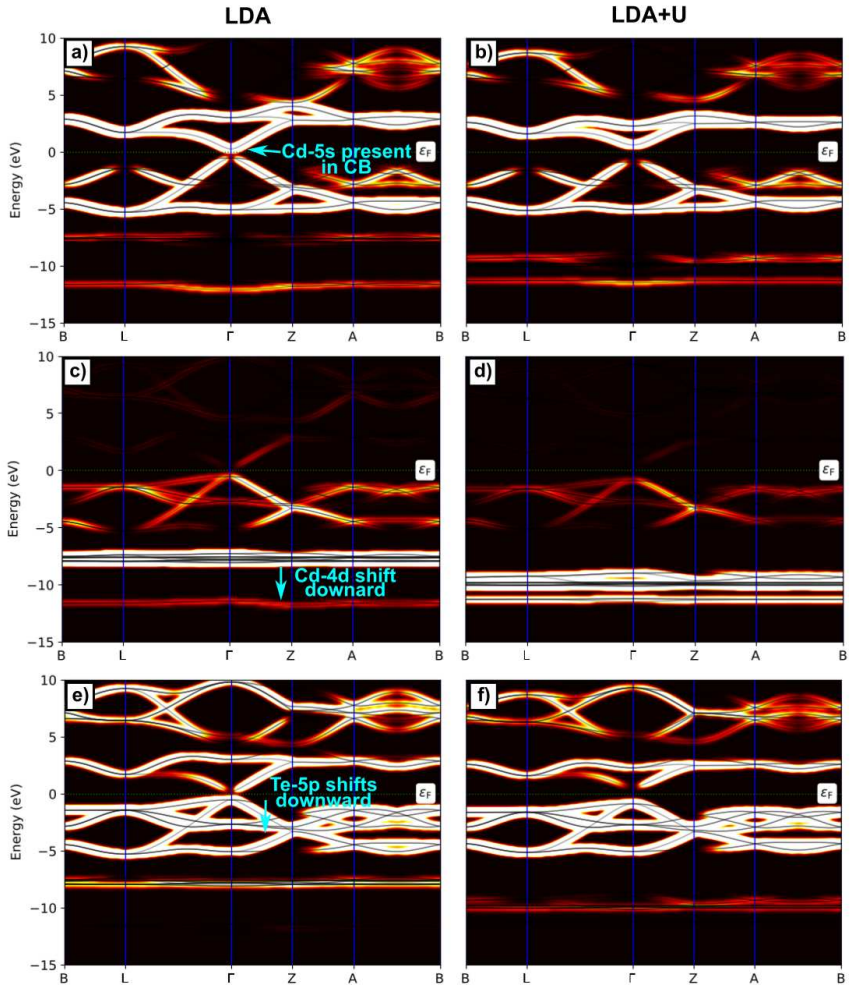

Figure 2.7: Calculated CdTe projected bandstructure using the LDA-PZ XC functional without and with Hubbard-U correction. The project bandstructures are separated as (a,b) Cd-5s, (c,d) Cd-4d_{z^2} and (e,f) Te-5p_z orbitals for the LDA and LDA+U DFT calculations.

experimentally reported values. The Hubbard-U correction is essential to the electronic structure of zinc-blende CdTe and thus was expected to dramatically influence the resulting energy band alignments of surfaces and interfaces studied in this work.

2.3 Green's Function Formalism

Ab initio methods that attempt to simulate interfaces typically use finite-sized models consisting of several atomic layers that form "slabs" with vacuum regions at each end (Figure 2.9a). The limitations of using such a framework for interface modeling involve 1) the geometry being

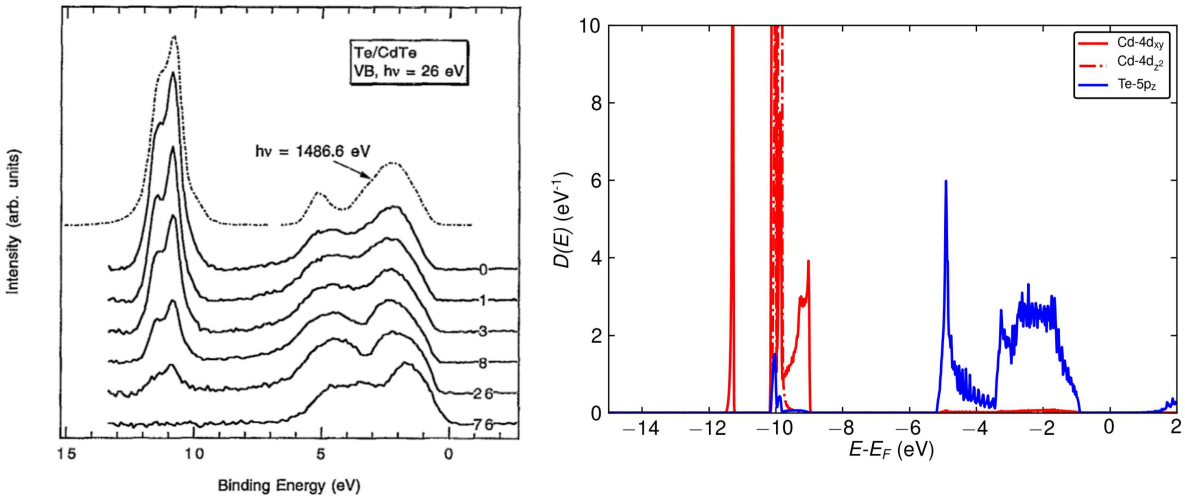

Figure 2.8: Comparison of photoemission spectra data (image on the left, taken from [84]) and the projected density of states (right image) of the LDA+U calculation in the bulk CdTe. A Gaussian broadening of 0.01 eV was used for the projected DOS analysis.

restricted to periodic systems that require expensive computational loads to accurately represent the space charge effects seen in junctions across semiconductor devices, and 2) no straightfoward method to combine two materials with differing chemical potentials to simulate non-equilbirium conditions at the interface [61, 64]. The Green's function (GF) formalism is capable of addressing both limitations by developing a model system that consists of several distinct regions that algorithmically interact with each other. All GF models implement a central region of atoms to describe the electronic structure of the surface or interface. The central region is then coupled to either one semi-infinite bulk electrode and a vacuum region (one-probe model [62] shown in Figure 2.9b) or two semi-infinite bulk electrodes that act as open boundary conditions for the central region (two-probe model [61] shown in Figure 2.9c). The electron density $n(r)$ throughout the interface is obtained from the real space representation of the density matrix within the central region. The density matrix must be defined by several additional terms that account for coupling between each electrode and the central region (a.k.a. self-energy $\Sigma_{1,2}$), each electrode's chemical potential $\mu_{1,2}$ and the Hamiltonian within the central region. The listed references [86–89] are just a few examples of the one and two-probe DFT models outside of the current study if the reader is interested in further exploring its application to a wide array of research problems.

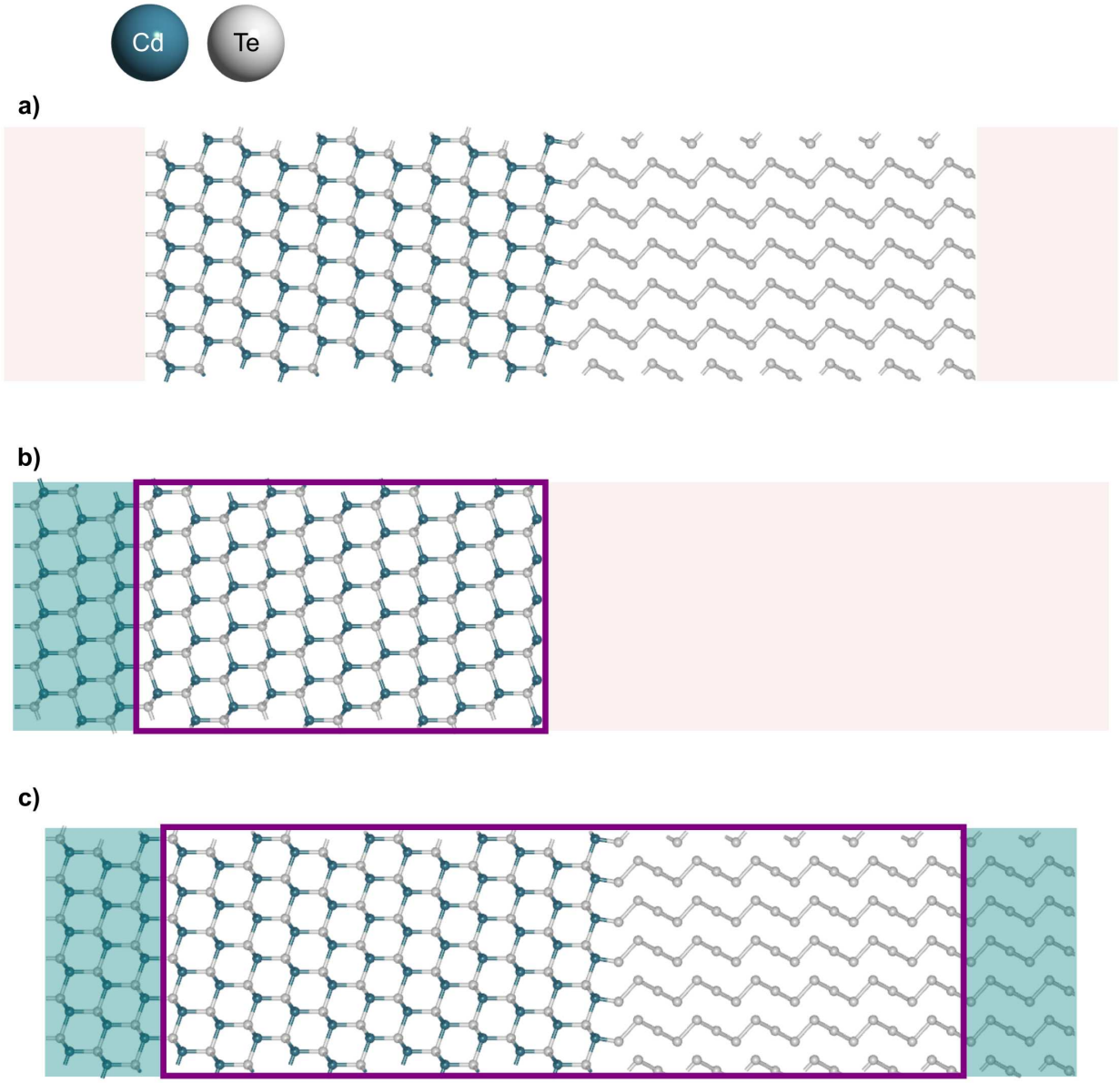

Figure 2.9: (a) Typical DFT slab configuration with vacuum on the ends (transparent pink) to model surfaces or interfaces. (b) Surface configuration of CdTe using the one-probe DFT model that contains one bulk left electrode for CdTe (transparent green), a surface region (purple box), and a vacuum region (transparent pink). (c) Device configuration of a CdTe/Te interface using the two-probe model that consists of semi-infinite left and right bulk electrodes (transparent green) for CdTe and Te, respectively, and a central region (purple box).

Chapter 3

DFT+GF One-Probe Modeling of CdTe Surfaces

Electronic properties residing at surfaces constitute a major role within thin film semiconductor device physics [90]. The surface region of semiconductor materials is often classified as a two-dimensional defect that tends to influence important electronic properties during the formation of interfaces. At the same time, the extension of surface effects is highly dependent on what type of defects exists in the localized region. As PV device configurations continue to decrease in size, it is becoming increasingly necessary to have a detailed atomic-scale perspective of electronic properties along thin film semiconductor surfaces. Therefore, quantum-based DFT+GF method was selected to accomplish the surface studies investigated within the current research. The main objective of DFT+GF surface studies was to understand the electronic behavior of surfaces and their relationship to interfaces regarding energy band alignment of CdTe-based heterostructures. The mechanisms related to plane orientation, termination layer, surface reconstruction and geometry optimization were investigated as a direct approach to classifying how such mechanisms influence CdTe-based surfaces.

3.1 Theoretical Outlook of Semiconductor Surfaces

Simulation modeling of CdTe surfaces encompassed a wide range of parameters that gave a comprehensive outlook on surface energy band alignment. As initially stated in Section 1.2, the Anderson Rule does not apply for energy band alignment along surfaces because the theory relies on knowing the band offsets at interfaces. Since only the CdTe surface is analyzed without an independent front or back layer joined to it to form a junction, then the Anderson Rule simply breaks down in accurately determining energy band alignment of the CdTe surface. The DFT+GF method gives the advantage of calculating spatially dependent energy band alignments for CdTe surfaces as a function of plane orientation, termination layer and relaxation. Surface reconstructions were included later in the research work to evaluate how surfaces that obey the electron counting rule

(ECR) [91, 92] affect electronic states at the CdTe surface. In Section 1.3.1, three of the four key hypotheses were primarily related to the electronic characteristics found at certain CdTe surfaces. The following subsections will briefly provide the theoretical basis necessary for explaining the CdTe surface results presented later in the chapter.

3.1.1 CdTe Surface Polarity

From the bulk CdTe results presented in Section 2.2, there was clear evidence that many mechanical and electronic properties were dependent on certain directions within the real CdTe conventional unit cell (i.e. elasticity, hole effective mass, etc.). The planes along which the CdTe bulk material is cleaved to create distinct surfaces are thus expected to show a diverse collection of electronic properties. There are a plethora of facet orientations that can be studied, however the current research focuses on the polar {111} and {100} planes along the respective terminations.

Regarding the zinc-blende form of the CdTe crystal structure, the unit cell can be constructed by alternating Cd and Te planes along the [111] direction as shown in Figure 3.1. Past studies have shown that various plane orientations of the CdTe crystal exhibit surface polarity [93–96] characteristics that may influence the electronic properties at the junctions. Along the CdTe{111} family of planes, the atoms along the termination layer are described to be triply bonded to the subsequent layer beneath due to sp^3 orbital hybridization of the CdTe compound; the sp^3 orbital hybridization is similar to that seen for III-V semiconducting compounds [97]. To illustrate for the Cd-terminated CdTe(111) plane, Figure 3.1a depicts that in the [111] direction the termination layer of Cd atoms are triply bonded with the Te atoms. The same is true for the Te($\bar{1}\bar{1}\bar{1}$) plane, which after incorporating a 180° rotation about the [$\bar{1}$10] direction in Figure 3.2a, the Te-terminated surface atoms also exhibit a triply bonded structure with the underlying Cd atoms. Experimental evidence suggests that epitaxial growth of the CdTe surface along the ($\bar{1}\bar{1}\bar{1}$) Te-terminated surface yields the best crystal growth [96]. However, the current DFT-based study was done to verify which particular termination layer along the {111} planes actually gives favorable electronic properties for band alignment of CdTe PV surfaces.

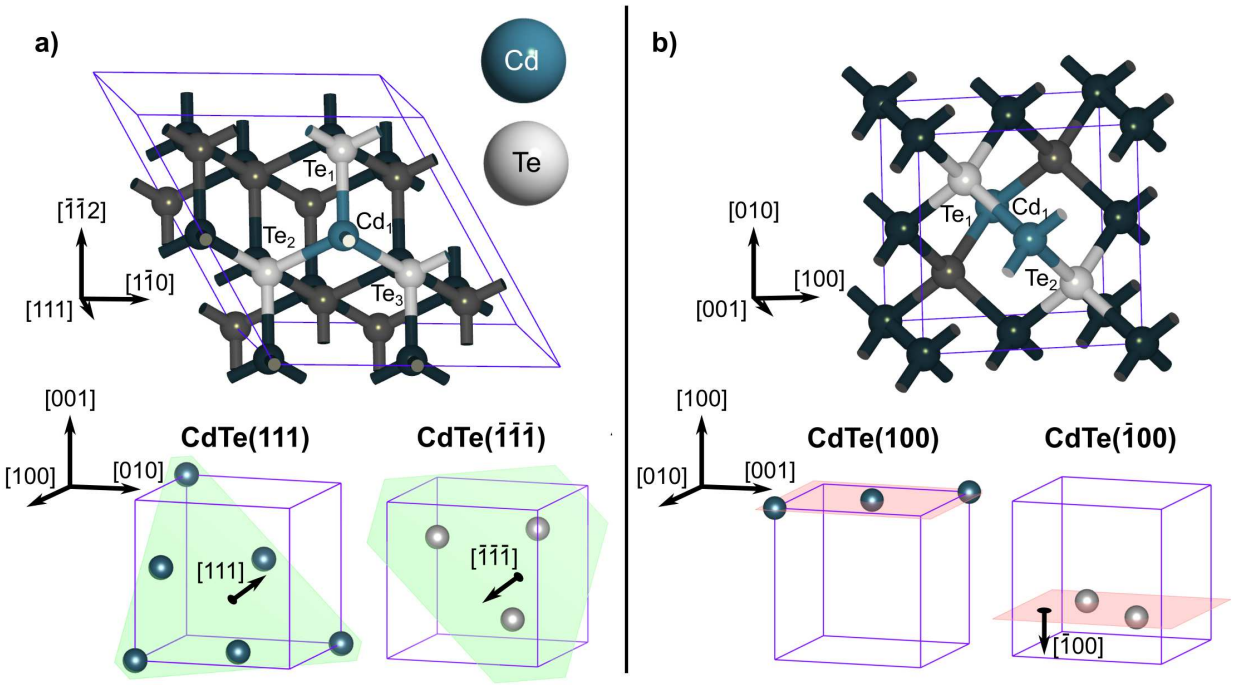

Figure 3.1: Illustration of the (a) {111} and (b) {100} facets of the zinc-blende CdTe structure. The top inset images show the number of Te atoms bonded to the Cd atom along the normal direction of the plane being viewed. The lower inset images in (a) provide colorized planes marking the close-packed (111) and ($\bar{1}\bar{1}\bar{1}$) planes of the CdTe conventional unit cell. The lower insets images in (b) are colorized planes along the (100) and ($\bar{1}$00) CdTe planes, respectively (lattice plane orientation structures generated with the *Vesta* software program [98]).

The bonding configuration along the CdTe(100) and ($\bar{1}$00) facets is displayed in Figure 3.1b. Two Te atoms are bonded to the Cd atom above it, and the cycle repeats in the <100> direction. If a surface where to form after cleaving along the (100) plane, then each termination layer atom would be doubly bonded with the layer beneath it. The CdTe{100} termination layers were expected to have some type of polarization as the termination surface is either a Cd or Te monolayer. However, Holt et al. [95] have stated that CdTe{100} planes can be classified as macroscopically non-polar surfaces if demi-steps (each with a Cd and Te facet step) are considered. The instance when CdTe polarity was said to be applicable was along the <110> directions where closest neighboring atoms of the same species along the {100} planes were present. It was not known how a macroscopically non-polar surface would behave in terms of its energy band alignment and whether such a macroscopic condition meant that no surface states were present. Thus, the current work investigated how an atomic-scale perspective of the CdTe{100} surfaces would determine the electronic properties along the {100} facets.

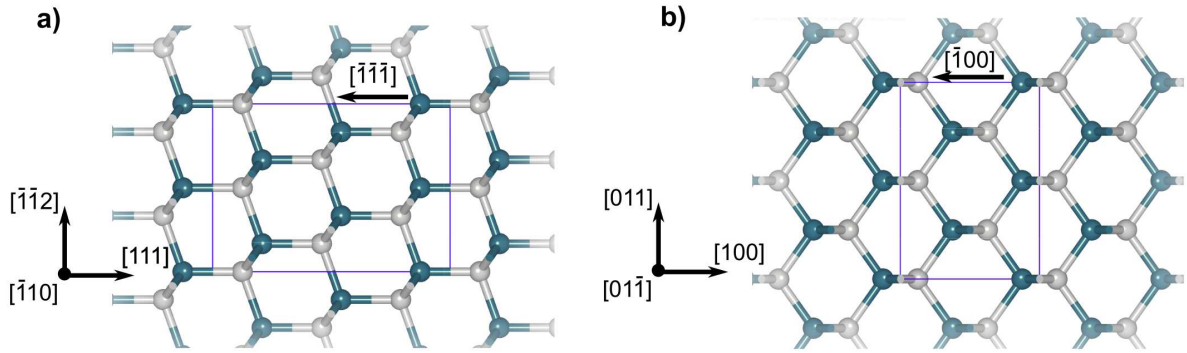

Figure 3.2: Sideview of the alternating Cd and Te atoms along their respective (a) <111> and (b) <100> directions.

According to previous studies, CdTe surface polarity is dictated by the termination layer as well as the bonding configuration at the CdTe surface. Although the {111} and {100} planes were known to be polar surfaces based on their termination layers, it was not known which facet would be favorable for energy band alignment. The first hypothesis of the study stated that the two plane orientations were expected give similar energy band alignment profiles if the planes

terminated along the same species (Cd or Te). The initial expectation was that the termination layer would play the primary role in the electronic properties of the CdTe surfaces in comparison to the bonding arrangement along the observed facet. Section 3.3 evaluates the two facets for both the Cd-terminated and Te-terminated CdTe surfaces and provides surprising insights on their actual effects on energy band alignment. Before constructing DFT simulations to test the hypothesis and analyze the results in-depth, the conceptual basis of how surface electronic properties are perceived needed to be established. The next subsection will provide a simplified treatment of surface theory and how it is used to develop the conclusions obtained from the DFT+GF simulation results.

3.1.2 Surface Theory

According to surface theory, the position of the Fermi level at the surface of a semiconductor is sensitive to the distribution of surface states that lead to Schottky barrier potentials [99]. As a result, band bending occurs depending on where the surface chemical potential state lies with respect to the Fermi level of the bulk semiconductor [100]. Typically, surface bands are partly filled with its chemical potential μ_{CN} lying within the bandgap of the bulk semiconductor material (Figure 3.3a). Charge neutrality (CN) must be maintained throughout the system, which requires the equilibration of occupied states between the surface band and valence band of the bulk semiconductor. Figure 3.3b illustrates the band bending formation that occurs during the equilibration of occupied states near the surface region of the semiconductor.

The equilibration of states leads to charge build up at the surface depending on the energy positions of the surface (μ_{CN}) and bulk semiconductor (μ_{SC}) chemical potentials. Equilibration at the surface develops a depletion width some distance into the bulk that follows a quadratic dependence on the depletion width size z_{dep} for the electrostatic potential $V(z)$ as shown in 3.1:

$$V(z) = \frac{e^2 N_A}{2\epsilon\epsilon_0}(z - z_{dep})^2 \tag{3.1}$$

If the surface charges positively as a result of equilibration ($\mu_{CN} < \mu_{SC}$), then the bands will bend downward according to (3.1). The opposite is true in that a negatively charged surface

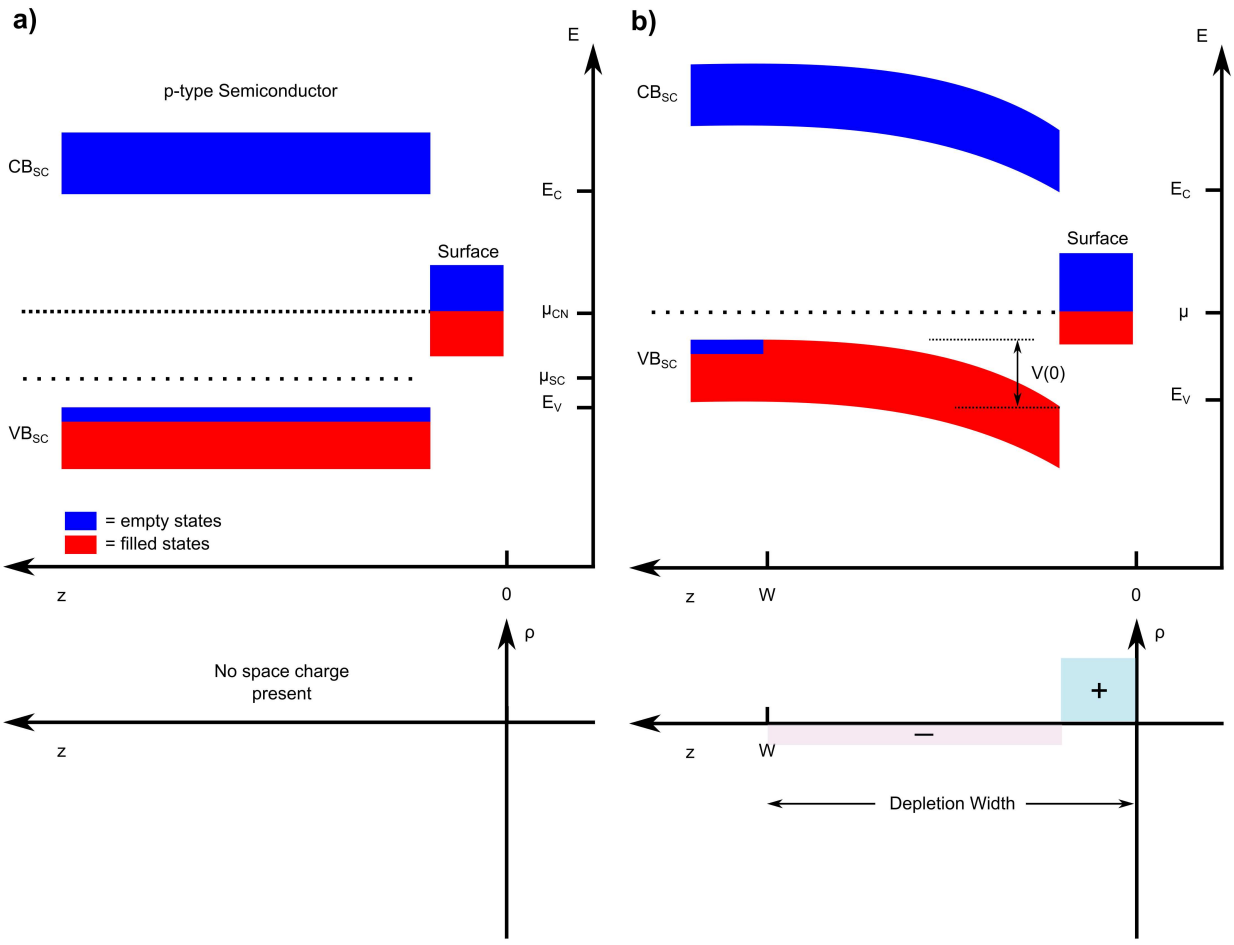

Figure 3.3: Band bending illustration (a) before equilibration, and (b) after equilibration is achieved in a p-type semiconductor where $\mu_{CN} > \mu_{SC}$.

($\mu_{CN} > \mu_{SC}$) will cause the bands to bend upward. It must be noted that the number of ionized acceptors N_A (or donors N_D) magnify the band bending at the surface as they must be filled (depleted) to neutralize the surface charge. The surface polarity is directly related to band bending features explained by surface theory. Any surface electronic states present will play an additional role to the surface polarity effect that influences charge distribution at the surface.

Although surface theory gives a general perspective on the effects of surface states, it does not explain how different types of plane orientations or terminated surfaces drive the mechanisms leading to surface state formation. That is why the current research work uses an atomistic modeling approach based on DFT to reveal the nuances of terminated surfaces and their alterations to electronic surface behaviors. The implications of surface theory in relation to the predicted electronic

features of CdTe surfaces using atomistic modeling make up the second and third hypotheses from Section 1.3.1. As a reminder, the second hypothesis stated that the energy band alignment of the Cd-terminated surfaces were not expected to have detrimental surface electronic states and would simply bend downward. On the other hand, the Te-terminated surfaces were thought to contain surface states due to dangling bonds present at the termination layer and bend the bands upward. As for the third hypothesis, chlorine in the tellurium sites of the Te-terminated CdTe surface was predicted to passivate the dangling bonds that existed for the CdTe($\bar{1}\bar{1}\bar{1}$) facet. At the same time, a monolayer of TeO_2 was anticipated to further reduce any detrimental surface states present along the Te-terminated CdTe surface. The hypotheses were tested using the DFT+GF method to determine whether the simulation results validate or refute them.

One last topic needs to be covered before moving forward with the computational results and discussion. The subject is pertaining to surface reconstruction and how it contributes to the overall CdTe surface characteristics.

3.1.3 Surface Reconstructions

Surface reconstruction is quite an involved discussion for epitaxial processes with subtopics that are beyond the scope of the present research study. Yet in the context of the second hypothesis, it was deemed necessary to include several important surface reconstructions within the DFT+GF models as they became crucial to the understanding of surface charge neutrality.

The topic of surface reconstructions was initially overlooked during the construction of the hypotheses. They are mostly applicable to the second hypothesis mentioned above, which failed to incorporate the importance of the electron counting rule (ECR, briefly mentioned in Section 3.1.2) [91,92] to the determination of favorable CdTe surfaces. Surface reconstructions are the rearrangement of the surface periodicity leading to an overall lower energy of the system. The resulting surface reconstructions may or may not obey the ECR conditions, which cause the surface to be charge neutral across it.

Recall that the bonding arrangement of the zinc-blende CdTe structure follows an sp^3 orbital hybridization, similar to the III-V semiconducting compounds like GaAs [97,101]. If the CdTe surface were to be cleaved along a polar surface like the {111} family of planes, then there would be the formation of filled dangling bonds on the anion (Te) terminated surface while empty dangling bonds would reside on the cation (Cd) terminated surface. Figure 3.4 illustrates the hybridization of the CdTe compound and the arrangement of the electrons after the structure is cleaved along the (111) plane. One way that newly formed surfaces can obey the ECR would be to create the necessary amount of atomic vacancies or adatoms on the surface that balance the surface charge distribution. For the both of the Cd and Te-terminated cases, the c(2×2) and (2×2) reconstructions along the respective CdTe(100) and CdTe(111) facets were investigated. All reconstructed CdTe surfaces were chosen to identify how the ECR affected the energy band alignment profiles.

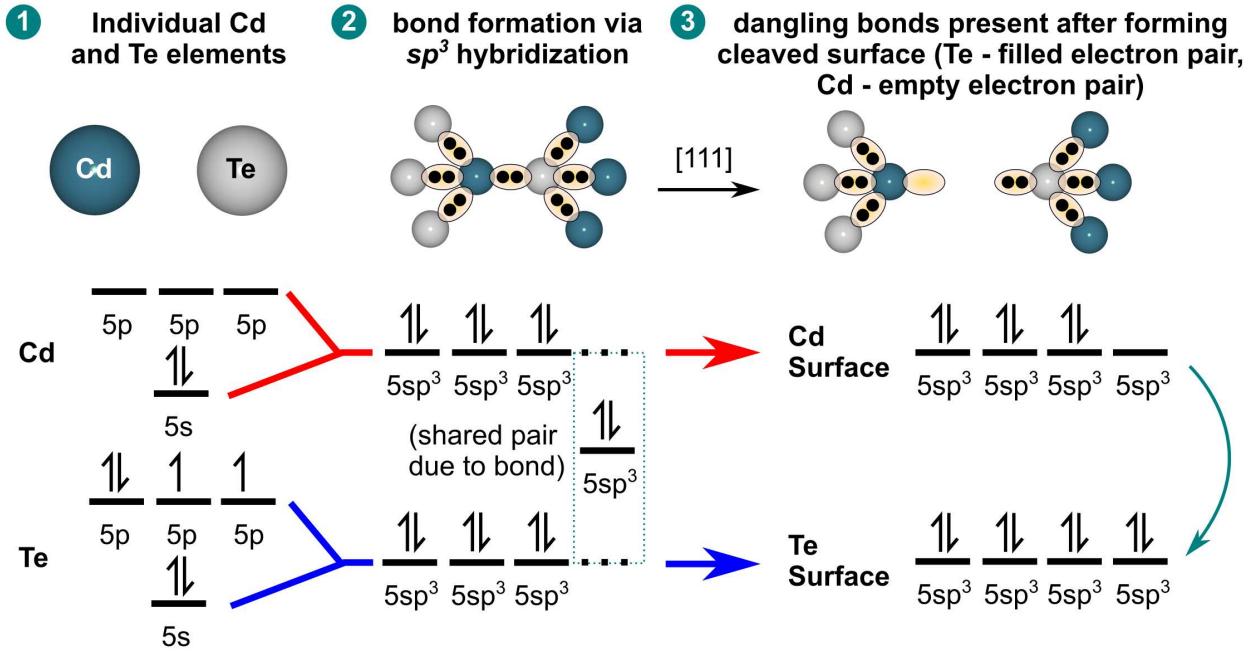

Figure 3.4: Schematic of the bonding configuration within CdTe following the sp^3 orbital hybridization structure. After cleaving along the single bond between the Cd and Te atom in the [111] direction, the Cd atom in the CdTe(111) facet adopts one empty dangling bond while the Te atom on the CdTe($\bar{1}\bar{1}\bar{1}$) facet retains both electrons to form a filled dangling bond.

3.2 Computational Details

The DFT and surface Green's function one-probe modeling setup within the QuantumATK software package was the simulation of choice for all CdTe surface configurations [62]. All simulations used the Perdew-Zunger [71] form of the LDA exchange-correlation functional along with the semi-empirical Hubbard-U energy applied to the Cd-4d and Te-5p orbitals to ensure proper bandgap values. The selected pseudopotential and basis set combination as described in Section 2.2.2 was the FHI+OMX [67, 68] pseudopotentials along with the double-zeta polarized and s2p2d1 (low) basis sets, respectively. A density mesh cutoff of 2200 eV was used in all calculations. For the CdTe{100} family of planes, a k-point sampling of 3 $\times$ 3 $\times$ 150 (4.376 Å $\times$ 4.376 Å $\times$ 154.699 Å) was implemented while for the CdTe{111} family of planes the k-point sampling was 4 $\times$ 4 $\times$ 100 (5.052 Å $\times$ 5.052 Å $\times$ 178.631 Å). A Monkhorst-Pack grid distribution was set as the standard for all simulations. Each model incorporates a small p-type doping concentration of 2 $\times$ 10^{14} cm^{-3} to remain consistent with typical concentration values found in real CdTe-based PV devices. Spin-orbit splitting was not included in any of the calculations.

Each one-probe model included a semi-infinite CdTe bulk electrode coupled with a CdTe surface region of approximately 20 nm in length and a 5 nm vacuum region to represent the terminated surface (see Figure 3.5). The experimental lattice parameter of 6.480 Å was maintained for both the bulk electrode and first 15 nm of the surface region so as to maintain the structural integrity seen in experimental CdTe thin films. The last 5 nm of the atoms in the surface region from the terminated surface had their atomic positions geometrically optimized until all forces reached below 0.01 eV/Å. The region between the CdTe bulk electrode and the CdTe surface region adopted a Dirichlet boundary condition so that the electronic structures of the two regions were coupled together and mimic a semi-infinite bulk region for CdTe. Towards the right of the modeling domain is the vacuum region, which implements a Neumann boundary condition so that the gradient of the electrostatic difference potential with respect to length did not change at the surface (i.e. $d(\delta V)/dr|_{r=L_{z,surf}} = 0$). The one-probe modeling setup ensures that the Poisson solver would accurately converge the electronic structure of each CdTe termination case.

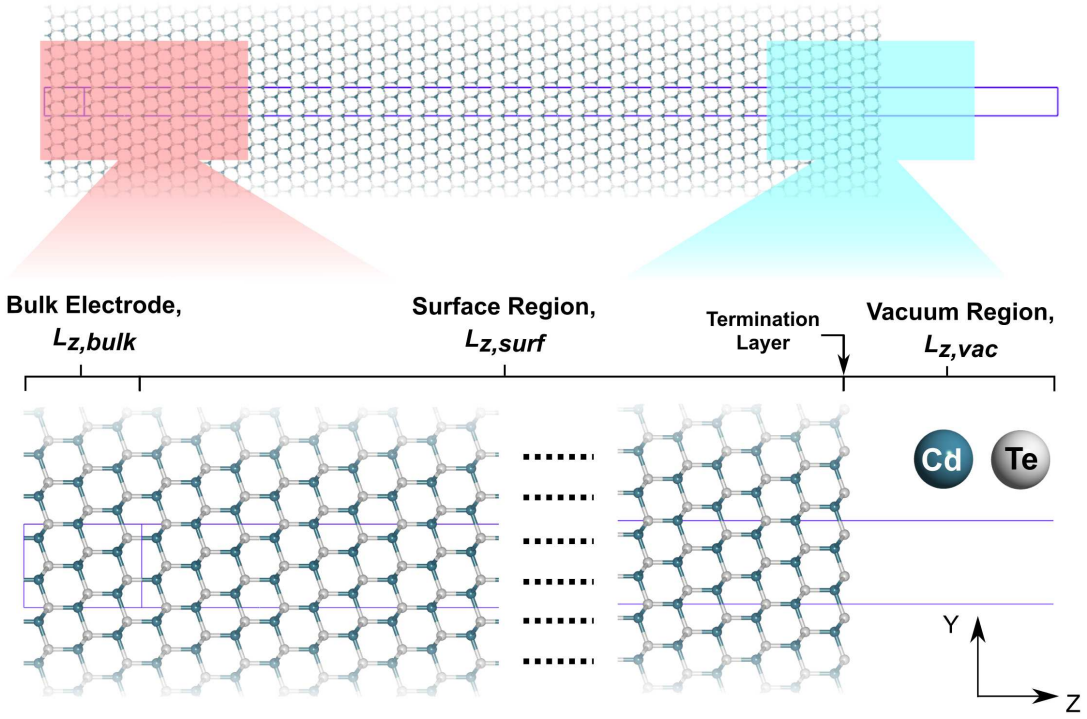

Figure 3.5: One-probe surface model illustration projected along the YZ plane. The red and blue highlighted regions of the surface model are zoomed in at the bottom subfigures. The bulk electrode length $L_{z,bulk}$ depends on the plane orientation of the surface.

Several simulations were performed to create an expanded perspective of energy band alignment based on unique CdTe surface arrangements. Table 3.1 displays all one-probe DFT+GF modeling parameters and domain sizes during the calculations. As a general overview for Section 3.3, each subsection is divided by its respective terminated surfaces with data presented for both the {100} and {111} facets or just the {111} cases only. Two termination layers labeled as Cd-terminated and Te-terminated were investigated separately within each oriented plane category. Furthermore, Cl_{Te} formation on the CdTe($\bar{1}\bar{1}\bar{1}$) surface was simulated to evaluate any additional effects on the energy band alignment. Lastly, a TeO_2 monolayer without and with Cl_{Te} along the CdTe(111) surface was studied independently to determine their influence on band alignment characteristics.

Table 3.1: One-probe DFT+GF modeling domain sizes used in all investigated CdTe surface studies. "u" denotes unrelaxed while "r" denotes relaxed CdTe surface models.

Termination Layer	Facet	$L_{z,bulk}$ (Å)	$L_{z,surf(u)}$ (Å)	$L_{z,surf(r)}$ (Å)	N_{bulk}	N_{surf}
Cd	$CdTe(100)_{(1\times1)}$	6.480	213.030	215.827	16	528
	$CdTe(100)_{c(2\times2)}$	6.480	213.030	213.116	16	526
	$CdTe(111)_{(1\times1)}$	11.224	223.071	225.034	24	480
	$CdTe(111)_{(2\times2)}$	11.224	223.071	222.281	24	479
Te	$CdTe(\bar{1}00)_{(1\times1)}$	6.480	213.030	213.519	16	528
	$CdTe(\bar{1}00)_{c(2\times2)}$	6.480	213.030	214.322	16	528
	$CdTe(\bar{1}\bar{1}\bar{1})_{(1\times1)}$	11.224	223.071	223.877	24	480
	$CdTe(\bar{1}\bar{1}\bar{1})_{(2\times2)}$	11.224	223.071	223.993	24	479
Cl_{Te}	$CdTe(\bar{1}\bar{1}\bar{1})_{(1\times1)}$ + 25% Cl_{Te}	11.224	223.071	223.854	24	480
	$CdTe(\bar{1}\bar{1}\bar{1})_{(1\times1)}$ + 25% Cl_{Te} + V_{Cd}	11.224	223.071	223.079	24	479
	$CdTe(\bar{1}\bar{1}\bar{1})_{(1\times1)}$ + 50% Cl_{Te}	11.224	223.071	223.857	24	480
TeO_2	$CdTe(111)_{(1\times1)}$ + TeO_2	11.224	223.071	222.764	24	484
	$CdTe(111)_{(1\times1)}$ + TeO_2 + 25% Cl_{Te}	11.224	223.071	222.089	24	484
	$CdTe(111)_{(1\times1)}$ + TeO_2 + 50% Cl_{Te}	11.224	223.071	221.568	24	484

3.3 Results and Discussion

Comparisons between electronic characteristics of differing CdTe surface grain orientations and terminated layers were made to gain an overall perspective of defect surface states and band bending effects associated with certain terminated surfaces. Local density of states projected along the direction perpendicular to the surface plane of the CdTe surfaces were plotted to describe the energy band alignment features for a given surface of CdTe. Projected local density of states (PLDOS) analyses for each SCF-converged calculation was done with an 11 x 11 k-point sampling. PLDOS is a convenient way for visualizing the electronic structure of the DFT+GF one and two-probe models in the transport direction and will be extensively used throughout the rest of the document for energy band alignment.

Relevant electronic characteristics measured from the energy band alignment plots such as band gap energy $E_{g,CdTe}$, respective valence and conduction band surface energy potentials $E_{(v,c),surf}$ and internal cusp energy potential $E_{v,cusp}$ (if any exists) were reported in the tables of each subsection for the plane orientations under scrutiny. The two most prominent surface electronic state energy levels (E_{def1} and E_{def2}, respectively) as well as their DOS magnitudes ($D(E_{def1})$ and $D(E_{def2})$, respectively) were tabulated in a separate table for each subsection as well.

A standard for measuring electronic features such as the CdTe band gap, surface and internal cusp energy potentials was established by using macroscopically averaged curve fits of the VBM and CBM with a Gaussian kernel width of 5 Å. The Gaussian kernel width was chosen so that the curve fits for VBM/CBM would minimize the oscillatory effects of tracing between alternating Cd and Te layers. Too large of a width value resulted in the shrinking of the curve fits as wider Gaussian widths required more data slices to smoothen the curve traces. Furthermore, a DOS threshold of 10^{-4} eV^{-1} was selected as done in another DFT-LCAO study [55] to distinguish between the band edges and background noise during the tracing process.

Using the macroscopically averaged curve fits of the VBM and CBM, the band gap energy $E_{g,CdTe}$ was consistently determined from the energy differences of the VBM and CBM at positions located closest to the bulk-like CdTe electrode region (the leftmost part of each surface region).

The Hubbard-U values U_{Te-5p} = 2.55 eV and U_{Cd-4d} = 4.60 eV described in Section 2.2.2 have accurately described the energy band gap values for the CdTe bulk electrodes to ensure transferability in the one-probe modeling setup.

In the context of the macroscopically averaged curve fit for the VBM, the surface potential $E_{v,surf}$ is defined as the energy difference between the VBM curve fit value nearest the surface and the curve fit VBM value of the CdTe bulk-like region. Both of the specified locations are respectively labeled as points 1 and 2 in Figure 3.8a and follow the same definition thereafter. Depending on whether it bends upward or downward, $E_{v,surf}$ acts as either a barrier (negative magnitude, bending downward) or an enhancer (positive magnitude, bending upward) for hole transport toward the back of a typical p-type CdTe PV device. A similar definition is applied to the CB surface potential $E_{c,surf}$ if it was measured within the given study. In accordance with the labels provided in Figure 3.9b, the cusp energy potential $E_{v,cusp}$ is simply defined as the energy difference between the peak of the curve fit VBM (labeled point 1) and the leftmost part of the same curve fit (labeled point 2). The length $\delta_{v,cusp}$ marks the position where the cusp energy potential begins with respect to the surface region length $L_{z,surf}$.

The two surface states with the highest DOS magnitudes were recorded as E_{def1} and E_{def2} in separate tables for each subsection and were measured within 5 Å from the termination layer. This was done to maintain consistency with where the most prominent surface electronic states were evaluated in each modeling case.

3.3.1 Cd-Terminated Surfaces

Research Scope

In CdTe-based PV technologies, CdTe surfaces are a critical limiting factor in solar cell efficiencies. Research studies indicate that CdTe surface characteristics dictate minority carrier lifetimes that affect CdTe device performance [102]. However, the relationship between preferential plane orientations of CdTe surfaces, if any exist, to the optimization of junctions within CdTe PV devices are not well understood [33]. CdTe terminated surfaces will exhibit differing polarities depending

upon which plane orientation and termination layer (Cd or Te) is examined [93,95,96]. As a result, various plane orientations of the CdTe surface will influence the electronic properties in the device, especially in areas where interfaces form.

A detailed understanding of the electronic characteristics of CdTe surface plane orientations is essential to the advancement of CdTe device fabrication processes. In this subsection, the DFT+GF method has been utilized for studying the electronic properties found in Cd-terminated CdTe(100) and (111) surfaces [103]. Both the unreconstructed and commonly seen reconstructed CdTe surfaces for the (100) and (111) plane orientations have been simulated to evaluate the energy band alignment characteristics for each case. The pertinent features calculated in the band alignment diagrams were quantified and compared to understand their effect on carrier charge transport within CdTe-based thin film PV devices.

Relaxation Effects

As shown in Figure 3.6 and Figure 3.7, the respective CdTe(100) and CdTe(111) plane orientations have underwent relaxation (GO) of their surfaces to see how it affects energy band alignment. The transition that occurs between Figure 3.6a and Figure 3.6b shows the dramatic effect that geometry optimization has on the unreconstructed CdTe(100) surface as the surface deviates from an ordered set of Cd and Te rows. More specifically, the Cd atoms along the horizontal boundaries of the unit cell in the top view of Figure 3.6b tend to move toward each other by 1.854 Å. It is notable that the CdTe(100) surface flattens out with a single Cd atom being displaced 2.794 Å from the topmost relaxed layer. Using the unrelaxed CdTe(100) atomic positions as a reference, the Cd-termination layer and the Te layer beneath it expand by 0.252 Å and 1.642 Å respectively in the [100] direction. Similar flattening of the surface due to relaxation is seen between the c(2 $\times$ 2) CdTe(100) surface going from Figure 3.6c to Figure 3.6d. With the c(2 $\times$ 2) unrelaxed case as the reference, the c(2 $\times$ 2) CdTe(100) surface slightly expands by 0.086 Å with the Te layer beneath it expanding by 1.713 Å. The observed relaxation effect is due to the removal of two Cd atoms from the termination layer and at least for the c(2 $\times$ 2) case has been observed in other DFT-based studies [45, 46]. It must be noted that the relaxation procedure as well as the one-probe surface

setup in the present work lead to different values for the c(2 $\times$ 2) CdTe(100) atomic positions in the [100] direction. However, the quantitative differences may also be attributed to the greater relaxation region used in the present work. Nonetheless, the two Cd vacancies lead to a rearrangement of charge that causes the underlying Te layer to expand in the [100] direction to compensate the effect. The preferred undimerized flat structure obeys the ECR for the Cd-terminated c(2 $\times$ 2) CdTe(100) surface [46, 104] since the number of empty cation (Cd) dangling bonds is equal to the number of fully occupied anion (Te) dangling bonds. As a result, the dramatic relaxation effects observed in the CdTe(100) unreconstructed and reconstructed surfaces directly influence the energy band alignment diagrams and their associated surface electronic states as presented in the next subsection.

Regarding the CdTe(111) plane orientations, Figure 3.7 provides a clear indication that the (2 $\times$ 2) surface reconstruction is the energetically minimized facet. This is validated by the fact that after the original CdTe(111) unrelaxed surface in Figure 3.7a undergoes relaxation, a single Te atom is displaced 2.899 Å from its original position in the [111] direction. After relaxation, the CdTe(111) (1 $\times$ 1) surface tends to have Te atoms residing closer to the surface. The atomic displacements of the relaxed surface lead to the force-minimized cross-section found in Figure 3.7b, which appears to be quite disordered in relation to its unrelaxed state. On the other hand, the (2 $\times$ 2) CdTe(111) facet before and after relaxation as seen in Figure 3.7c and Figure 3.7d, respectively, maintains a well-behaved surface arrangement along the cross-sectional view due to the Cd vacancy. Most of the atoms in the topmost Cd layer of the CdTe(111) (1 $\times$ 1) surface minimally compress by 0.174 Å while the underlying Te layer expands by 0.808 Å in the [111] direction. For the CdTe(111) (2 $\times$ 2) surface, the compressive and tensile displacements for the Cd and Te topmost layers are 0.471 Å and 0.557 Å, respectively. Qualitatively, the resulting displacements and formation of flat CdTe(111) surfaces are in agreement with other calculations [47, 48]. Again, the explanation for the resulting planar surface leads back to the (2 $\times$ 2) CdTe(111) surface obeying the ECR in a similar manner as the III-V semiconducting compounds [92, 105]. Within the cross-sectional unit cell of the unreconstructed CdTe(111) surface, there are an equal number of cations and anions

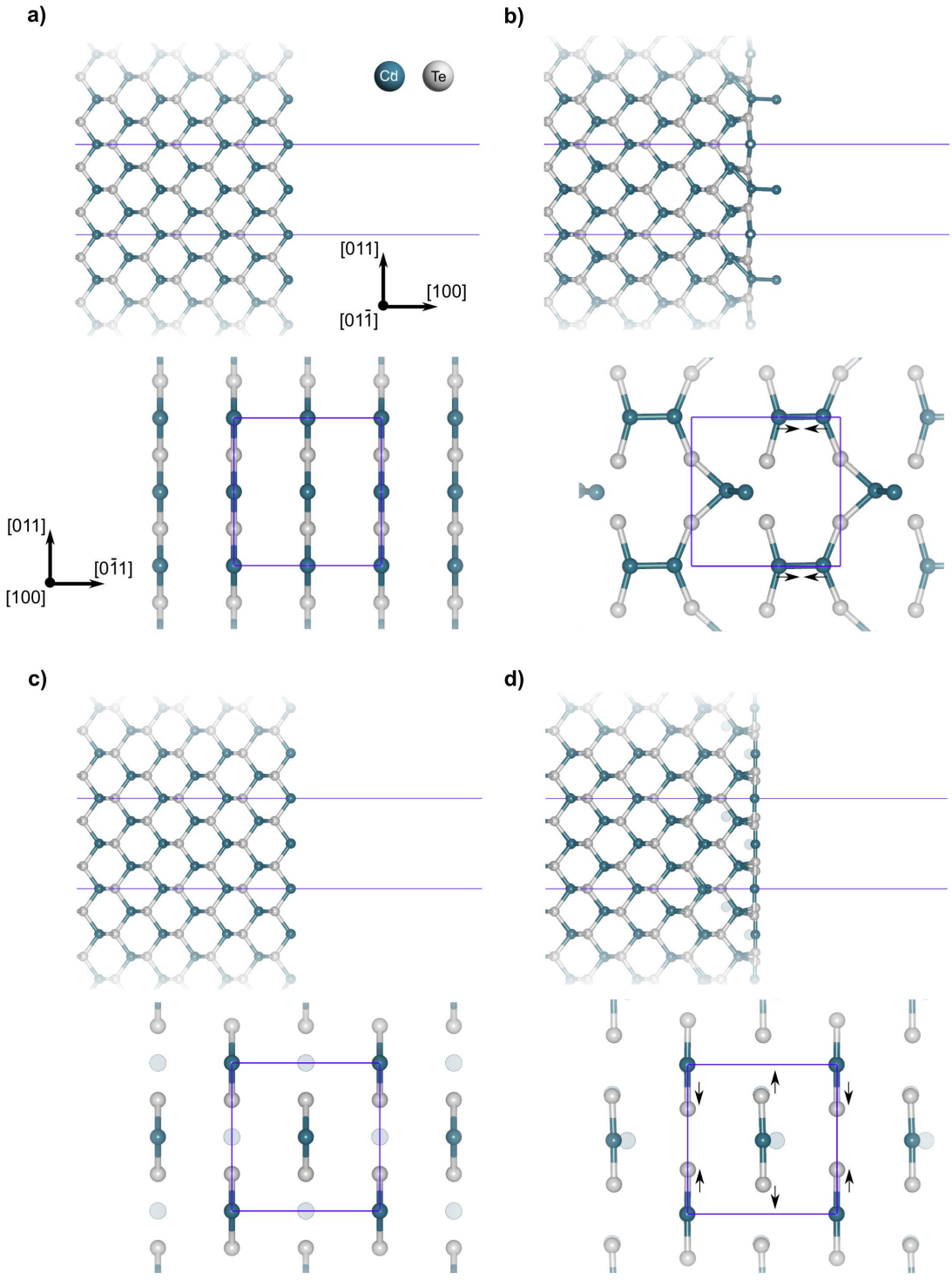

Figure 3.6: Perspective views of the respective unrelaxed and relaxed atomic configurations of (a,b) the (1 $\times$ 1) unreconstructed and (c,d) the c(2 $\times$ 2) reconstructed CdTe(100) surfaces. Two views are shown along the transport direction (top subfigure) and perpendicular directions (bottom subfigure) of the one-probe models. The perpendicular view only shows the last two atomic layers in the surface domain for clarity. All surfaces are visualized using the indices provided in (a). The "ghost" atoms are shown as translucent circles in (c,d).

present, each of which exhibit sp^3 orbital hybridization. After removing one Cd atom, each of the three underlying Te atoms that were bonded to the Cd atom are left with occupied dangling bonds. Geometry optimization of the (2 × 2) CdTe(111) surface allows for atomic layers to shift accordingly to ensure the surface maintains charge neutrality. Thus, the underlying Te layer moves closer to the Cd termination layer, causing the three occupied dangling bonds from Te to be eliminated by the empty dangling bonds from the remaining three Cd surface atoms in the cross-sectional unit cell. The (2 × 2) CdTe(111) surface has been observed experimentally over a wide temperature range [106], proving its stability as the favorable facet for the CdTe(111) cases.

Energy Band Alignment

Table 3.2: Salient electronic features within each (100) and (111) CdTe one-probe model. $\delta_{v,cusp}$ indicates the position where the cusp energy potential $E_{v,cusp}$ is determined starting from the termination layer. All energy band alignment values are determined from the macroscopically averaged curve fit of each local density of states plot. Any +/- values indicate energy values referenced to the Fermi level E_F (marked as 0 eV).

Type	Facet	$E_{g,CdTe}$ (eV)	$E_{v,surf}$ (eV)	$\delta_{v,cusp}$ (Å)	$E_{v,cusp}$ (eV)
Unrelaxed	$CdTe(100)_{(1 \times 1)}$	1.49	-0.14	n/a	n/a
	$CdTe(100)_{c(2 \times 2)}$	1.47	+0.28	n/a	n/a
	$CdTe(111)_{(1 \times 1)}$	1.48	-0.38	n/a	n/a
	$CdTe(111)_{(2 \times 2)}$	1.47	+0.01	n/a	n/a
Relaxed	$CdTe(100)_{(1 \times 1)}$	1.49	-0.15	n/a	n/a
	$CdTe(100)_{c(2 \times 2)}$	1.50	-0.03	51.926	+0.05
	$CdTe(111)_{(1 \times 1)}$	1.40	+0.09	59.017	+0.33
	$CdTe(111)_{(2 \times 2)}$	1.46	-0.02	63.746	+0.07

Figure 3.8 shows the energy band alignment of the respective CdTe(100) one-probe models. As shown in Table 3.2, the band gap energies $E_{g,CdTe}$ for the CdTe(100) configurations lie between 1.47 eV and 1.50 eV, in agreement with the experimental value of 1.49 eV [34]. Figure 3.8a and Figure 3.8b are the respective unrelaxed and relaxed one-probe results for the (1 × 1) CdTe(100)

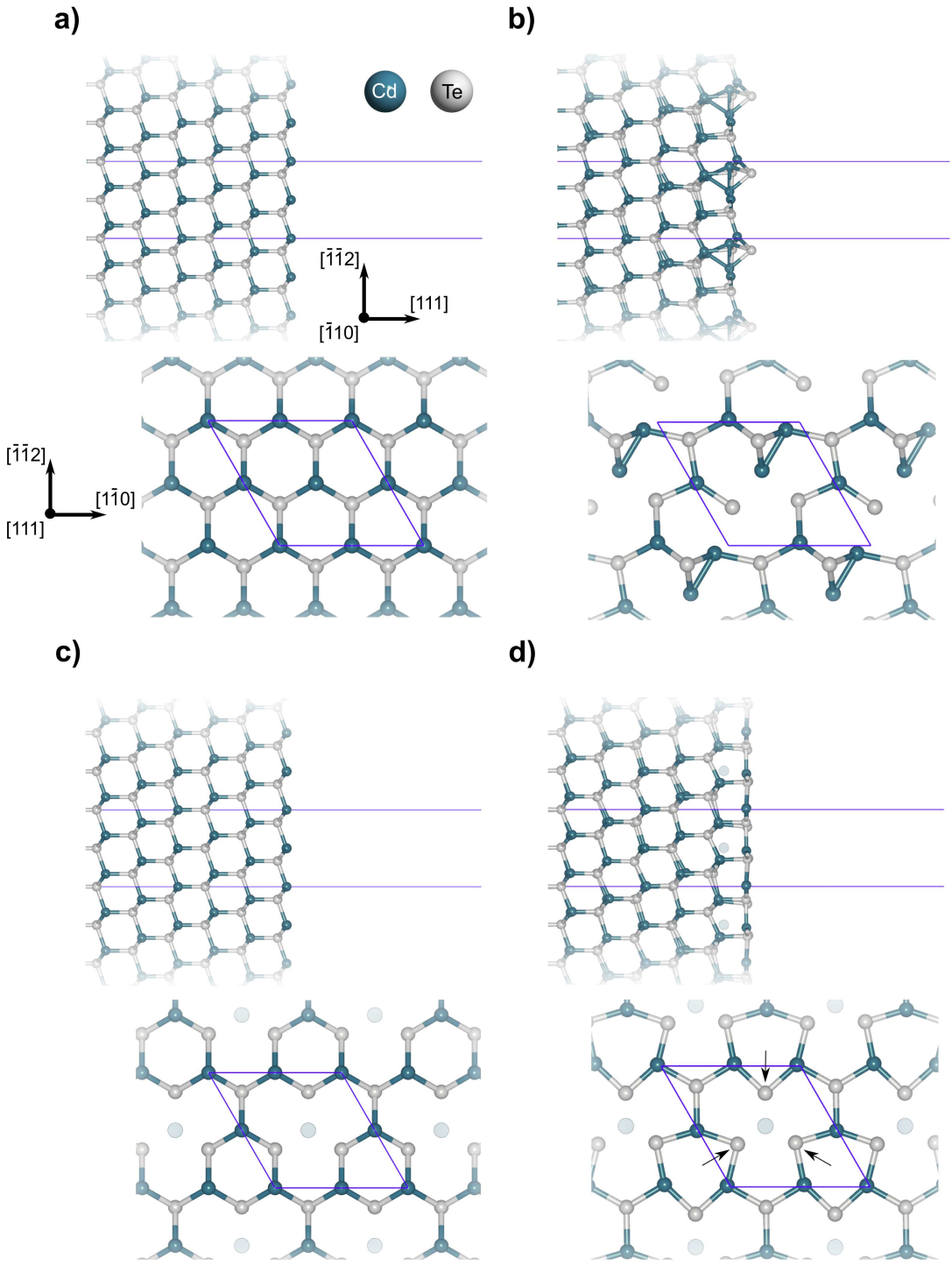

Figure 3.7: Perspective views of the respective unrelaxed and relaxed atomic configurations of (a,b) the (1 × 1) unreconstructed and (c,d) the (2 × 2) reconstructed CdTe(111) surfaces. Two views are shown along the transport direction (top subfigure) and perpendicular directions (bottom subfigure) of the one-probe models. The perpendicular view only shows the last two atomic layers in the surface domain for clarity. All surfaces are visualized using the indices provided in (a). The "ghost" atoms are shown as translucent circles in (c,d).

Table 3.3: Surface electronic state energy levels and DOS magnitudes within each (100) and (111) CdTe one-probe model. All electronic state energy values for a given facet are chosen according to highest DOS magnitude and are accurate to within ±5 meV.

Type	Facet	E_{def1} (eV)	$D(E_{def1})$ (eV^{-1})	E_{def2} (eV)	$D(E_{def2})$ (eV^{-1})
Unrelaxed	$CdTe(100)_{(1 \times 1)}$	+0.07	2.56×10^{-1}	+0.01	2.07×10^{-1}
	$CdTe(100)_{c(2 \times 2)}$	+0.61	1.47×10^{2}	+0.56	4.44×10^{-1}
	$CdTe(111)_{(1 \times 1)}$	+0.23	6.48×10^{-1}	-0.40	2.60×10^{-1}
	$CdTe(111)_{(2 \times 2)}$	-0.81	9.73×10^{-3}	-0.80	4.74×10^{-3}
Relaxed	$CdTe(100)_{(1 \times 1)}$	+0.62	5.98×10^{1}	-0.30	2.45×10^{1}
	$CdTe(100)_{c(2 \times 2)}$	+0.68	6.69×10^{-4}	-0.96	2.47×10^{-4}
	$CdTe(111)_{(1 \times 1)}$	+0.56	6.80×10^{-2}	+0.67	4.72×10^{-2}
	$CdTe(111)_{(2 \times 2)}$	+0.62	7.55×10^{-2}	+0.65	1.05×10^{-2}

surface. Figure 3.8c and Figure 3.8d are the respective unrelaxed and relaxed band alignment analyses corresponding to the c(2 × 2) CdTe(100) surface.

In the CdTe(100) unrelaxed case without reconstruction (Figure 3.8a), a shallow downward bend of -0.14 eV in the valence band forms while negligible band bending occurs in the conduction band. The valence band bending presents a barrier to the hole majority charge carriers that would lead to a decreased efficiency if all band alignment features at the back of the absorber layer were maintained in a complete CdTe device. Furthermore, a large range of surface state levels extending both above and below the Fermi level E_F appear at the CdTe(100) surface. The two biggest DOS magnitudes for the surface states in the one-probe model exist at +0.07 and +0.01 eV from the Fermi level. Surface electronic states closer to the Fermi level, at least from a first-order perspective, are potential avenues for Shockley Read Hall recombination within a CdTe device if the features were retained at the back of an equivalent CdTe(100) absorber layer. However, detrimental features are seen in the energy band alignment profile when GO is introduced to the (1 × 1) CdTe(100) surface. The relaxed surface shown in Figure 3.8b continues to have a downward valence band bend but now contains a wider range of surface state levels. It is evident that within the present modeling setup the relaxation effects actually worsen the surface states characteristics for the CdTe(100) (1 × 1) case. It is worth mentioning that the entire screening length of the

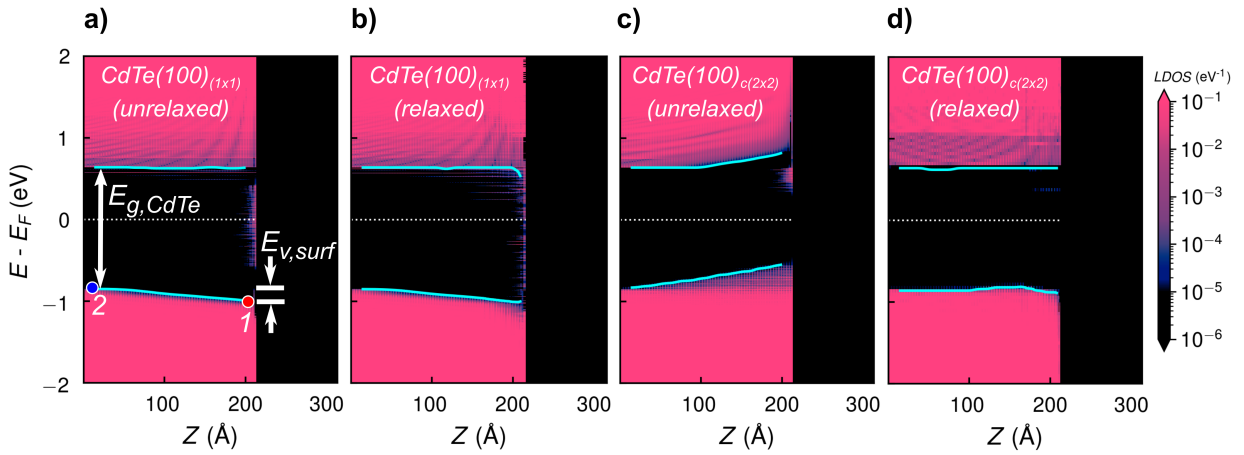

Figure 3.8: Localized density of states mapping across the unreconstructed and reconstructed CdTe(100) one-probe models separated as unrelaxed (a,c) and relaxed cases (b,d). Plane orientation and reconstruction type are provided in each image above. The zero energy on the y-axis is referenced by the Fermi level E_F of each respective band alignment profile. The light blue curves are the macroscopically averaged curve fits of the valence band maximum and conduction band minimum, respectively. Points 1 and 2 in (a) are used to determined the surface energy potential $E_{v,surf}$ with details provided in Section 3.3.

CdTe(100) (1 $\times$ 1) surface is not fully accomodated, which is why the VBM does not flatten out near the CdTe bulk region. One way to alleviate the bend would be with a higher doping concentration than the 2 $\times$ 10^{14} cm^{-3} value used in the current work. However, a lower doping concentration was used to reflect typical concentrations seen within intrinsic CdTe PV devices. In any case, the CdTe(100) (1 $\times$ 1) surface leads to unfavorable surface states and downward VBM bending that are harmful to hole carrier transport toward the back of p-type CdTe solar cell devices.

The CdTe(100) c(2 $\times$ 2) surface band alignment depicted in Figure 3.8c provides several noteworthy differences from the unreconstructed case. First, the valence band has a gradual upward bend of +0.28 eV as oppose to the negative downward bend seen in CdTe(100) valence band. By extension, the conduction band also slightly bends upward, which was not observed for the CdTe(100) (1 $\times$ 1) surface. The surface states levels E_{def1} and E_{def2} for CdTe(100) c(2 $\times$ 2) reside at least +0.50 eV above the Fermi level E_F in a concentrated manner rather than throughout the energy gap. The concentrated DOS of the surface electronic states is primarily due to the remaining Cd atoms at the CdTe(100) termination layer after creating two Cd vacancies. Since no GO has been applied to the surface yet, charge compensation has not been achieved along the CdTe(100)

c(2 $\times$ 2) surface and leads to the features seen in Figure 3.8c. Once GO is performed on the CdTe(100) c(2 $\times$ 2) facet, a flattening of the bands is achieved as shown in Figure 3.8d due to the force-minimized atomic displacements. As mentioned in the previous subsection, relaxation of the CdTe(100) c(2 $\times$ 2) surface into an undimerized, charge neutral surface leads to the fulfillment of the electron counting model. Along this facet, the surface energy potential $E_{v,surf}$ of -0.03 eV is both smaller and opposite in sign from the +0.28 eV surface potential found in the unrelaxed case. However, the surface states above the Fermi level have virtually disappeared as both surface states in Table 3.9 have a DOS magnitude of 10^{-4} eV^{-1}. The second surface state at -0.96 eV nearest the termination layer resides below the measured bulk VB for CdTe. This is simply due to the chosen Gaussian width of the macroscopic curve fit only tracing close to the surface based on how the Gaussian kernel is set up for averaging the VBM. A newly formed cusp energy potential with a small magnitude $E_{v,cusp}$ of +0.05 eV is created only for the CdTe(100) c(2 $\times$ 2) case. In terms of charge transport, this shallow energy feature should not significantly impede or enhance carrier flow. Several pertinent characteristics of the CdTe(100) c(2 $\times$ 2) unrelaxed surface are changed by the applied relaxation to its surface. It is clear that relaxation of the CdTe(100) plane oriented surfaces has a strong effect on the band alignment features present at the surface.

In accordance with surface polarity, CdTe(100) plane orientations can be classified as macroscopically non-polar surfaces if demi-steps (A to B facet steps) are considered [95]. However, the current atomistic modeling on CdTe(100) surfaces will have some type of charging effect present that causes the bands to bend as a polar surface. Only the c(2 $\times$ 2) reconstruction after relaxation was able to have flatter bands with minimal surface electronic states as it satisfies the ECR. It is therefore evident that a relaxed reconstructed c(2 $\times$ 2) CdTe(100) surface provides the most favorable conditions out of the CdTe(100) cases studied for hole carrier transport in CdTe PV devices.

As shown in Figure 3.9, two different CdTe(111) surfaces were investigated for comparison to each other as well to the CdTe(100) plane orientations. Figure 3.9a and Figure 3.9b depict the energy band alignment features present for the unrelaxed and relaxed cases, respectively, for the (1 $\times$ 1) CdTe(111) surface. Figure 3.9c and Figure 3.9d represent the unrelaxed and relaxed

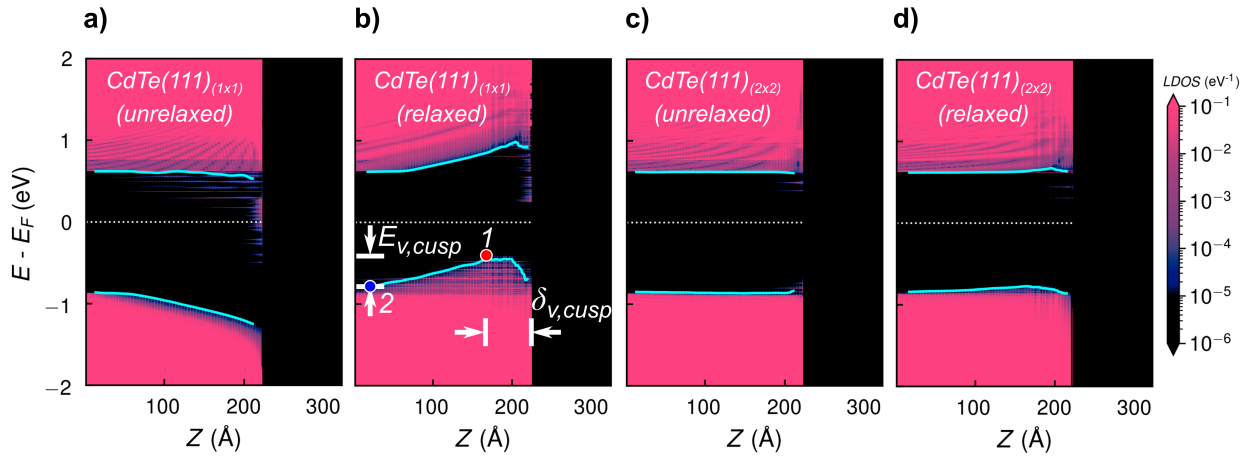

Figure 3.9: Localized density of states mapping across the unreconstructed and reconstructed CdTe(111) one-probe models separated as unrelaxed (a,b) and relaxed cases (c,d). Plane orientation and reconstruction type are provided in each image above. The zero energy on the y-axis is referenced by the Fermi level E_F of each respective band alignment profile. The light blue curves are the macroscopically averaged curve fits of the valence band maximum and conduction band minimum, respectively. Points 1 and 2 in (b) are used to determined the cusp energy potential $E_{v,cusp}$ with details provided in Section 3.3.

cases, respectively, for the (2 $\times$ 2) CdTe(111) surface reconstruction. All electronic properties obtained from the band profiles of each CdTe(111) one-probe model are quantified in Table 3.2 and Table 3.3. An investigation of the CdTe(111) surfaces provides direct insights on how plane orientation affects energy band alignment properties from a spatial representation across the surface domain.

Band alignment for the unrelaxed CdTe(111) (1 $\times$ 1) surface is presented in Figure 3.9a. As in the CdTe(100) case, the CdTe(111) surface displays a downward valence band bending of -0.38 eV with several shallow surface states that extend far into the surface region ($\sim$ 10 nm). The conduction band remains relatively flat as the surface states are discretely spaced out across the energy band gap of the rightmost part of the surface region. As in the CdTe(100) configuration, the surface electronic states could potentially increase carrier recombination as seen with E_{def1} (+0.23 eV) and E_{def2} (-0.40) surface states levels with 10^{-1} eV^{-1} DOS magnitudes. After relaxing the CdTe(111) unreconstructed surface, the surface states shift further above E_F with an order of magnitude smaller DOS value. Yet, the most intrigue detail of energy band alignment along the respective facet was discovered. The relaxed CdTe(111) (1 $\times$ 1) case in Figure 3.9b no longer has a

large downward valence bend but instead has developed a large cusp energy potential $E_{v,cusp}$ with a height of 0.33 eV. The resulting cusp feature has been recognized within CdTe PV devices such as the CdTe/Te interface by means of a photoelectron spectroscopy characterization study performed by *Fritsche et al.* [34]. The study demonstrates a hole enhancing feature that resides near the CdTe/Te interface to facilitate hole transport toward the back of the PV device. Furthermore, a similar cusp energy potential height was obtained for the computational study of CdTe(111)/Te [81] that only occurs after relaxation of the CdTe(111) surface. It must be stated the experimental study by *Fritsche et al.* was done for polycrystalline CdTe while the results in the current work are for a pristine (111) oriented CdTe single crystal surface. Nonetheless, it is suggested that the geometry optimized, unreconstructed CdTe(111) surface can provide an additional mechanism for hole transport that is not seen in the CdTe(100) cases.

Looking at the CdTe(111) reconstructed case in Figure 3.9c, the CdTe(111) (2 $\times$ 2) surface has a negligible valence band bending effect ($E_{v,surf}$ = +0.01 eV) than its unreconstructed counterpart. Furthermore, the surface states levels have decreased appreciably with the highest concentration of surface states being nearly -0.80 eV below E_F. The unrelaxed CdTe(111) (2 $\times$ 2) surface shows distinct differences in band bending and surface states from the (1 $\times$ 1) unreconstructed case that establishes the role of Cd surface vacancies for polarized CdTe facets. After GO is achieved on the CdTe(111) (2 $\times$ 2) surface as shown in Figure 3.9d, an energy potential cusp develops with a magnitude $E_{v,cusp}$ = +0.07 eV above the valence band of the bulk CdTe region. The cusp energy potential occurs $\delta_{v,cusp}$ = 63.746 Å from the Cd-termination layer of the CdTe(111) (2 $\times$ 2) one-probe model, which is similar to the CdTe(111) (1 $\times$ 1) cusp location at 59.017 Å. The $\delta_{v,cusp}$ value is within the region length that has been structurally relaxed (GO $\sim$ 5-6 nm) in the CdTe(111) surface. Therefore, the spatial position of the cusp energy potential $E_{v,cusp}$ for both the relaxed cases of the unreconstructed and reconstructed CdTe(111) one-probe models correlates with the GO size used to minimize the atomic forces. Similar to the CdTe(100) c(2 $\times$ 2) case, the (2 $\times$ 2) surface reconstruction also mitigates the CdTe surface recombination limiting factor brought upon by surface elecronic states since the CdTe(111) (2 $\times$ 2) surface obeys the ECR as described in the

previous subsection. It is clear that the CdTe(111) (2 $\times$ 2) surface decreases the electronic states that were present in the (1 $\times$ 1) relaxed case and still develops a small energy cusp.

The energy cusp in both the CdTe(111) (1 $\times$ 1) and (2 $\times$ 2) cases provides a new insight in band alignment that is strictly dependent on the plane orientation and the amount of relaxation present in the CdTe surface. Although a small energy cusp was seen for the CdTe(100) c(2 $\times$ 2) case, the cusp seen specifically for the CdTe(111) (1 $\times$ 1) case has a greater magnitude and thus would lead to better majority charge carrier (holes) transport at the back of a CdTe device. Two possibilities to create the same cusp potentials seen in either Figure 3.9c or Figure 3.9d for improved hole current transport in a CdTe(111) absorber layer are proposed as follows: 1) develop a CdTe deposition process that relaxes the CdTe(111) (1 $\times$ 1) or (2 $\times$ 2) surface less than 5 nm from the termination layer; 2) fabricate a CdTe(111) facet that relaxes 5 nm within the surface but undergoes some type of etching process that extends past the downward valence band bend while retaining $E_{v,cusp} > E_{V,CdTe}$. The energy cusp readily seen in (111) but minimized in (100) CdTe surfaces reveals the importance of plane orientation and surface relaxation as some of the possible mechanisms leading to improved CdTe PV device performance.

Research Impact

The DFT+GF approach to investigating the electronic features of the CdTe surface gives a detailed picture of atomic-scale electronic behaviors that cannot be studied from surface theory and classical band alignment models alone. Atomistic modeling of CdTe(100) and CdTe(111) oriented facets reveals the importance of plane orientation, surface reconstruction, and surface relaxation to the determination of electronic behaviors in CdTe surfaces.

There is a complex relationship between electronic performance of CdTe to its plane orientation. Both the (100) and (111) CdTe surfaces lead to a unique description of the band bending profile that adds to the conventional understanding of CdTe surface polarity. In general, the Cd-termination layer bends downward with surface polarity determining the amount of bending as suggested in surface theory [99]. Geometric optimization leads to key insights on how relaxed CdTe surfaces distribute charge densities that introduce vastly different energy band profiles than

the unrelaxed cases. For most of the CdTe relaxed variants, the surface electronic states are reduced by the minimization of atomic forces that may mitigate recombination losses at the CdTe surface.

The investigation of unreconstructed vs. reconstructed CdTe surfaces within their respective plane orientations provide strong conclusions. In general, the reconstructed surfaces give the most favorable structural and electronic characteristics that lead to cleaner CdTe energy band alignments. Both the CdTe(100) c(2 $\times$ 2) and CdTe(111) (2 $\times$ 2) reconstructed surfaces obey the ECR that leads to charge compensated surfaces and thus virtually no surface electronic states. The superiority of reconstructed CdTe surfaces indicates how the surface point defects considered in the study are beneficial along their respective plane orientations.

The most prominent feature seen exclusively for the relaxed CdTe(111) surfaces is the favorable energy cusp that forms within the surface band profile. The resulting cusp feature has been recognized at the CdTe/Te interface (albeit a polycrystalline CdTe layer) with a photoelectron spectroscopy characterization study performed by *Fritsche et al.* [34]. Furthermore, the computational study on the CdTe(111)/Te interface shown later in Chapter 4 indicates a similar cusp feature existing within the unreconstructed CdTe(111) region [81]. If the cusp feature along the CdTe(111) plane orientation could be retained throughout the CdTe fabrication process, it may provide an additional mechanism for improving hole carrier transport in CdTe PV devices.

The detailed aspects revealed in the DFT+GF modeling approach of CdTe(100) and (111) facets give a fundamental overview of electronic features in CdTe surfaces. Energy band alignment from an atomistic computational standpoint enables the understanding of CdTe surfaces without the reliance on pre-determined band alignment properties required in theoretical models such as the Anderson Rule [30]. In turn, the spatial characteristics obtained from the DFT+GF CdTe surface models can later be verified by surface and near-interface characterization techniques such as photoelectron spectroscopy and time-resolved photoluminescence. The atomistic perspectives of CdTe surfaces provide further guidance for deposition processes to be modified so as to achieve optimal CdTe surface properties used in CdTe-based thin film PV applications.

3.3.2 Te-Terminated Surfaces

Research Scope

The evaluation of Te-terminated CdTe surfaces closely follows the approach from the Cd-terminated study in Section 3.3.1 to gain a wide perspective of possible surface formations and their effects on energy band alignment. Although it has been suggested that the Te-terminated surface is best suited for epitaxial growth applications [96], there is no clear indication that the Te termination layer will induce favorable electronic features for CdTe PV devices. Thus, an investigation is made on various unreconstructed and reconstructed Te-terminated CdTe surfaces for the CdTe($\bar{1}00$) and CdTe($\bar{1}\bar{1}\bar{1}$) facets. Varied conditions for the Te-terminated surfaces were investigated to determine whether the filled dangling bonds of Te caused more issues than the empty dangling bonds of the Cd-terminated CdTe surfaces. Along with the (1×1) cases, the c(2×2) CdTe($\bar{1}00$) and (2×2) CdTe($\bar{1}\bar{1}\bar{1}$) surface reconstructions were also simulated with the latter being seen experimentally in other studies [107]. It must be noted that the most stable Te-rich CdTe{100} (2×1) and (3×1) facets [104, 108] were not included in the study. However, the current research problem focuses on distinguishing the effects of a Te-termination layer compared to the Cd-termination layer for similar hypothetical reconstructions. Spatially-dependent energy band alignments are obtained from the DFT+GF method for each Te-terminated CdTe surface and are used for discussing the possible implications they have on CdTe PV device performance.

Relaxation Effects

Figure 3.10 shows the atomic arrangements for each of the unreconstructed and reconstructed Te-terminated CdTe($\bar{1}00$) surfaces, respectively. Previously in the Cd-terminated simulations, the two surfaces had remarkably different surface structures as the reconstructed case flattened out, allowing the surface atoms to be positioned in a way where they obeyed the ECR. It was not known if the CdTe($\bar{1}00$) cases would mimic a similar behavior, which was why both were investigated together.

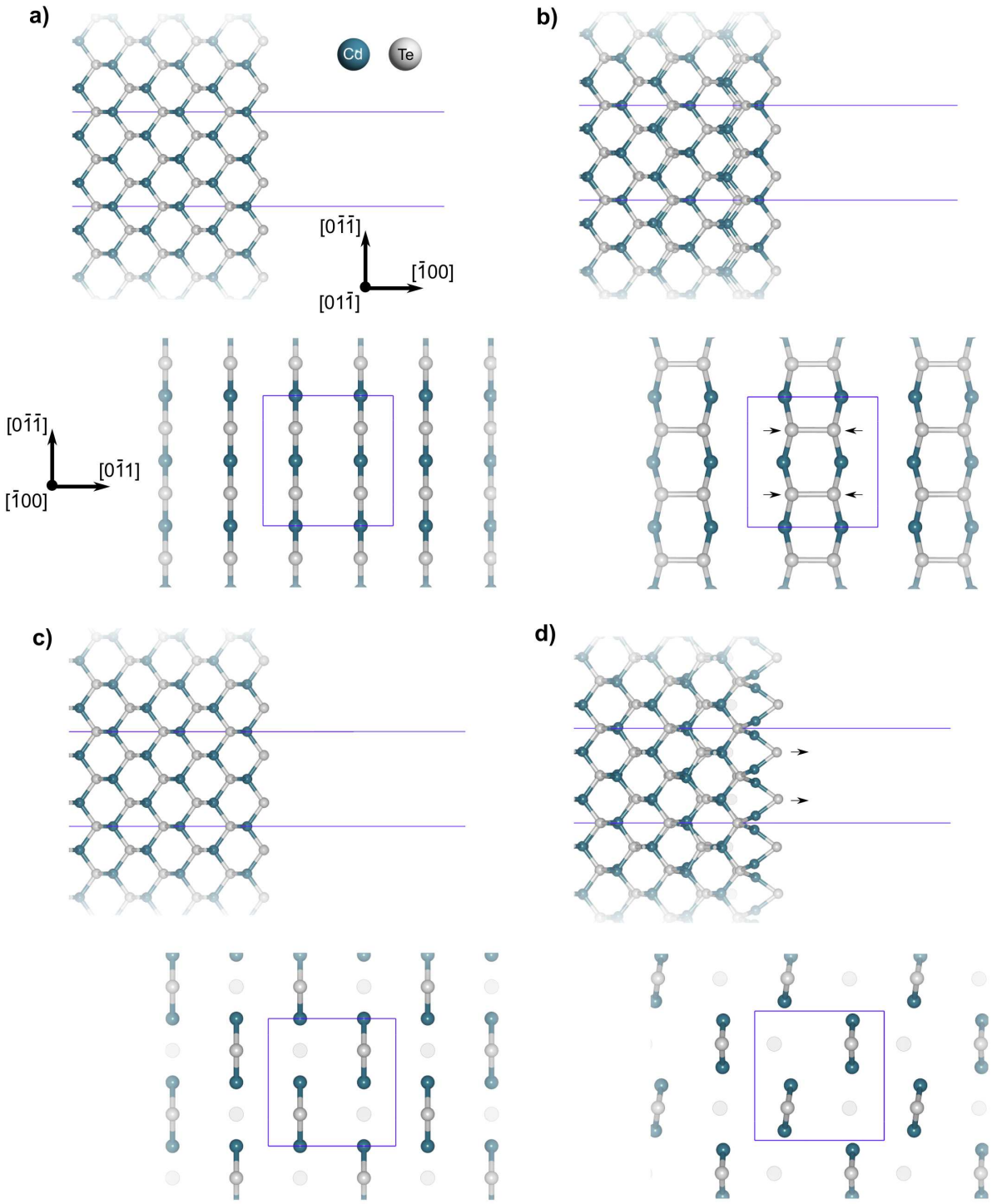

Figure 3.10: Perspective views of the respective unrelaxed and relaxed atomic configurations of (a,b) the (1 $\times$ 1) unreconstructed and (c,d) the c(2 $\times$ 2) reconstructed CdTe($\bar{1}$00) surfaces. Two views are shown along the transport direction (top subfigure) and perpendicular directions (bottom subfigure) of the one-probe models. The perpendicular view only shows the last two atomic layers in the surface domain for clarity. All surfaces are visualized using the indices provided in (a). The "ghost" atoms are shown as translucent circles in (c,d).

Prior to GO, the CdTe($\bar{1}00$) (1×1) case contains alternating Te and Cd layers that are doubly bonded to each other per atom. From the cross-sectional view, a line of Te and Cd atoms can be seen between the first two immediate layers of the CdTe surface. After relaxation, the CdTe($\bar{1}00$) (1×1) surface has its Te atoms shifted in a manner that leads to anion dimerization. In response, the surface slightly expands by 0.489 Å in the [$\bar{1}00$] direction. The newly formed CdTe($\bar{1}00$) surface closely resembles the Te-terminated (2×1) CdTe reconstruction [46, 104], which is stable after the formation of the Te-Te single bond along the surface [109]. Thus, CdTe($\bar{1}00$) (1×1) appears to have transitioned to a (2×1)-like reconstruction after relaxation and may explain why in its unreconstructed form the CdTe($\bar{1}00$) surface without relaxation can be considered an unstable surface. Dimerized surfaces have been mentioned as one of the mechanisms leading to a charge neutral surface and thus satisfying the ECR [92], but typically accompanied by a reconstructed CdTe{100} surface. If the dimerization effect were to form on the CdTe($\bar{1}00$) surface as predicted with the current simulation setup, then that would suggest the surface to be well-behaved for energy band alignment with less band bending at the surface.

For the CdTe($\bar{1}00$) c(2×2) facet, there was a significant shift outward by 1.292 Å from the remaining two Te atoms in the topmost layer of the supercell. The cross-sectional view shows that there is a small rotational tilt in the bonding arrangement of the two immediate layers. Both effects are quite different than what was seen along the CdTe(100) c(2×2) case where the reconstructed surface relaxed to a flat, planar formation after creating two Cd vacancies on it. The energy band alignment presented in the next subsection will prove if the relaxation on the CdTe($\bar{1}00$) c(2×2) surface introduces any harmful features to it.

Evaluation of the geometry optimized CdTe($\bar{1}\bar{1}\bar{1}$) cases as shown in Figure 3.11 were done to elucidate patterns between Te and Cd termination layers for surface structural characteristics. Relaxation of the CdTe($\bar{1}\bar{1}\bar{1}$) surface causes the termination layer to slightly expand with the Te atoms nonuniformly displacing in the [$\bar{1}\bar{1}\bar{1}$] direction. Along the cross-sectional view perpendicular to the surface, there is little indication of atomic rearrangement present in comparison to that

seen with the CdTe(111) unreconstructed surface. Thus, the CdTe($\bar{1}\bar{1}\bar{1}$) surface tends to retain its unreconstructed periodicity after relaxing to its force-minimized position.

The relaxed CdTe($\bar{1}\bar{1}\bar{1}$) (2×2) reconstruction undergoes a radial expansion due to the single Te vacancy. The surrounding Cd atoms radially move outward by 0.654 Å within the ($\bar{1}\bar{1}\bar{1}$) plane while the nearest neighboring Te atoms are slightly displaced as well. The phenomenon is closely representative of the CdTe(111) (2×2) surface, clearly showing the effect of relaxation due to a surface point defect like the Te vacancy. In the [$\bar{1}\bar{1}\bar{1}$] direction, the topmost Te layer expands by 0.922 Å with the second Cd layer expanding by 0.613 Å.

The relaxation of the CdTe($\bar{1}\bar{1}\bar{1}$) cases again show the optimized surface arrangement that a Te-terminated surface finds favorable for charge redistribution. The alteration of the reconstructed surface by GO due to the removal of one Te atom as seen in experimental studies [107] will influence the atomic displacements that later cause the energy band alignments to change nearest the surface.

Energy Band Alignment

Figure 3.12 and Figure 3.13 provide all the calculated band alignments for each of the Te-terminated CdTe facets under investigation. In general, both the CdTe($\bar{1}00$) and CdTe($\bar{1}\bar{1}\bar{1}$) plane orientations have a smaller bulk CdTe band gap $E_{g,CdTe}$ than the CdTe(100) and CdTe(111) planes for the Cd-terminated cases. This may be attributed to the amount of band bending present in the Te-terminated simulations and thus longer screening regions that require larger surface domain sizes to properly accommodate them. The following paragraphs will describe each of the studied Te-terminated CdTe surface cases in more detail.

In Figure 3.12a, the CdTe($\bar{1}00$) (1×1) surface prior to GO shows a dramatic upward bend in both the VBM and CBM. The bending direction is opposite of the Cd-terminated CdTe(100) surface (Figure 3.8) and is correctly attributed to the surface charging that occurs from the cation/anion-terminated surface as suggested by surface theory (see Section 3.1.2). Along the CdTe($\bar{1}00$) facet, the surface electronic states extend from the VBM at the surface past the Fermi level E_F. If the surface states were to gradually extend from the surface VBM rather than be separated in discrete

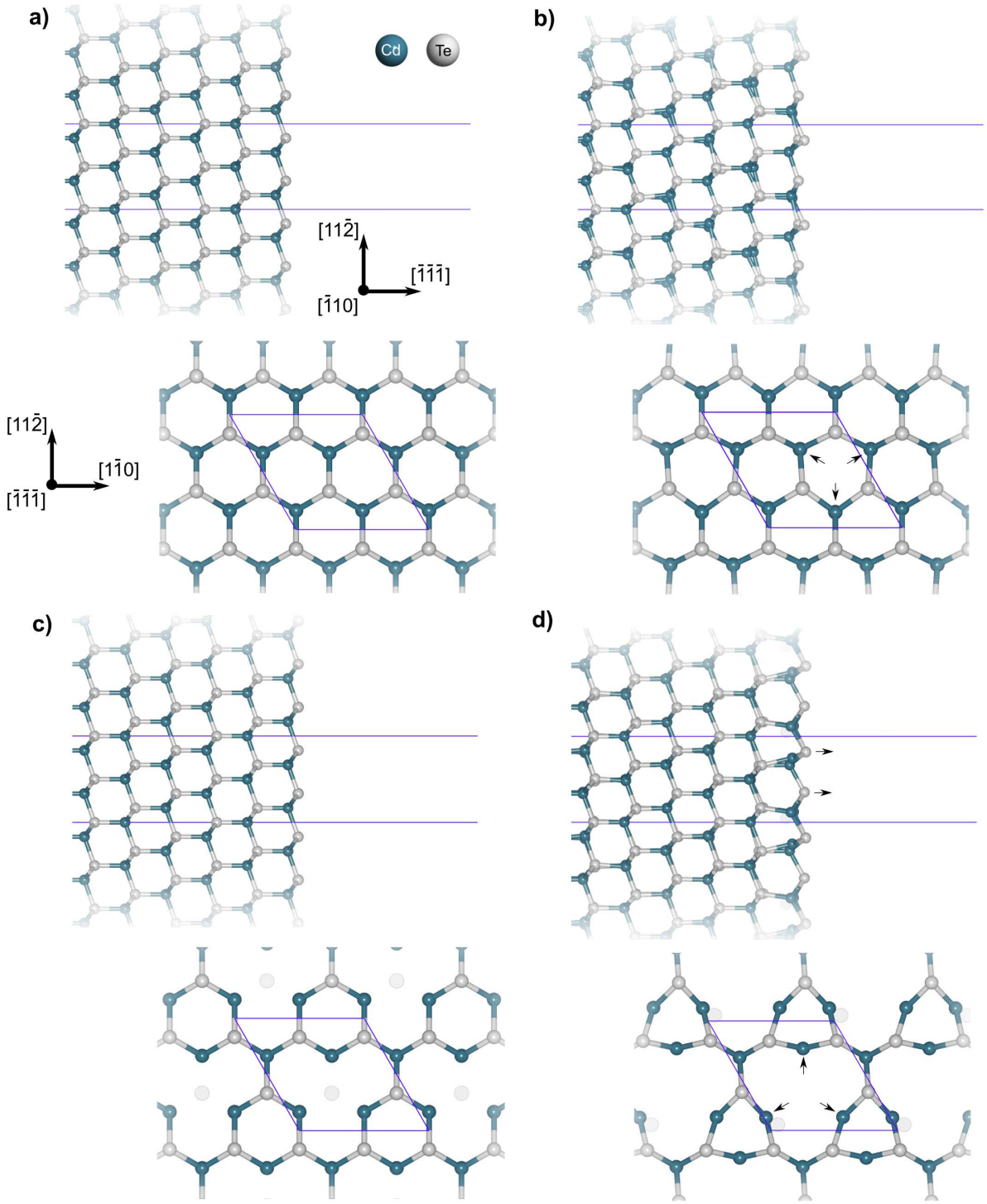

Figure 3.11: Perspective views of the respective unrelaxed and relaxed atomic configurations of (a,b) the (1 $\times$ 1) unreconstructed and (c,d) the (2 $\times$ 2) reconstructed CdTe($\bar{1}\bar{1}\bar{1}$) surfaces. Two views are shown along the transport direction (top subfigure) and perpendicular directions (bottom subfigure) of the one-probe models. The perpendicular view only shows the last two atomic layers in the surface domain for clarity. All surfaces are visualized using the indices provided in (a). The "ghost" atoms are shown as translucent circles in (c,d).

levels, the available states for charge carrier transport could be beneficial at back of the CdTe absorber layer. Real surfaces have some type of relaxation during deposition, so the features shown in Figure 3.12 are idealistic to say the least. That is why the CdTe($\bar{1}$00) (1 $\times$ 1) surface also has results after relaxation (Figure 3.12b). The relaxed surface contains little surface electronic states that exist closer to the CB. An extremely small energy cusp of +0.04 eV appears in the VB while the CB remains flat. Interestingly, the dimerization seen in the previous subsection for the CdTe($\bar{1}$00) (1 $\times$ 1) model has led to the Te dangling bonds on the CdTe($\bar{1}$00) plane to be neutralized. The explanation has been proposed for III-V semiconductor compounds terminated along the {100} facets [92], but only after the same number of cation vacancies as surface dangling bonds (i.e. the c(2 $\times$ 2) reconstruction) has been created. Although the energy band alignment of the CdTe($\bar{1}$00) facet appears to be well-behaved, the instability of the surface along with the fact that the unreconstructed surface does not satisfy the ECR deem the CdTe($\bar{1}$00) (1 $\times$ 1) case to be unlikely to form.

The CdTe($\bar{1}$00) c(2 $\times$ 2) surface is reported in Figure 3.12c and Figure 3.12d. It must be noted beforehand that the Gaussian width used for the relaxed CdTe($\bar{1}$00) c(2 $\times$ 2) case in Figure 3.12d was set at 15 Å to avoid the missing data slice artifact that when included gives an erroneous $E_{v,surf}$ magnitude. After creating the c(2 $\times$ 2) reconstructed surface along the CdTe($\bar{1}$00) plane, the band alignment becomes flatter than its unreconstructed counterpart. Yet, there are a two prominent surface state levels, one above and the other below the Fermi level E_F. The surface states below E_F have a DOS magnitude of 10^{-1} eV^{-1} and do reside closer to the VBM nearest the surface. Relaxation of the CdTe($\bar{1}$00) c(2 $\times$ 2) surface (Figure 3.12d) causes the VBM to no longer display a slight downward slope but instead has leveled out toward the bulk region. A negligible energy cusp potential of +0.01 eV also develops and is not expected to affect charge transport along the bands. Most importantly, the surface states have significantly decreased due to the surface relaxation. The detected surface states are mostly located above the Fermi level and have a DOS of 10^{-1} to 10^{-4} eV^{-1}. A similar change to the electronic features was seen for the Cd-terminated case, which

shows that the relaxation and reconstruction effects are necessary for improved electronic features of CdTe($\bar{1}$00) surfaces.

Table 3.4: Salient electronic features within each ($\bar{1}$00) and ($\bar{1}\bar{1}\bar{1}$) CdTe one-probe model. $\delta_{v,cusp}$ indicates the position where the cusp energy potential $E_{v,cusp}$ is determined starting from the termination layer. All energy band alignment values are determined from the macroscopically averaged curve fit of each local density of states plot. Any +/- values indicate energy values referenced to the Fermi level E_F (marked as 0 eV).

Type	Facet	$E_{g,CdTe}$ (eV)	$E_{c,surf}$ (eV)	$E_{v,surf}$ (eV)	$\delta_{v,cusp}$ (Å)	$E_{v,cusp}$ (eV)
Unrelaxed	CdTe($\bar{1}$00)$_{(1\times1)}$	1.43	+0.35	+0.59	n/a	n/a
	CdTe($\bar{1}$00)$_{c(2\times2)}$	1.47	-0.02	-0.09	n/a	n/a
	CdTe($\bar{1}\bar{1}\bar{1}$)$_{(1\times1)}$	1.42	+0.39	+0.68	n/a	n/a
	CdTe($\bar{1}\bar{1}\bar{1}$)$_{(2\times2)}$	1.44	+0.14	+0.26	n/a	n/a
Relaxed	CdTe($\bar{1}$00)$_{(1\times1)}$	1.47	0.00	-0.03	133.650	+0.04
	CdTe($\bar{1}$00)$_{c(2\times2)}$	1.46	0.00	-0.03	99.630	+0.01
	CdTe($\bar{1}\bar{1}\bar{1}$)$_{(1\times1)}$	1.39	+0.44	+0.74	n/a	n/a
	CdTe($\bar{1}\bar{1}\bar{1}$)$_{(2\times2)}$	1.46	+0.07	+0.15	188.511	-0.04

Figure 3.13 provides the CdTe($\bar{1}\bar{1}\bar{1}$) unreconstructed and reconstructed energy band alignments. For the CdTe($\bar{1}\bar{1}\bar{1}$) unreconstructed case in Figure 3.13a, the band bending upward is clear indication that the surface is charging negatively from the Te termination layer as seen for the CdTe($\bar{1}$00) case (see Figure 3.12a). The surface VB and CB heights are $E_{v,surf}$ = +0.68 eV and $E_{c,surf}$ = +0.39 eV, respectively, meaning that there is a strong negative charging effect on the surface. The CdTe($\bar{1}\bar{1}\bar{1}$) (1 $\times$ 1) surface also contains a number of electronic states that extend past the Fermi level toward the CB in a discretized manner. There is little change to the overall band alignment features after GO is applied to the CdTe($\bar{1}\bar{1}\bar{1}$) (1 $\times$ 1) facet (Figure 3.13b). The magnitudes of the surface VB and CB heights have slightly changed to $E_{v,surf}$ = +0.74 eV and $E_{c,surf}$ = +0.44 eV, respectively. The negative charging at the surface means that charge neutrality has not been achieved for the surface and thus the CdTe($\bar{1}\bar{1}\bar{1}$) (1 $\times$ 1) unreconstructed case does not obey the ECR. The minimal relaxation effects demonstrated in Figure 3.11b explain why there is little energy band alignment changes in the CdTe($\bar{1}\bar{1}\bar{1}$) (1 $\times$ 1) case. Despite the perceived benefits of

Table 3.5: Surface electronic state energy levels and DOS magnitudes within each ($\bar{1}00$) and ($\bar{1}\bar{1}\bar{1}$) CdTe one-probe model. All electronic state energy values for a given facet are chosen according to highest DOS magnitude and are accurate to within $\pm$5 meV.

Type	Facet	E_{def1} (eV)	$D(E_{def1})$ (eV^{-1})	E_{def2} (eV)	$D(E_{def2})$ (eV^{-1})
Unrelaxed	CdTe($\bar{1}00$)$_{(1\times1)}$	-0.01	7.91×10^{-1}	+0.08	1.09×10^{-1}
	CdTe($\bar{1}00$)$_{c(2\times2)}$	-0.60	5.77×10^{-1}	-0.55	1.39×10^{-1}
	CdTe($\bar{1}\bar{1}\bar{1}$)$_{(1\times1)}$	+0.21	3.90×10^{-2}	+0.10	2.55×10^{-2}
	CdTe($\bar{1}\bar{1}\bar{1}$)$_{(2\times2)}$	+0.43	$2.94 \times 10^{+2}$	+0.74	5.64×10^{-2}
Relaxed	CdTe($\bar{1}00$)$_{(1\times1)}$	+0.52	2.59×10^{-2}	+0.45	7.80×10^{-3}
	CdTe($\bar{1}00$)$_{c(2\times2)}$	+0.47	1.35×10^{-1}	+0.55	1.83×10^{-4}
	CdTe($\bar{1}\bar{1}\bar{1}$)$_{(1\times1)}$	+0.33	1.92×10^{-2}	+0.20	6.17×10^{-3}
	CdTe($\bar{1}\bar{1}\bar{1}$)$_{(2\times2)}$	+0.57	1.48×10^{0}	-0.71	4.49×10^{-3}

charge neutral surfaces, the upward bend present in the unreconstructed CdTe($\bar{1}\bar{1}\bar{1}$) surface would be advantageous for hole charge transport in the back of the CdTe PV device. The resulting band alignment feature may possibly suggest that the Te-terminated surface provides a favorable field effect mechanism for CdTe surfaces.

As expected, the CdTe($\bar{1}\bar{1}\bar{1}$) (2 $\times$ 2) case leads to a different band alignment than the unreconstructed version. Figure 3.13c reveals the unrelaxed reconstructed CdTe surface containing shallower band bending and several electronic surface states. The states measured near the Te-termination layer as shown in Table 3.5 sit +0.43 and 0.74 eV above the Fermi level E_F with the first state level having a DOS magnitude of 2.94×10^2 eV^{-1}. The surface states appear to be the main culprit for the banding bending effect and are assumed to be unfavorable as they are discretely placed at the surface and will thus increase surface recombination. Once the CdTe($\bar{1}\bar{1}\bar{1}$) (2 $\times$ 2) surface energy band alignment experiences relaxation as represented in Figure 3.13d, the VB and CB bands flatten out as seen in many previous cases. Although there are still small magnitudes for the VBM and CBM traces at the surface ($E_{v,surf}$ = +0.15 eV and $E_{c,surf}$ = +0.07 eV from Table 3.4), the previous surface states have noticeably decreased as a benefit for charge transport across the surface. The radial expansion of the Cd atoms due to the Te vacancy as seen in Figure 3.11d results in the cleaner band alignment features. In relation to the Cd-terminated CdTe(111) (2 $\times$ 2) surface

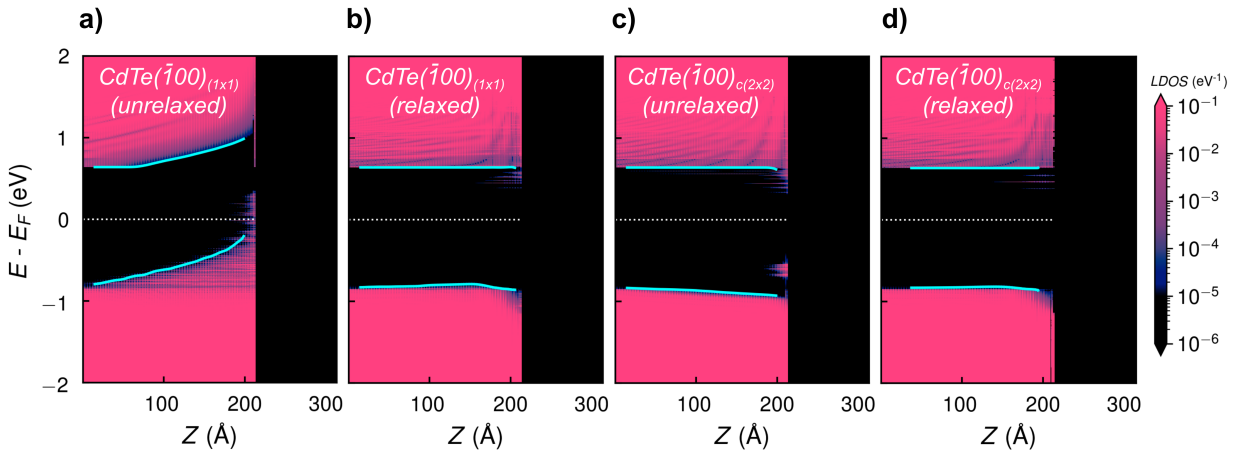

Figure 3.12: Localized density of states mapping across the unreconstructed and reconstructed CdTe($\bar{1}$00) one-probe models separated as unrelaxed (a,b) and relaxed cases (c,d). Plane orientation and reconstruction type are provided in each image above. The zero energy on the y-axis is referenced by the Fermi level E_F of each respective band alignment profile. The light blue curves are the macroscopically averaged curve fits of the valence band maximum and conduction band minimum, respectively.

though, the Te-terminated version does still have some surface band bending, indicative of some charging effect. It cannot be concluded that the CdTe($\bar{1}\bar{1}\bar{1}$) (2 $\times$ 2) case is charge neutral from the energy band alignment plot alone and requires further investigation.

Research Impact

The relaxation and reconstruction effects on the non-stoichiometric Te-terminated CdTe($\bar{1}$00) and CdTe($\bar{1}\bar{1}\bar{1}$) facets both develop more favorable energy band alignment characteristics that mitigate surface recombination. If the electronic features seen in all the localized density of states plots were present at the back of the CdTe absorber layer, then it would suggest that Te-terminated surfaces could encourage majority hole carrier transport. If the features were retained toward the front of CdTe, then the holes would not be impeded to move toward the front while the electron charge carriers would be hindered by the upward CB bending, resulting in a severly compromised CdTe PV device. Clearly, the way that the surface terminates during CdTe epitaxial growth will undoubtedly influence how charge transport behaves in the CdTe PV device.

Amongst the CdTe($\bar{1}$00) simulation models, the relaxed CdTe($\bar{1}$00) (1 $\times$ 1) and c(2 $\times$ 2) reconstructions had the cleanest surface properties. Real-world deposition processes will have some

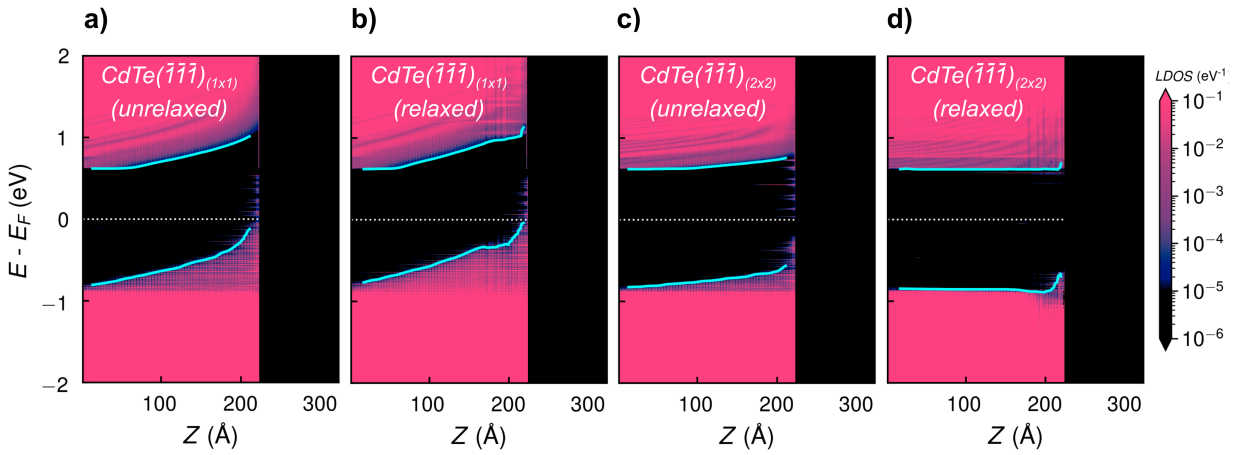

Figure 3.13: Localized density of states mapping across the unreconstructed and reconstructed CdTe($\bar{1}\bar{1}\bar{1}$) one-probe models separated as unrelaxed (a,b) and relaxed cases (c,d). Plane orientation and reconstruction type are provided in each image above. The zero energy on the y-axis is referenced by the Fermi level E_F of each respective band alignment profile. The light blue curves are the macroscopically averaged curve fits of the valence band maximum and conduction band minimum, respectively.

type of relaxation on the surface to minimize the energy and forces present on it. If the features in the two cases could be maintained, then incorporating a controlled deposition method that could create two Te vacancies on the surface prior to creating an interface between CdTe and a back contact layer would be beneficial for CdTe device performance. Several past studies have stated that the (2 $\times$ 1) Te surface is the stablized reconstruction [104, 108], which may certainly give different results than the two Te-terminated CdTe($\bar{1}$00) surfaces under review. Yet, in direct comparison to the Cd-terminated CdTe(100) cases, both studies make it evident that the c(2 $\times$ 2) reconstruction is the most beneficial and stable facet for either doubly bonded termination layer.

A complex perspective is developed for the CdTe($\bar{1}\bar{1}\bar{1}$) unreconstructed and reconstructed surfaces. The unrelaxed facets always bend upward, which follows closely with surface theory of negatively charged surfaces. However, relaxation of the unreconstructed case does not flatten out the bands, suggesting some charging effect remains for that surface. If the CdTe($\bar{1}\bar{1}\bar{1}$) (1 $\times$ 1) surface were to be created for the CdTe PV fabrication process, then there would need to be some way to passivate the surface so as to eliminate the detrimental surface states. As for the CdTe($\bar{1}\bar{1}\bar{1}$) (2 $\times$ 2) reconstruction, no passivation is needed as the surface already satisfies the ECR according to other studies [107]. One previous study has stated that the CdTe($\bar{1}\bar{1}\bar{1}$) surface

is the preferable choice for CdTe epitaxial growth [96], which would correlate well with the case for the energy band alignment results at the back of CdTe absorber layer. However, other studies have determined CdTe($\bar{1}\bar{1}\bar{1}$) surfaces to be highly disordered prior to annealing in comparison to the Cd-terminated CdTe(111) surfaces [106]. There is a complex relationship with how annealing can affect the surface characteristics of CdTe($\bar{1}\bar{1}\bar{1}$) that are beyond the scope of the research work. Regarding bulk DFT studies, growing CdTe under Te-rich conditions actually limits the minority-carrier lifetimes due to recombination centers such as the Te antisite and Te interstitial [40]. As for intrinsic CdTe surfaces, high surface recombinations on Te-rich CdTe single crystal and polycrystalline surfaces [102] also hinder CdTe PV device performance. Therefore, upward band bending along the Te-terminated CdTe($\bar{1}\bar{1}\bar{1}$) facets will certainly not solve all the problems associated with charge transport. That is why the relaxation effects leading to flattened bands and (2×2) surface reconstruction eliminating some of the surface states could be possible pathways that allow CdTe($\bar{1}\bar{1}\bar{1}$) surfaces to be beneficial to CdTe PV devices.

3.3.3 Cl_{Te} Formation on CdTe($\bar{1}\bar{1}\bar{1}$) Surface

Research Scope

Noteworthy advances in solar cell efficiency for CdTe-based photovoltaic devices is mainly attributed to the well-known cadmium chloride ($CdCl_2$) passivation treatment. The passivating effect of $CdCl_2$ involves the substitution of Cl into areas that contain high densities of defects such as CdTe grain boundaries, enabling inversion from the p-type CdTe interior to a n-type grain boundary region [110]. Point defects that most likely exist within CdTe bulk [41] may also create several complex pairs that involve Cl [43], but only one case will be considered in the study. Two chlorine-related formations on the CdTe($\bar{1}\bar{1}\bar{1}$) surface were evaluated in the study: 1) Cl passivating a Te site (denoted as Cl_{Te}), and 2) Cl_{Te} acting as the nearest neighbor to a Cd vacancy along the surface (hereafter written as Cl_{Te}-V_{Cd}). Both complexes have been determined to be most energetically stable in the chlorine-doped CdTe bulk under Te-rich growth conditions [44] but have not been studied along various plane orientations of Te-terminated CdTe surfaces. For

each Cl-related CdTe($\bar{1}\bar{1}\bar{1}$) surface model, the surface Cl concentration was varied after passivating the Te-terminated CdTe($\bar{1}\bar{1}\bar{1}$) (1 × 1) facets. The highly polar CdTe($\bar{1}\bar{1}\bar{1}$) surface was expected to significantly change with the formation of Cl_{Te} along the cleaved surface.

Relaxation Effects

Analysis of the Cl_{Te} formation on the CdTe($\bar{1}\bar{1}\bar{1}$) surface was done for three different variations of the surface: 1) 25% Cl_{Te}, 2) 25% Cl_{Te} with a Cd vacancy (V_{Cd}), and 3) 50% Cl_{Te}. The placements of the Cl and geometry optimized configurations are shown in Figure 3.14. Only the relaxed variants were provided as the effects of GO have been clearly established in Section 3.3.1 and Section 3.3.2. For the 25% Cl_{Te} simulation (Figure 3.14a), there were hardly any atomic distortions seen after GO. An outward displacement of the Cd atoms nearest the Cl_{Te} defect results in a Cd-Cl bond length of 2.64 Å. The structural behavior after GO for the 25% Cl_{Te} model follows closely with what is seen from other literature [44].

After the inclusion of V_{Cd} along with 25% Cl_{Te} to create a Cl-related complex pair at the CdTe($\bar{1}\bar{1}\bar{1}$) surface (Figure 3.14b), a strong distortion to the surface symmetry is evident. The last two layers of the model also flatten out. The Te atoms tend to move closer to the Cd vacancy by 0.395 Å from their unrelaxed atomic positions but do not form Te-dimers as suggested in other work [44].

The final relaxed simulation, which includes 50% Cl_{Te} as shown in Figure 3.14c, results in the Cl atoms moving far enough that the bond formation is not present between the Cd atoms surrounding it. There is little movement of the surface in the [$\bar{1}\bar{1}\bar{1}$] direction, showing that the surface relaxation effect is benign for the 50% Cl_{Te} case.

Energy Band Alignment

The energy band alignments provided in Figure 3.15 give a unique outlook on the effect of Cl_{Te} at the CdTe($\bar{1}\bar{1}\bar{1}$) surface. Starting with the 25% Cl_{Te} concentration in Figure 3.15a, the VBM and CBM curves bend upward accordingly as they are still charging negatively. The surface band heights are $E_{v,surf}$ = +0.63 eV and $E_{c,surf}$ = +0.37 eV, respectively. A cusp energy potential develops

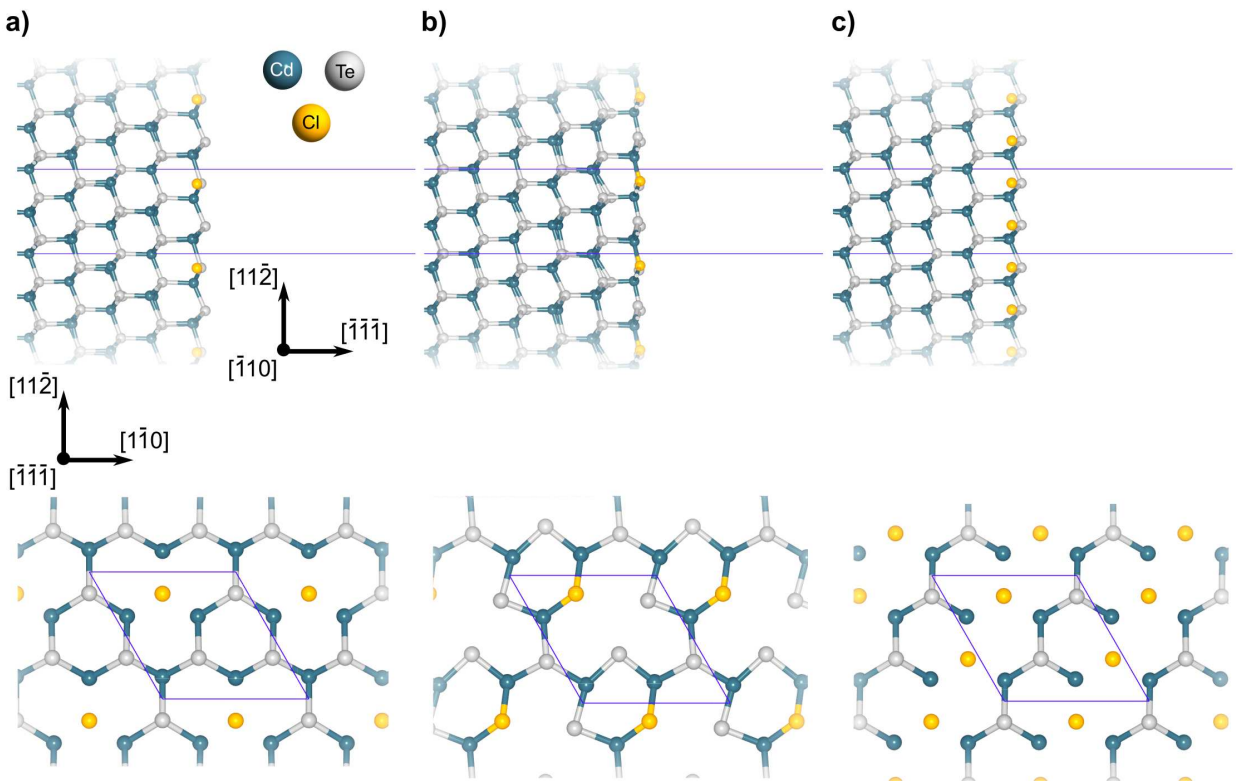

Figure 3.14: Perspective views of the relaxed atomic configurations of CdTe($\bar{1}\bar{1}\bar{1}$) (1 $\times$ 1) surfaces containing (a) 25%, (b) 25% and V_{Cd}, and (c) 50% concentrations of Cl_{Te}. Two views are shown along the transport direction (top subfigure) and perpendicular directions (bottom subfigure) of the one-probe models. The perpendicular view only shows the last two atomic layers in the surface domain for clarity. All surfaces are visualized using the indices provided in (a).

with a height of +0.38 eV at a position from the surface $\delta_{v,cusp}$ = 162.276 Å. If the electronic features existed at the back of CdTe, then they would be beneficial for hole majority carrier transport while creating a barrier for the electron minority carriers. If the features developed in the front of CdTe, then the electrons would be prevented from flowing toward the junction where they can be extracted while holes would freely move through it. The cusp energy potential does not provide any additional assistance as its energy level is still lower than $E_{v,surf}$. The Cl_{Te} defect is said to create a donor-like state, which is not immediately present in the calculated energy band alignment of Figure 3.15a. It may be that since the band gap is smaller at the surface, the neutral state level simply resides within the CB.

The energy band alignment in Figure 3.15b for the 25% Cl_{Te}-V_{Cd} complex pair has many identical features as the previously discussed band alignment for the 25% Cl_{Te} CdTe($\bar{1}\bar{1}\bar{1}$) surface model. Despite the similarities, the Cd vacancy introduces a number of electronic states at the surface that exist around +0.32 eV above E_F. If $E_{v,surf}$ is instead used as the reference, the states reside between 0.00 to +0.35 eV within the energy level region where shallow acceptors are located for a Cd vacancy. Thus the electronic states seen are positioned higher at the surface due to the significant upward bend in the VB. The position of the V_{Cd} energy level is in qualitative agreement with bulk CdTe defect analysis from outside literature [38].

The inclusion of 50% Cl_{Te} on the CdTe($\bar{1}\bar{1}\bar{1}$) surface levels out the VBM and CBM curves as shown in Figure 3.15c. The surface band heights are negligible with relatively little surface states in comparison to the other two simulation models with lesser Cl concentration. If the Te-terminated CdTe($\bar{1}\bar{1}\bar{1}$) surface required flat bands at either junction of the absorber layer, then a Cl concentration closer to 50% would be effective at achieving such a desired band alignment behavior.

Research Impact

The formation of Cl replacing certain Te sites at the CdTe surface leads to an intriguing possibility for the removal of detrimental surface states that exist along the Te-terminated CdTe($\bar{1}\bar{1}\bar{1}$) surface. The inclusion of closer to 50% Cl at the CdTe surface eliminates any dangling bond for-

Table 3.6: Salient electronic features within each CdTe($\bar{1}\bar{1}\bar{1}$) + Cl_{Te} one-probe model. $\delta_{v,cusp}$ indicates the position where the cusp energy potential $E_{v,cusp}$ is determined starting from the termination layer. All energy band alignment values are determined from the macroscopically averaged curve fit of each local density of states plot. Any +/- values indicate energy values referenced to the Fermi level E_F (marked as 0 eV).

Type	Facet	$E_{g,CdTe}$ (eV)	$E_{c,surf}$ (eV)	$E_{v,surf}$ (eV)	$\delta_{v,cusp}$ (Å)	$E_{v,cusp}$ (eV)
Relaxed	Cl_{Te} (25%)	1.39	+0.37	+0.63	162.276	+0.38
	Cl_{Te} (25%) + V_{Cd}	1.39	+0.44	+0.66	166.952	+0.42
	Cl_{Te} (50%)	1.46	+0.01	-0.01	143.570	+0.03

Table 3.7: Surface electronic state energy levels and DOS magnitudes within each CdTe($\bar{1}\bar{1}\bar{1}$) + Cl_{Te} one-probe model. All electronic state energy values for a given facet are chosen according to highest DOS magnitude and are accurate to within $\pm$5 meV.

Type	Facet	E_{def1} (eV)	$D(E_{def1})$ (eV^{-1})	E_{def2} (eV)	$D(E_{def2})$ (eV^{-1})
Relaxed	Cl_{Te} (25%)	-0.09	3.28×10^{-2}	-0.16	8.59×10^{-3}
	Cl_{Te} (25%) + V_{Cd}	+0.13	4.44×10^{-1}	+0.32	5.94×10^{-2}
	Cl_{Te} (50%)	-0.73	2.57×10^{-2}	-0.79	1.03×10^{-2}

mation caused by Te atoms due to Cl having a higher electronegativity and one less electron charge than surface Te.

Interestingly the Cl_{Te} formation layer at high enough concentrations lead to one of two things: 1) alleviation of the upward band bending and 2) minimization of the deleterious effects found at the Te-terminated surface along the ($\bar{1}\bar{1}\bar{1}$) plane associated with dangling bonds. It is evident that 50% Cl_{Te} yields a highly favorable surface that would reduce surface recombination velocity and improve CdTe device efficiency.

3.3.4 TeO_2-Monolayer + Cl_{Te} Formation on CdTe(111) Surface

Research Scope

Experimental studies on CdTe surfaces [111, 112] have seen evidence of a native tellurium dioxide (TeO_2) layer that has led to low interface charge density and thus significant improvements to CdTe electronic properties. It has been suggested that a selective oxidation process occurs on the

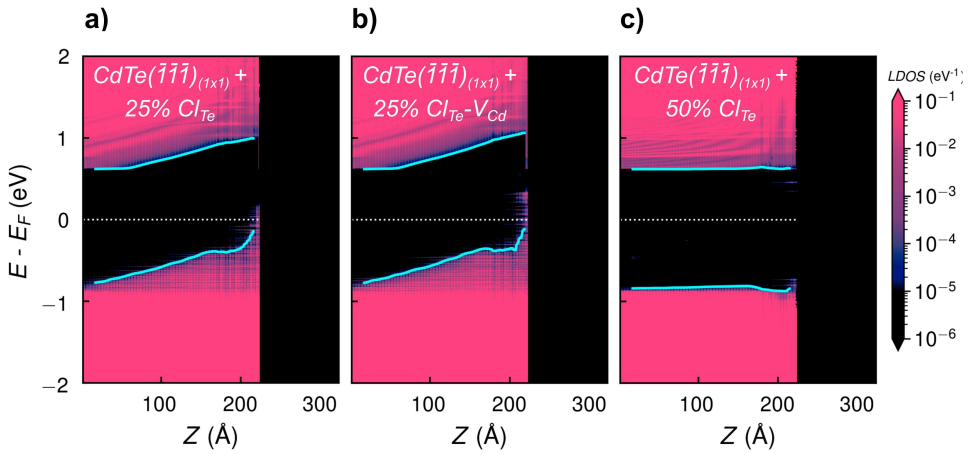

Figure 3.15: Localized density of states mapping across the CdTe($\bar{1}\bar{1}\bar{1}$) (1 × 1) one-probe models containing (a) 25%, (b) 25% and V_{Cd}, and (c) 50% concentrations of Cl_{Te}. Concentration amounts are provided in each image above. The zero energy on the y-axis is referenced by the Fermi level E_F of each respective band alignment profile. The light blue curves are the macroscopically averaged curve fits of the valence band maximum and conduction band minimum, respectively.

CdTe(111) (1 × 1) surface and subsurface with an excess of Te atoms on the CdTe facet [113]. A renewed interest in recent years on TeO_2 within CdTe devices [114, 115] suggest the development of a tellurium dioxide layer after $CdCl_2$ in an oxygen ambient deposition environment may be responsible for some form of passivation of CdTe surfaces. It is thought that the oxygen atoms replace the Cd atoms before and after the last Te layer during the passivation treatment. However, there is no clear understanding from an atomic-scale perspective as to what the oxide layer does to the electronic properties of CdTe surfaces. Therefore, a TeO_2 monolayer formation on the CdTe(111) (1 × 1) surface [113] was modeled to determine what effects TeO_2 has when it forms on a CdTe polar surface.

Energy Band Alignment

The surface model was constructed by using a CdTe(111) Cd-terminated surface and replacing the cadmium atomic layers behind and in front of the last Te layer of the CdTe surface with oxygen atoms. It is worth noting that the modeled form of Te surrounded by two O atoms is from hereon referred to as "TeO_2" with no relation to the conventional description of a crystalline TeO_2 layer. The various crystalline forms of TeO_2 have larger direct band gaps than CdTe [116–118], however

none of them are modeled in the current study. The surface model strictly relies on the assumption that Te and O atoms diffuse to their respective positions following the CdTe(111) (1 $\times$ 1) atomic arrangement as suggested by *Kowalski et al.* [113]. Hydrogen atoms were placed on the end of the last oxygen termination layer to eliminate any residual dangling bonds from the TeO_2 monolayer. The extra hydrogen passivation ensured that only the interface between CdTe and TeO_2 was evaluated and not the TeO_2 surface itself. Figure 3.16 provides a comparison of the TeO_2-terminated model without and with two different concentrations of Cl_{Te} defects on the surface.

In Figure 3.16a, a large amount of deformation occurs to the TeO_2 monolayer. The optimization process causes each individual atom with TeO_2 to shift accordingly so as to minimize the forces present on the surface. The oxidation process is said to diffuse oxygen into the CdTe subsurface and creates an amorphization of the CdTe surface [113], which certainly describes how the CdTe surface looks after the TeO_2 relaxation. The resulting band alignment shown in Figure 3.17a depicts how relaxation has caused several surface electronic states to concentrate close to the Fermi level E_F. Secondly, a noticeable cusp energy potential with a magnitude of 0.56 eV above the CdTe bulk VBM develops at a similar location as the original CdTe(111) (1 $\times$ 1) surface (compared with Figure 3.9b). Once again, the cusp feature is created within the geometry optimized region of the surface model at the location $\delta_{v,cusp}$. Thirdly, the VBM near the surface fluctuates slightly while the CBM remains relatively constant starting at $\delta_{v,cusp}$. In comparison to the original CdTe(111) surface in Figure 3.9b, the addition of a TeO_2 monolayer does not cause the VB to bend downward. Evidently the TeO_2 monolayer by itself can create some sort of field effect that encourages hole transport toward the back of the CdTe PV device. However, the large number of electronic states that reside near the Fermi level could impede carrier flow and as a result counteract some of the improvements gained from the field effect.

The introduction of 25% Cl_{Te} along with the TeO_2 monolayer in Figure 3.16b leads to peculiar features that differ from the TeO_2-only case. After replacing one Te atom joining the CdTe(111) surface to the TeO_2 monolayer with Cl (marked in yellow), the surface is much more well-behaved in terms of relaxation. Despite the improved structual appearance, the energy band alignment for

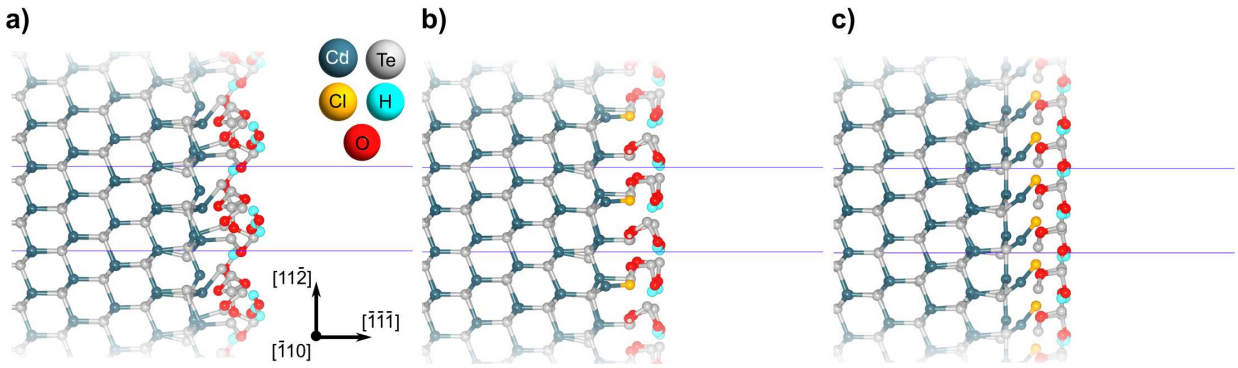

Figure 3.16: Perspective views of the relaxed atomic configurations of CdTe(111) (1 × 1) surfaces containing (a) the TeO_2 monolayer only, (b) TeO_2 with 25% Cl_{Te}, and (c) TeO_2 with 50% Cl_{Te}. The view is shown only along the transport direction with the axis orientation provided in (a).

CdTe(111) (1× 1) + TeO_2 + 25% Cl_{Te} (Figure 3.17b) reveals a significant range of electronic states near or below E_F. Notably, the VBM curve also bends downward to significantly decrease the $E_{v,surf}$ magnitude by 0.59 eV as it approaches the vacuum region. The CBM curve maintains a plateau with a $E_{c,surf}$ magnitude of 0.31 eV as it reaches the surface, a value that is 0.16 eV lower than the TeO_2-only model. At the same time, the $E_{v,cusp}$ height decreases by 0.19 eV after including 25% Cl_{Te}. The CdTe(111) surface model with TeO_2 and Cl_{Te} does contain lower DOS magnitudes than the original TeO_2 monolayer case. However, the modeling case would still suffer from hinderances to hole majority carrier charge transport due to the VB downward bending and wide range of surface states. The electron minority carriers, on the other hand, continue to experience a large field effect from $E_{c,surf}$, showing that lower Cl concentration maintains the CB barrier seen in the first case. The results illustrate the dramatic role that chlorine substitutional defects can play for CdTe(111) (1 × 1) surface energy band alignment.

The last surface model studied incorporated 50% Cl_{Te} between the CdTe(111) Cd sublayer and TeO_2 monolayer. Figure 3.16c reveals that the TeO_2 monolayer flattens out and maintains a structured periodicity. The consequential energy band alignment plotted in Figure 3.17c comprises of a shift in surface states above the Fermi level with the surface VB preserving its downward bending feature. Furthermore, the CBM curve now bends downward as well, imitating many of the electronic characteristics seen in the original relaxed CdTe(111) (1 × 1) surface (Figure 3.9b). The

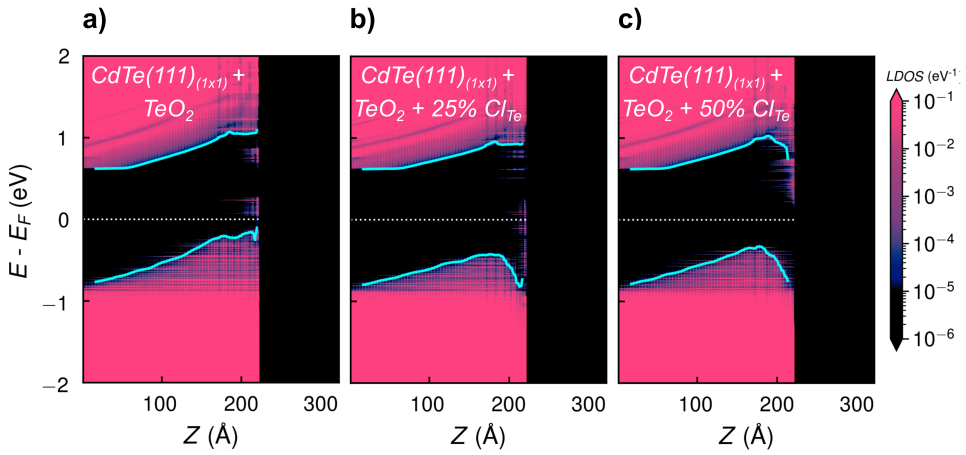

Figure 3.17: Localized density of states mapping across the CdTe(111) (1 × 1) one-probe models combined with (a) a TeO_2 monolayer, (b) TeO_2 + 25% Cl_{Te}, and (c) TeO_2 + 50% Cl_{Te}. Labels for the individual modeling cases are provided in each image above. The zero energy on the y-axis is referenced by the Fermi level E_F of each respective band alignment profile. The light blue curves are the macroscopically averaged curve fits of the valence band maximum and conduction band minimum, respectively.

main difference is that the newly formed TeO_2 monolayer with 50% Cl_{Te} causes the cusp energy potential $E_{v,cusp}$ to display a height of +0.46 eV above the bulk CdTe VBM. The new height is nearly 0.13 eV greater than the cusp energy potential obtained from the unreconstructed CdTe(111) surface energy band alignment. Based on the results, the combination of a TeO_2 monolayer and higher Cl concentration acquires similar energy band alignment properties as the CdTe(111) (1 × 1) surface except for a noticeably larger cusp energy potential.

Table 3.8: Salient electronic features within each CdTe(111) + TeO_2 monolayer one-probe model. $\delta_{v,cusp}$ indicates the position where the cusp energy potential $E_{v,cusp}$ is determined starting from the termination layer. All energy band alignment values are determined from the macroscopically averaged curve fit of each local density of states plot. Any +/- values indicate energy values referenced to the Fermi level E_F (marked as 0 eV).

Type	Facet	$E_{g,CdTe}$ (eV)	$E_{c,surf}$ (eV)	$E_{v,surf}$ (eV)	$\delta_{v,cusp}$ (Å)	$E_{v,cusp}$ (eV)
Relaxed	TeO_2	1.38	+0.47	+0.66	174.448	+0.56
	TeO_2 + Cl_{Te} (25%)	1.42	+0.31	+0.07	173.455	+0.37
	TeO_2 + Cl_{Te} (50%)	1.40	+0.13	+0.04	177.240	+0.46

Table 3.9: Surface electronic state energy levels and DOS magnitudes within each CdTe(111) + TeO_2 monolayer one-probe model. All electronic state energy values for a given facet are chosen according to highest DOS magnitude and are accurate to within ±5 meV.

Type	Facet	E_{def1} (eV)	$D(E_{def1})$ (eV^{-1})	E_{def2} (eV)	$D(E_{def2})$ (eV^{-1})
Relaxed	TeO_2	+0.24	$2.76 \times 10^{+2}$	+0.85	5.02×10^{-1}
	TeO_2 + Cl_{Te} (25%)	+0.10	6.98×10^{-2}	-0.11	6.12×10^{-2}
	TeO_2 + Cl_{Te} (50%)	+0.59	1.94×10^{0}	+0.71	3.39×10^{-1}

Research Impact

The relaxed CdTe(111) + TeO_2 monolayer surface configurations and calculated band diagrams give a unique perspective on how certain electronic properties are modified due to the resultant oxidation process. The TeO_2 monolayer creates several detrimental electronic surface states but creates favorable band alignment attributes that would be beneficial for selective charge carrier transport at the back of the CdTe absorber layer. The same benefits cannot be applied to the front of CdTe as the electronic features would hinder the appropriate charge carriers from flowing along their preferred transport directions. The inclusion of substitutional chlorine at increasing concentrations eventually makes the surface configuration behave as if it were the CdTe(111) (1 × 1) surface without an additional monolayer or substitutional defect. A 50% Cl_{Te} concentration with the TeO_2 monolayer does include a bigger cusp energy potential than the CdTe(111) surface only. But the higher Cl concentration does not remove all surface states as seen for the CdTe($\bar{1}\bar{1}\bar{1}$) + 50% Cl_{Te} simulation model (Figure 3.15c). Clearly, a fine balance is necessary between what modifications are applied to the CdTe polar surfaces by means of oxidation and Cl concentration. Equally important is the effect of termination layer on how the perceived Cl passivation effect is best optimized for CdTe polar surfaces. The complex relationship between relaxation, termination layer and oxide/defect formation on CdTe surfaces provide a comprehensive outlook on the necessity for atomistic modeling of CdTe surfaces for CdTe-based PV applications.

3.3.5 Limitations of CdTe Surface Studies

The DFT+GF method for simulating CdTe surfaces demonstrates its efficacy in determining energy band alignments from an atomistic viewpoint as opposed to the conventional heuristic theories such as the Anderson Rule. However, several limitations have developed as a result of the current simulation setup that must be brought to the reader's attention.

The first limitation is that some simulation domain sizes may have resulted in less accurate bulk CdTe band gap values that initially were in good agreement with experimental values for DFT bulk calculations. The reason for the discrepancy is that the calculated electrostatic potentials after solving Poisson's equation for polar CdTe surfaces contained large magnitudes for $V(z)$ in (3.1). To accommodate the effect, the depletion width z_{dep} must be sufficiently long enough as the electrostatic potential moves further from the surface (increases in z) and converges to the bulk value. If the system size is not extended far enough to capture the screening length, then there will be a slight decrease to the CdTe band gap $E_{g,CdTe}$ as measured by the macroscopic average. One way to compensate for the screening length without physically increasing the domain size would be to increase the doping concentration within the CdTe surface model. This would effectively increase N_A in (3.1), forcing the depletion width z_{dep} to decrease and thus arrive at the same electrostatic potential $V(z)$ magnitude. Since the typical p-type concentration in intrinsic polycrystalline CdTe absorber layer is 2×10^{14} cm^{-3}, the depletion width for some of the CdTe surface models was too large to capture with the modeling domain size used. Despite the slightly underestimated bulk CdTe band gaps, the typical CdTe surface domain lengths were $\sim$20 nm, which is much larger than conventional DFT simulations to date. Thus it is expected that the CdTe surface simulations under consideration still offer valid surface energy band alignments.

The second limitation is that thermodynamic processes involved in CdTe deposition are not described at all within the current CdTe surface studies. The DFT+GF one-probe models only calculate the electronic properties at temperature T = 0 K, meaning that only the ground state energy is considered throughout the system domain and not excited state energies. One way to possibly include thermodynamic effects in the system would be to first simulate the thin film deposition

process by means of molecular dynamics (MD) algorithms. MD simulations are used to describe the statistical ensembles of systems while at the same time allowing for the system to change in response to temperature. If the CdTe deposition process could be initially simulated by MD with temperature effects included, then the energy band alignment of the resulting CdTe surface after MD can be calculated using the DFT+GF method. A similar concept is proposed in Chapter 5 and is planned to be implemented in future surface and interface studies.

The last limitation is related to the description of the CdTe surface itself. Although care was taken to model possible unreconstructed and reconstructed CdTe surfaces seen within experimental studies of CdTe epitaxial growth, not all possible surface periodicities were investigated. Furthermore, the models are simplified representations of single crystal CdTe facets oriented along one plane, which is not entirely accurate if applied to more complex surfaces found on polycrystalline CdTe thin film layers. A large CdTe surface system with various CdTe grains terminating with different orientations and species would be most representative of actual CdTe surfaces during less controlled deposition techniques such as close space sublimation. However, the work is limited in computational resources available for such a complex system, even with the usage of the Summit supercomputer [56]. Nonetheless, the sophisticated high-fidelity DFT+GF one-probe models of the CdTe surface at the very least provides a new atomistic perspective of surface energy band alignment not performed within the CdTe research community.

3.4 Summary of Key Findings

The DFT+GF one-probe models of the CdTe surfaces elucidates the various effects on energy band alignment due to plane orientation, termination layer, surface relaxation and reconstruction. The CdTe surfaces were organized into four general classification studies, each adding its own unique piece to the atomistic modeling puzzle used to describe any possible mechanisms affecting CdTe PV device performance. The following list summarizes the major key findings associated with the four main CdTe surface studies:

Cd-Terminated CdTe Surfaces

1. Unrelaxed (1 $\times$ 1) plane orientations of the Cd-terminated CdTe surfaces dictate the surface potential magnitude. The unrelaxd polar CdTe(111) surface in general bends downward more than the CdTe(100) surface as proposed by surface polarity.

2. Stable surface reconstructions for Cd-terminated CdTe surfaces improve the energy band alignment profiles due to the charge neutrality conditions achieved by respective Cd vacancies. Both the CdTe(100) c(2 $\times$ 2) and CdTe(111) (2 $\times$ 2) facets satisfy the electron counting rule and are thus accompanied by well-behaved energy band alignments.

3. Relaxation of the CdTe surfaces provide cleaner surface electronic properties and are more representative of the characteristics seen for actual CdTe surfaces.

4. A newly identified electronic feature described as an cusp energy potential develops only after relaxation of the CdTe surface, primarily for the CdTe(111) plane orientation. The cusp energy potential is proposed as one of the mechanisms leading to enhance hole majority carrier transport at the back of the CdTe absorber layer and may improve CdTe PV device performance.

Te-Terminated CdTe Surfaces

1. Te-terminated CdTe surfaces cause the VB and CB to bend upward due to a negative charging effect at the termination layer. The band bending behavior is opposite to the Cd-terminated CdTe surfaces, which correctly follows surface theory. The Te-terminated surface energy potential magnitudes are typically greater than the Cd-terminated ones and could possibly assist with charge transport due to a strong field effect resulting from band bending.

2. Higher numbers of surface electronic states are present for Te-terminated CdTe surfaces in comparison to the Cd-terminated cases. It is uncertain if such states are secondary pathways for hole carrier transport or if they only act as traps due to how closely spaced together they are along the surface.

3. Similar improvements to energy band alignment are realized for the CdTe($\bar{1}00$) c(2×2) and CdTe($\bar{1}\bar{1}\bar{1}$) (2×2) surface reconstructions as in the Cd-terminated cases. Again, the reconstructed CdTe surfaces obey the ECR and thus present minimal surface states compared to their unreconstructed variants.

4. Cusp energy potentials still appear in the CdTe($\bar{1}\bar{1}\bar{1}$) cases at similar relaxation length locations. However, the upward band bending in the energy band alignments mask their possible effect on charge transport.

CdTe($\bar{1}\bar{1}\bar{1}$) Surface + Cl_{Te}-Formation

1. Cl concentrations near 25% on the relaxed CdTe($\bar{1}\bar{1}\bar{1}$) surface still retain the upward band bending present in the original CdTe($\bar{1}\bar{1}\bar{1}$) cases. There is no significant difference in the surface electronic states as well.

2. The combination of a Cd vacancy along with 25% Cl_{Te} creates more surface states and may actually be more harmful for CdTe PV device performance.

3. Optimized energy band alignment conditions are achieved for 50% Cl_{Te} with flatter bands and a significant reduction to surface electronic states.

CdTe(111) Surface + TeO_2 Monolayer + Cl_{Te}-Formation

1. All TeO_2 monolayer (according to the proposed oxidation process) one-probe models without and with Cl_{Te} develop larger cusp energy potentials than the original CdTe(111) surface.

2. TeO_2 monolayer contains surface states closer to the Fermi level but also flattens the CB and VB near the surface.

3. TeO_2 + 25% Cl_{Te} results in the VB bending downward but the CB remaining flat closer to the surface.

4. TeO_2 + 50% Cl_{Te} contains energy band alignment features that closely resemble the original CdTe(111) surface. The single major difference is a larger cusp energy potential, which may increase hole majority carrier transport at the back of CdTe PV devices.

Overall, the DFT+GF one-probe model provides a complex description of CdTe surfaces from an atomistic perspective that is beyond the scope of theoretical models such as the Anderson Rule. The powerful computational method allows for a comprehensive explanation of how various CdTe surface characteristics alter the energy band alignment features. As a result, the DFT+GF one-probe model has wide application for determining the electronic aspects of thin film surfaces with the potential to advance their respective semiconductor and PV technologies.

Chapter 4

DFT+GF Two-Probe Modeling of the CdTe/Te Interface

The development of well-behaved heterostructures have led to the success of thin film semiconductor technologies in past decades. The famous quote made by Nobel Physics Laureate Herber Kroemer states that "the interface is the device" [119], reaffirming the essential role that interfaces play in semiconductor devices. Much debate has existed within the research community as to what is the most appropriate representation for interfaces and their underlying electronic characteristics. As previously mentioned in Section 1.2, one common yet simplistic model used for energy band alignment at the interface is the Anderson Rule [30]. However, the Anderson Rule neglects complex electronic features that are dependent upon atomic-scale attributes found at the interface. In fact, nonuniform semiconductors caused by non-homogeneous impurity distributions and/or elastic strains will separately alter the CB and VB band bending features [120]. That is why an atomistic modeling approach to energy band alignment is necessary for accurately calculating the electronic features seen at the interface regions between two dissimilar materials.

This chapter focuses primarily on energy band alignment of the CdTe absorber layer and the Te back contact using DFT coupled with Green's function. The study utilized the two-probe interface model to describe the electronic phenomena that occurs at the CdTe/Te interface when different plane orientations and terminated surfaces are applied at the junction. It was expected that CdTe/Te interface would exhibit similar energy band alignment characteristics as the CdTe surface models described in Chapter 3 with an additional charging effect on the terminated surface. A full investigative procedure of the CdTe/Te interface is provided throughout the following sections.

4.1 Introduction

Advancements in CdTe-based thin film solar cell technologies have led to significant improvements in device efficiencies in recent decades. As mentioned in Section 1.1, CdTe PV research performed at Colorado State University has resulted in the achievement of an overall CdTe PV cell efficiency of 19.2% [23], in part due to the implementation of a Te back contact in the CdTe device configuration. The device architecture for the typical CdTe solar cell with the inclusion of a Te back contact is illustrated in Figure 4.1a. CdTe absorber layers that directly form a junction with metal back contacts usually develop Schottky back barriers that lead to decrease fill factors [121] and thus compromised CdTe PV device performances. There is some suggestion that an optimized concentration of Te acting as a back surface field layer tends to increase the short circuit current and fill factor of the CdTe solar cell [122]. Te layer thicknesses around 30 nm and above are suitable for obtaining the benefits in CdTe thin film PV and avoid the inversion from p-type to n-type character in the Te layer that occurs at thicknesses less than 5 nm [84]. Figure 4.1b demonstrates the current density vs. voltage (J-V) curves that characterize the electronic behavior of actual CdTe devices without and with an evaporated Te back contact. It is clear that without Te the J-V curve develops a kink with increasing voltage bias that negatively impacts the device efficiency. On the other hand, the Te layer creates a favorable back contact between the CdTe absorber layer and back metal electrode that restores the diode characteristics essential to CdTe device performance. It is important to emphasize the fact that both experimental CdTe PV devices do not contain intentional Cu doping, validating the fact that the Te back contact somehow leads to improved J-V properties. However, the mechanisms responsible for the enhanced CdTe device performance after using a Te back contact layer are not well understood. The two-probe DFT+GF CdTe/Te interface model was developed with the intention of shedding light on the factors responsible for improved CdTe device performance after depositing a Te back contact onto CdTe.

The reason for modeling the CdTe/Te interface is to distinguish the mechanisms leading to improved charge carrier behavior at the interface. As mentioned in Section 1.2, Anderson's Rule references a common vacuum energy level for the bulk materials in the system, whereupon the

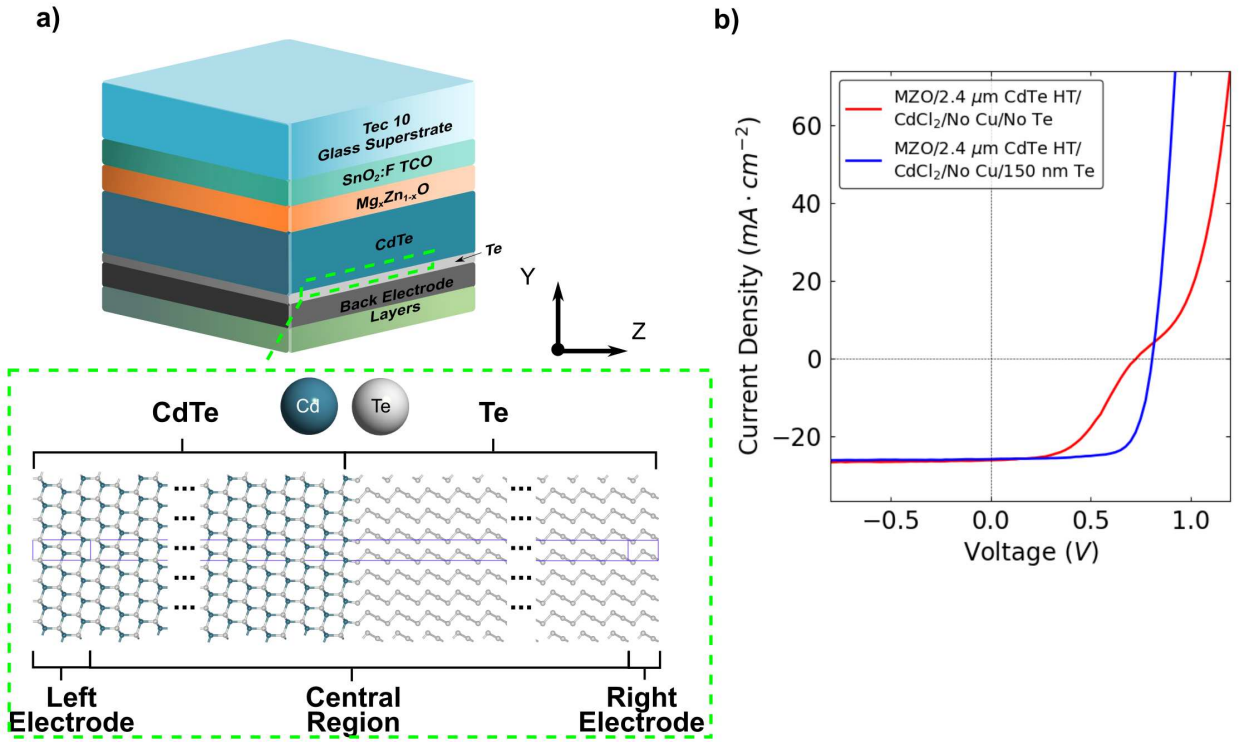

Figure 4.1: (a) Typical CdTe device configuration with the region of interest for DFT+GF modeling of the CdTe/Te interface; (b) experimentally measured J-V curve without (red curve) and with (blue curve) a Te back contact in the CdTe PV device configuration.

electron affinities χ and band gaps E_g of the bulk materials are used to construct the band alignment and calculate the resulting electronic properties due to band offsets (see Figure 1.4). Anderson's Rule does not accomodate for plane orientation, interface states, lattice mismatch, and termination layers at the interface and thus cannot accurately capture the complex phenomena that occurs at the CdTe/Te interface. That is why a detailed atomistic modeling approach based on the DFT+GF method was implemented to explore the different effects that interfacial properties (i.e. plane orientations, terminated surfaces and relaxation) have on the CdTe/Te interface.

Evaluation of the fourth hypothesis was carried out by studying the CdTe(111)/Te(0001) and CdTe($\bar{1}\bar{1}\bar{1}$)/Te(0001) interfaces. As a reminder, the fourth hypothesis assumes that the CdTe/Te interface can be constructed by adding either the unrelaxed or relaxed CdTe and Te surface results together along with an interface dipole in the form of a superposition. The hypothesis relies on the understanding that both the unrelaxed and relaxed termination layers of the surface models with

the same plane orientation dictates banding bending features. The surface behavior was expected to project the same characteristics after forming a junction between the CdTe facet with the Te thin film layer that includes an interface dipole before and after relaxation.

4.2 Computational Details

The two-probe model setup was performed with the QuantumATK software and consisted of a Cd and Te-terminated CdTe layer that was oriented along the{111} family of planes while the Te layer was oriented only along the (0001) plane. Another two-probe model with the (100) plane orientation for Cd-termintated CdTe was combined with Te(0001) layer to understand how plane orientation affected interfacial energy band alignment. The modeling domain sizes for the CdTe(111)/Te(0001) and CdTe(100)/Te(0001) interfaces as well as electronic and structural parameters are shown in Table 4.1. All CdTe/Te interface simulations were performed with the FHI+OMX pseudopotentials with their respective double-zeta polarized and low (s2p2d1) basis sets under the LCAO scheme. As in the surface modeling cases, the LDA-PZ exchange-correlation functional was used for all DFT+GF two-probe modeling calculations. A one-probe surface model for the Te(0001) facet was calculated and used the exact same parameters as the two-probe models to later verify fourth hypothesis in Section 4.3.3. The two-probe CdTe/Te interface simulations were calculated with a Monkhorst Pack grid for the k-point sampling distribution. The number of k-points used for the CdTe{111}/Te models was 7 $\times$ 7 $\times$ 100 (4.421 Å $\times$ 4.421 Å $\times$ 178.631 Å) while the CdTe(100)/Te models used 3 $\times$ 6 $\times$ 150. All simulations used a density mesh-cutoff of 2200 eV. A Hubbard-U correction was applied to the Cd-4d and Te-5p orbitals of CdTe{111} simulations with values U_{Cd-4d} = 4.60 eV and U_{Te-5p} = 2.55 eV, respectively, to yield a CdTe band gap value comparable to the experimental measurement of 1.49 eV [34]. For the thin film Te layer, only the Te-5p subshell with a value of U_{Te-5p} = 0.73 eV was applied to establish a proper band gap value close to the experimental value of 0.33 eV [123].

The Te layer had an in-plane mean absolute strain associated with it (see Table 4.1) while the CdTe layer lattice parameter was kept equal to the experimental value of 6.480 Å [77]. It was

assumed that the strain should only be applied the Te layer since during the fabrication process Te is evaporated as the thinnest layer on the CdTe absorber layer. The poisson effect created by the in-plane strain on Te was included in all simulations by relaxing the Te bulk electrode cell in the z-direction until the stress was below 0.005 eV/Å^3. It was later verified that accomodating for the poisson effect did not make a significant difference to electronic properties at the CdTe/Te interface but were still included for consistency.

Geometry optimization with a force threshold of 0.01 eV/Å was carried out for all relaxed CdTe{111}/Te(0001) simulation studies. As for the CdTe(100)/Te(0001) two-probe model, a value of 0.02 eV/Å was established due to the significantly larger system size and thus higher computational demand. At least 5 nm on the CdTe side and Te side nearest the CdTe/Te interface were relaxed, following a relaxation domain size similar to the CdTe surface modeling cases. The domain lengths for the central regions of the CdTe(111) and CdTe(100) plane orientations in the CdTe/Te interface models are depicted in Figure 4.2. Large domain sizes in each simulation were used in an attempt to account for screening effects that involved band bending over several nanometers that similarly occurred for the CdTe surface simulations. Secondly, the decay of interfacial electronic states between the Te layer band edges needed to be accomodated with an increased domain size to minimize their effects on modeling convergence. However, computational demands due to the supercell sizes have limited their dimensions to current modeling sizes. Semi-infinite boundary conditions consisting of the CdTe left electrode and Te right electrode were used for the calculation of the system as illustrated in Figure 4.2.

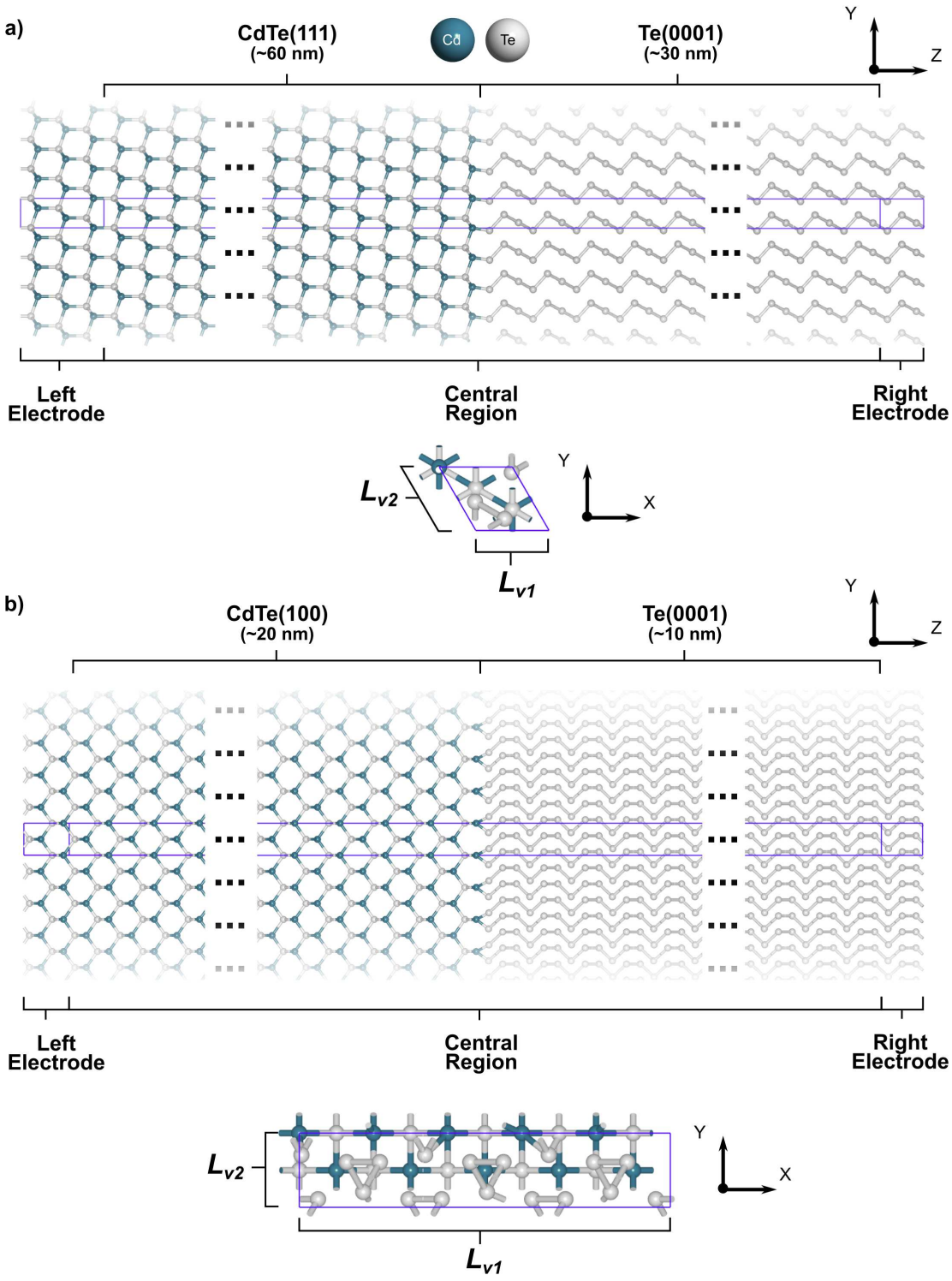

Figure 4.2: (a) CdTe(111) and (b) CdTe(100) plane oriented CdTe/Te interface model schematics with typical lengths along the YZ plane for the central region. The bottom inset of (a) and (b) are the cross-sectional views of the models along the YX plane for clarity of the supercell size. The domain cross-sectional lengths L_{v1} and L_{v2} are both 4.582 Å in (a), while for (b) they are 7.637 Å and 4.582 Å, respectively.

Table 4.1: Two-probe modeling domain parameters for the unrelaxed (u) and relaxed (r) CdTe/Te interfaces. Both the *"bulk"* and *"cr"* subscripts denote the bulk and central region, respectively.

Model	Interface Layers	Carrier Conc. (p-type), ρ (cm^{-3})	$L_{z,bulk}$ (Å)	$L_{z,cr(u)}$ (Å)	$L_{z,cr(r)}$ (Å)	N_{bulk}	N_{cr}	Mean Abs. Strain (%)	Poisson Effect, $\Delta z/z$ (%)
1,2	CdTe(111)/	2e14	11.224	615.900	616.237	6	330		
	Te(0001)	1e20	5.852	323.211	322.625	3	165	2.03	1.06
3,4	CdTe($\bar{1}\bar{1}\bar{1}$)/	2e14	11.224	615.900	615.191	6	330		
	Te(0001)	1e20	5.852	322.777	323.315	3	165	2.03	1.06
5	CdTe(100)/	2e14	6.480	n/a	207.385	20	640		
	Te(0001)	1e20	5.899	n/a	106.783	18	324	1.30	0.27

4.3 Results and Discussion

Evaluations of the unrelaxed and relaxed CdTe/Te interfaces with respect to termination layer and plane orientation were performed for the DFT+GF two-probe models listed in Table 4.1. A detailed study of the three models was necessary to capture all the electronic and structural dependencies that the CdTe/Te interface exhibits on an atomic-scale. Conclusions were made on the interfacial mechanisms contributing to and/or hindering the improvement of CdTe device performance. Lastly, verification of the fourth hypothesis was done to determine whether the CdTe and Te surface models could effectively describe the combined effects residing at the CdTe/Te interface region.

4.3.1 Interfacial Energy of CdTe{111}/Te(0001) Interfaces

The interfacial energy γ_{int} of the CdTe/Te interface was used to determine the energetics of interaction between the CdTe and Te layers that create the interface region. As opposed to the surface energy of a system, which must always be positive to be stable, the interfacial energy can be positive or negative. A negative value would denote a more thermodynamically stable system than the separate systems in isolation [124]. The following equation describes the method of calculating the interfacial energy γ_{int} using the two-probe modeling approach:

$$\gamma_{int} = \frac{1}{2A}\left[E_{tot,int} - E_{tot,CdTe}\frac{N_{cr,CdTe}}{N_{bulk,CdTe}} - E_{tot,Te}\frac{N_{cr,Te}}{N_{bulk,Te}}\right] \tag{4.1}$$

where A is the cross-sectional area of the two-probe modeling domain and $E_{tot,int}$, $E_{tot,CdTe}$ and $E_{tot,Te}$ are the DFT total energies of the relaxed CdTe/Te interface system and unrelaxed CdTe and Te bulk systems, respectively. The calculated γ_{int} value for CdTe(111)/Te(0001) interface was -2.60 J/m^2 while the CdTe($\bar{1}\bar{1}\bar{1}$)/Te(0001) system gave -2.89 J/m^2. According to (4.1), both CdTe/Te interfaces are more energetically favorable than the isolated bulk systems. With a difference of $\Delta\gamma_{int}$ = 0.29 J/m^2, the CdTe($\bar{1}\bar{1}\bar{1}$)/Te(0001) interface is predicted to be the more stable heterostructure. *Brown et al.* have also suggested that the Te-terminated CdTe surface gives the best epitaxial growth conditions for (Hg,Cd)Te layers [96], which may be related to its more stable

interfacial energy. In any case, both energy band alignments for either termination layer were still investigated to gain a general outlook on the effect of various CdTe facet properties.

4.3.2 Detailed Analysis of {111} Plane Oriented CdTe + Te(0001) Interface Energy Band Alignments

Chapter 3 looked extensively at the relaxation effects on CdTe surface energy band alignment with different termination layers, which provided useful information on how GO optimizes the band alignment features. The unrelaxed and relaxed DFT+GF interface calculations were performed once again to distinguish the effects that relaxation had on the interface as well as to compare to the common band alignment theories like Anderson's Rule. Both the CdTe(111) and CdTe($\bar{1}\bar{1}\bar{1}$) facets joined with the (0001) plane oriented Te layer were studied to see if similar trends could be ascertained from the previously studied CdTe surface models.

The energy band alignments of the unrelaxed and relaxed Cd-terminated CdTe(111)/Te(0001) two-probe interface models are provided in Figure 4.3a and Figure 4.3b. Both the unrelaxed and relaxed Te-terminated CdTe($\bar{1}\bar{1}\bar{1}$)/Te(0001) models are plotted in Figure 4.4a and Figure 4.4b, respectively. Due to the large continuous interface states that appeared with the CdTe/Te interface region for the models, the macroscopically averaged VBM and CBM curve fits could not be effectively plotted. However, many of the important features were measured using several points labeled in Figure 4.3a for further analysis of the band alignment data. E_i energy and Z_i position measurements of the labeled points are provided in Table 4.2. The crude measurements are not as algorithmically consistent as the macroscopic averaging, but at least provide a general view of the energy magnitude of the features. The following energy differences were used for determining the important electronic features seen in previous chapters and were recorded in Table 4.3:

$$\Delta E_{g,CdTe} = E_2 - E_1 \qquad \Delta E_C = E_4 - E_7 \qquad \Delta E_{c,surf} = E_4 - E_2$$

$$\Delta E_{g,Te} = E_7 - E_6 \qquad \Delta E_V = E_6 - E_5 \qquad \Delta E_{v,surf} = E_5 - E_1$$

$$\Delta E_{v,cusp} = E_3 - E_1$$

In Figure 4.3a and Figure 4.4a, the unrelaxed DFT+GF band alignment cases already provide several different features than what the Anderson Rule predicts. In general, the calculated models show an energy band alignment that correctly follows a Type I heterojunction interface as predicted by the Anderson Rule. However, the calculated band alignments tend to have upward VB and CB band bending at the interface. The band bending in the Te-terminated CdTe cases are qualitatively consistent with surface models, but for the Cd-terminated cases an upward bend is contrary to what was calculated by the surface model. Thus, the Te back contact layer is influencing the band bending at the interface that differs from the isolated CdTe surface cases.

In regards to the bulk band gap values for CdTe and Te, the CdTe band gap is well-converged with a domain length greater than 60 nm. Although there is a small curvature to the extended bulk region of the energy band alignments, the screening length is assumed to be captured and thus should not influence the calculated band alignment features. On the other hand, the Te band gap is slightly lower than the experimental value due to the interface strain that was introduced after creating the CdTe/Te interface. It is well-known that changes to the bulk semiconductor crystal due to strain will induce a change in the VB energy level in the form of a deformation potential [124, 125]. The interface strain has caused a change to the band gap, which is why the Te band gap is smaller than its expected bulk value.

Looking more specifically at the relaxed interface simulations, the electronic characteristics on both sides of the CdTe{111}/Te(0001) interface that were noticeably affected by the geometry optimization length. The VB and CB band offsets ΔE_V and ΔE_C found in Table 4.3 for the Cd and Te-terminated CdTe/Te interface models differ by 0.24 eV and 0.33 eV, respectively. Both relaxed cases contain VB offset values that are in agreement with the experimental value of 0.6 ± 0.1 eV

obtained from photoelectron spectroscopic characterization studies of CdTe/Te band alignment performed by *Fritsche et al.* [34, 126].

Furthermore, Figure 4.3b shows that a cusp energy potential $E_{v,cusp}$ with a height of 0.34 eV above the bulk CdTe VBM is created as seen for the CdTe(111) surface one-probe modeling results. For the CdTe($\bar{1}\bar{1}\bar{1}$) case (Figure 4.4b) that cusp energy potential is much smaller at 0.12 eV above the CdTe bulk VBM. Regardless of energy magnitude, both relaxed CdTe{111}/Te(0001) interface simulations have a cusp feature due to the relaxed region that forms after GO. The resulting deformation due to the force minimization process across 5 nm on the CdTe side causes the CdTe VB to change in response. No concrete statements can be made on if the cusp feature is relevant to electronic polaron distortion [127, 128] or just simply a localized deformation potential (or both). In any case, the energy band alignments show that the cusp is confined by the GO region near the back of the CdTe layer. A cusp energy potential has been suggested to form by *Fritsche et al.* as a tunneling effect since they concluded that a Te back contact does not create an Ohmic contact between CdTe and the metal electrode [126]. It must be noted that they contribute the cusp energy potential formation to a p^+-doping mechanism at the back of CdTe as opposed to a strain effect as suggested in this work. The Mulliken charge analysis was thus utilized to de-couple any charge transfer mechanisms causing the cusp feature from developing as opposed to the strain mechanism.

Table 4.2: Labeled points data for calculating salient electronic features within the unrelaxed (*u*) and relaxed (*r*) CdTe{111}/Te(0001) interface two-probe models. Termination layer is denoted below as "Cd-Term." and "Te-Term." for the Cd and Te terminations of the CdTe layer, respectively. Any +/- values indicate energy values referenced to the Fermi level E_F (marked as 0 eV). All energy and positional values are in eV and Å, respectively. Energy values are within ± 0.01 eV while Z positions are within ± 1 Å.

Model	E_1	Z_1	E_2	Z_2	E_3	Z_3	E_4	Z_4	E_5	Z_5	E_6	Z_6	E_7	Z_7
Cd-Term.*(u)*	-0.85	5	+0.64	5	n/a	n/a	+0.96	595	-0.39	605	-0.08	930	+0.18	930
Cd-Term.*(r)*	-0.86	5	+0.64	5	-0.52	560	+1.01	600	-0.51	600	-0.08	930	+0.18	930
Te-Term.*(u)*	-0.85	5	+0.63	5	-0.81	500	+0.74	597	-0.70	597	-0.08	930	+0.18	930
Te-Term.*(r)*	-0.86	5	+0.63	5	-0.74	514	+0.77	586	-0.84	593	-0.08	930	+0.18	930

Table 4.3: Calculated electronic features from Table 4.2 within the unrelaxed (*u*) and relaxed (*r*) CdTe{111}/Te(0001) interface two-probe models. Termination layer is denoted below as "Cd-Term." and "Te-Term." for the Cd and Te terminations of the CdTe layer, respectively.

Model	$E_{g,CdTe}$ (eV)	$E_{g,Te}$ (eV)	ΔE_C (eV)	ΔE_V (eV)	$E_{c,surf}$ (eV)	$E_{v,surf}$ (eV)	$E_{v,cusp}$ (eV)
Cd-Term.*(u)*	1.49	0.26	0.78	0.31	0.32	0.46	n/a
Cd-Term.*(r)*	1.50	0.26	0.83	0.43	0.37	0.35	0.34
Te-Term.*(u)*	1.48	0.26	0.56	0.62	0.11	0.15	0.04
Te-Term.*(r)*	1.49	0.26	0.59	0.76	0.14	0.02	0.12

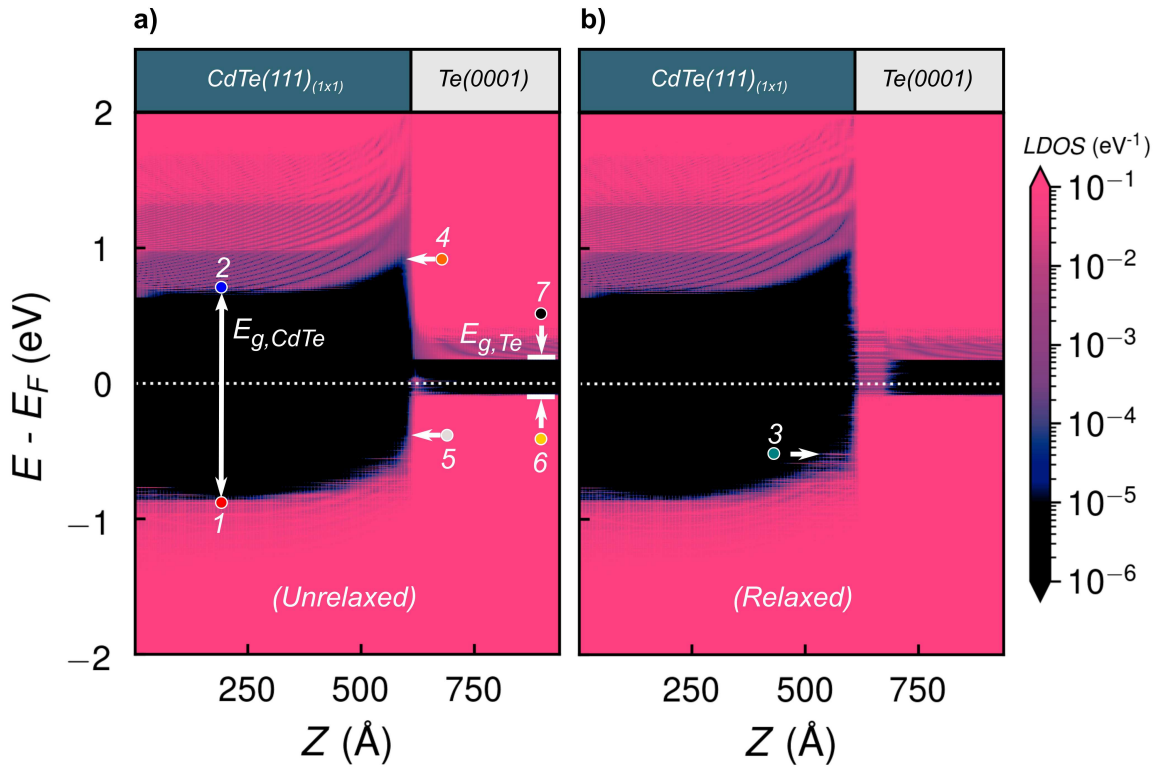

Figure 4.3: Two-probe CdTe(111)/Te(0001) interface energy band alignments for (a) unrelaxed and (b) relaxed interface regions. Several point labels are provided on (a) as an example of where the pertinent electronic features are measured.

One way to evaluate whether the cusp energy potential features are due to charging effects is by plotting the atomic charges across the entire modeling domains. The Mulliken charge analysis was thus evaluated along each atomic site throughout the modeling domain to identify the charging effects associated with the different CdTe terminations. The determination of the atomic charge distribution throughout the CdTe/Te interface enables a unique perspective on whether charge transfer contributes to the cusp energy potentials developed in the CdTe{111}/Te cases. It must be noted that only the valence electrons of the atomic sites were considered in the analysis as performed in another metal chalcogenide DFT study [129] and not the charge involved within the bonds between the atoms. Figure 4.5 contains the atomic charges across both unrelaxed and relaxed CdTe{111}/Te(0001) interfaces with each Cd and Te element marked by separate colors. In all interface models, it is clear that the atomic charges sufficiently far away from the interfacial re-

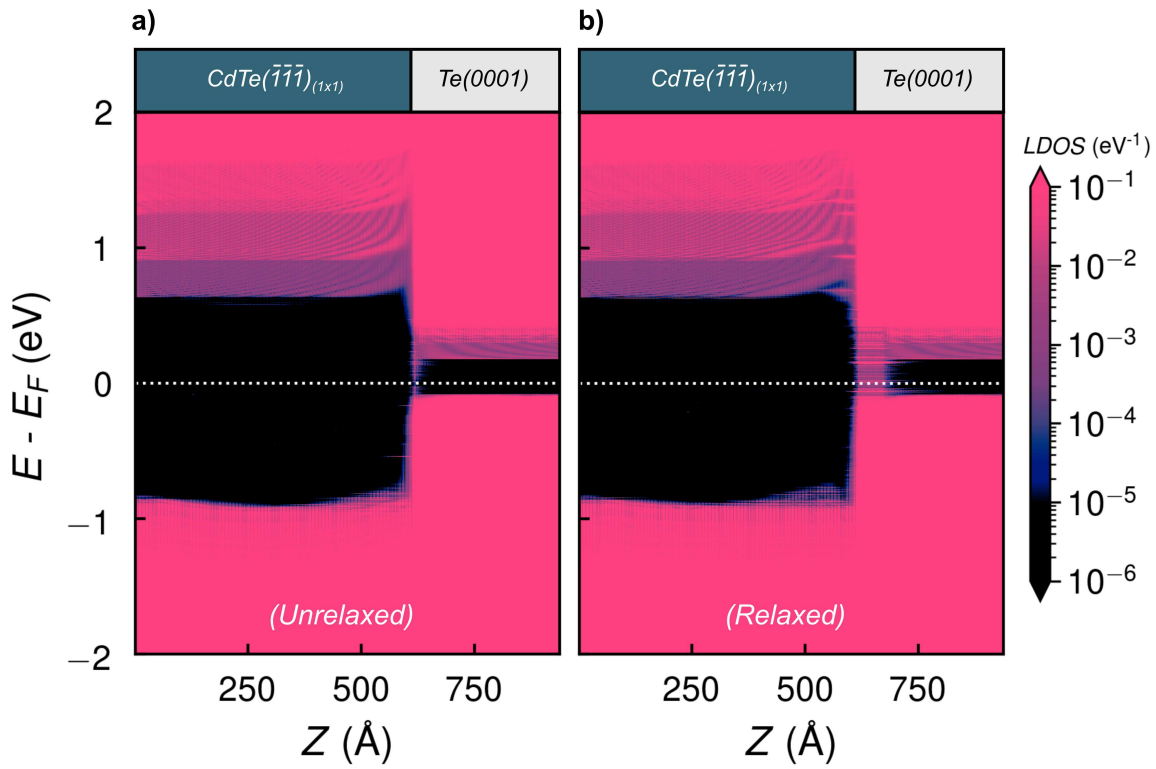

Figure 4.4: Two-probe CdTe($\bar{1}\bar{1}\bar{1}$)/Te(0001) interface energy band alignments for (a) unrelaxed and (b) relaxed interface regions.

gions are balanced with positive and negative charges on the Cd and Te atoms, respectively. There is around 0.9e charge transfer between the Cd and Te atoms, which qualitatively shows that the Cd atom correctly behaves as the cation-like atom and Te acts as the anion-like atom. Although there are slight differences in charge transfer occurring at the interfaces, there is no indication that would suggest the formation of a cusp energy potential is strictly due to charge transfer. A large charging effect would be easily discernible from the plots at the same Z distance as where the cusp feature appears, but there is negligible change in atomic charge near that area. As far as the CdTe{111}/Te(0001) two-probe models are concerned, the cusp feature is primarily due to the strain effect that exists within the GO region rather than a charging effect of the atoms in the cusp location.

As suggested in the CdTe{111} surface models, the cusp feature that develops on the CdTe side of the CdTe{111}/Te(0001) interface may directly contribute to enhancing hole transport toward the back of CdTe as a possible tunneling effect. The current DFT+GF modeling results show that the cusp develops from strain-induced deformation instead of charging effects from charge transfer on the atoms within the same location. However, the actual role for the cusp energy potential has not been studied on the mesoscopic-scale for charge transport within the CdTe PV device. The systematic integration of energy band alignment results obtained from the DFT+GF model such as the cusp energy potential with numerical device modeling tools will be investigated in future work.

4.3.3 Qualitative Assessment of Surface vs. Interface-Derived Te(0001) Energy Band Alignments

Although interesting characteristics were found on the CdTe side of the CdTe/Te interface two-probe models, the Te side likewise provides non-trivial electronic features. Figure 4.6 depicts the unrelaxed and relaxed Te(0001) surface models for comparison to the energy band alignment obtained by the two-probe version of the Te(0001) layer. First, both the Te surface and interface-derived energy band alignments have flat VBM and CBM levels due to the strong p-type character of the Te layer. Secondly, a closer look at Figure 4.6 reveals that the Te surface electronic states are

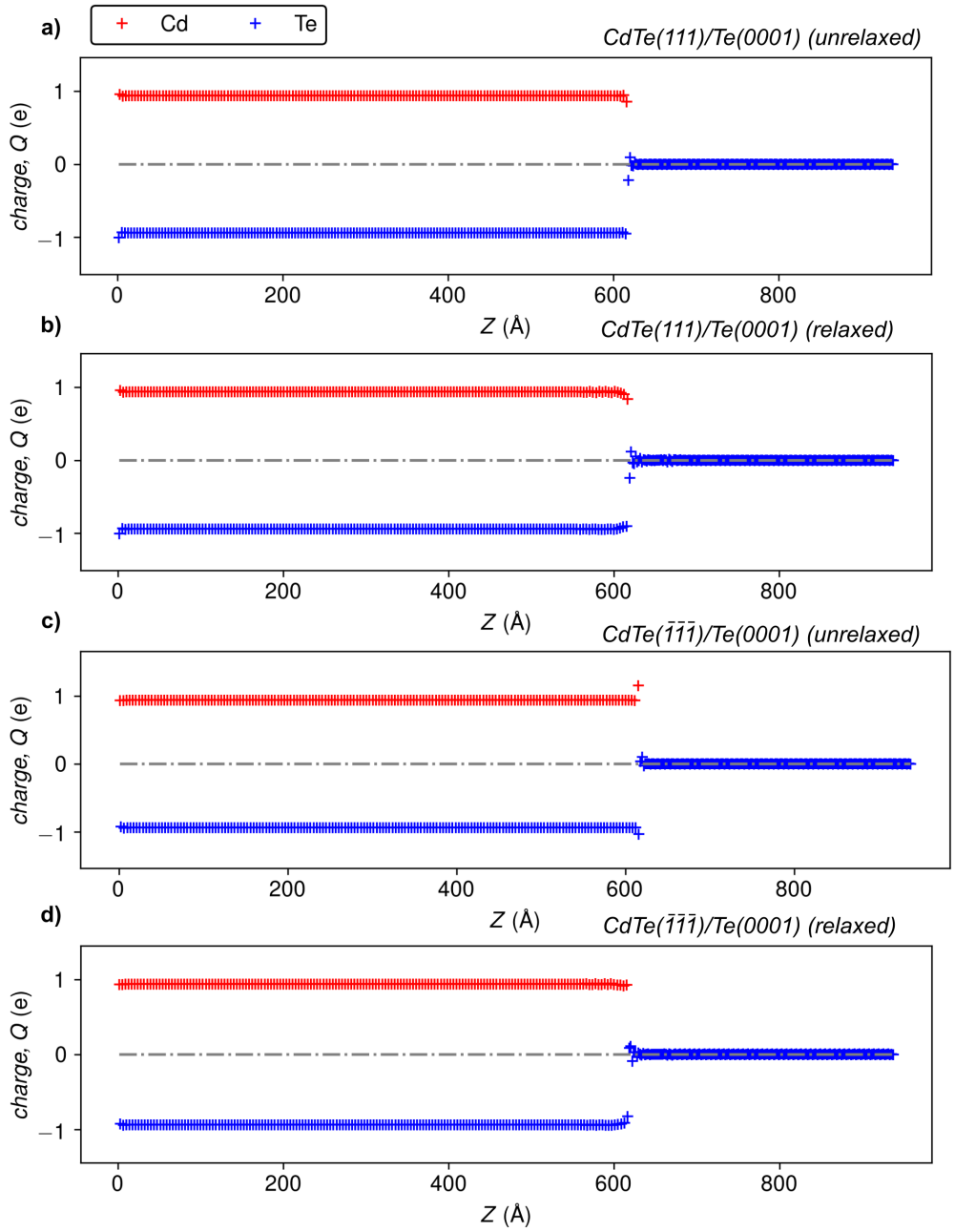

Figure 4.5: Mulliken charge analysis evaluated throughout the (a,c) unrelaxed and (b,d) relaxed versions of the respective CdTe(111)/Te(0001) and CdTe($\bar{1}\bar{1}\bar{1}$)/Te(0001) two-probe interface models. The legend for all plots are found on (a). The centered grey dotted line marks the zero value for Mulliken charge as a reference.

significantly less for the unrelaxed case as opposed to the extended electronic states of the relaxed Te surface. Evaluating the interface states that reside on the Te side of the CdTe{111}/Te(0001) two-probe models in Figure 4.3 and Figure 4.4 lead to the same conclusion. Prior to relaxation,

the Te side of the interface has a small number of interface states. Only after the 5 nm relaxation on the Te side of the interface is when the near-surface Te region develops a continuous band of interface states irrespective of CdTe termination layer. The significant amount of newly formed interface states effectively make the first several nanometers of Te exhibit a metallic-like behavior. According to previous studies using an evaporated Te back contact on CdTe, it was found that Te thicknesses less than 7-8 nanometers display n-type behavior due to a shifted VB energy position [84]. It may be due to the interface states resulting from combined relaxation and interfacial strain effects on the Te overlayer that lead to the change in conductivity type of the back contact. If a thick Te is used, then the strong p-type character is established and more favorable enery band alignments for the CdTe/Te interface are developed, in agreement with other literature studies [122]. Lastly, the Te relaxation effects appear to be independent from the cusp energy potential at the back of the CdTe layer. This reasoning does not mean that the Te layer itself does not contribute to the cusp feature altogether as the unrelaxed CdTe($\bar{1}\bar{1}\bar{1}$)/Te(0001) model still contained a cusp energy potential. The DFT+GF method clearly reflects the complexity involved in band alignment of the CdTe/Te interface that the Anderson Rule cannot address *a priori*.

4.3.4 Band Alignment Dependencies on CdTe Plane Orientation

The last part of the CdTe/Te interface band alignment study was to differentiate between the {111} and (100) CdTe plane orientations for any unique electronic attributes within the relaxed interface region. Figure 4.7 compares the energy band alignment for CdTe(111), CdTe($\bar{1}\bar{1}\bar{1}$) and CdTe(100) planes at the CdTe/Te interface. One major difference is that the cusp energy potential appears only in the CdTe{111} family of planes but not in the CdTe(100) case. Rather, there appears to be a cusp feature that instead resides within the CB for the CdTe(100) case. The DFT+GF two-probe calculations are calculated with a minimal DOS threshold of 10^{-4} eV^{-1}, meaning that any states seen in the plots are not artificial but are real states above the data noise. The small cusp in the CB would be beneficial for mitigating electron minority carrier transport toward the back of the CdTe device. However, there is a significant amount of density of electronic states spreading above

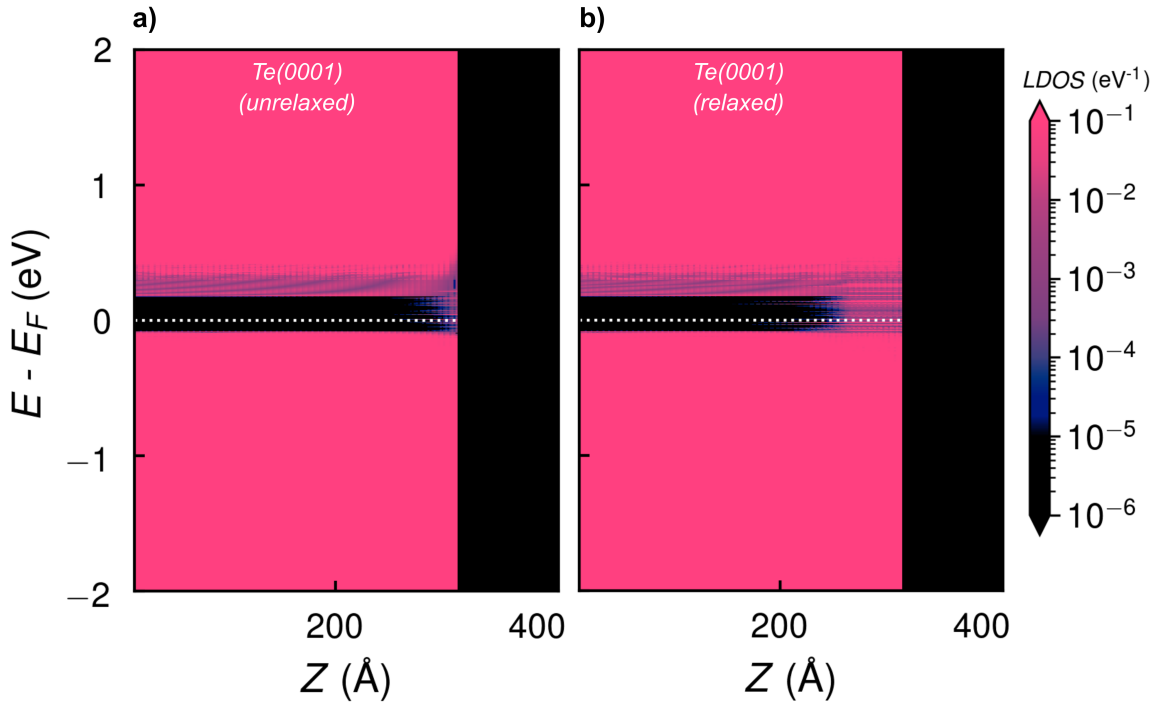

Figure 4.6: One-probe Te(0001) surface energy band alignment for the (a) unrelaxed and (b) relaxed Te surface.

and below the Fermi level E_F in all CdTe/Te cases. In the CdTe(100)/Te(0001) two-probe model, the interface states actually extend further than the CdTe{111}/Te(0001) simulations and have not been fully captured despite the Te length being greater than 10 nm. The deleterious interface states increase due to the bonding arrangement within the interface region of the CdTe(100) plane orientation. The interface electronic states would hinder charge transport at the CdTe absorber layer and Te back contact. It is suggested that features such as the cusp energy potential are responsible for the Te back contact leading to benefits in device performance, which are not necessarily present in the CdTe(100)/Te(0001) interface.

4.4 Summary of Key Findings

The DFT+GF two-probe models for the CdTe/Te interface allow for a systematic evaluation of termination layer and plane orientation effects on the calculated energy band alignments. The following sub-categories provide the key findings from the various studies in the chaper:

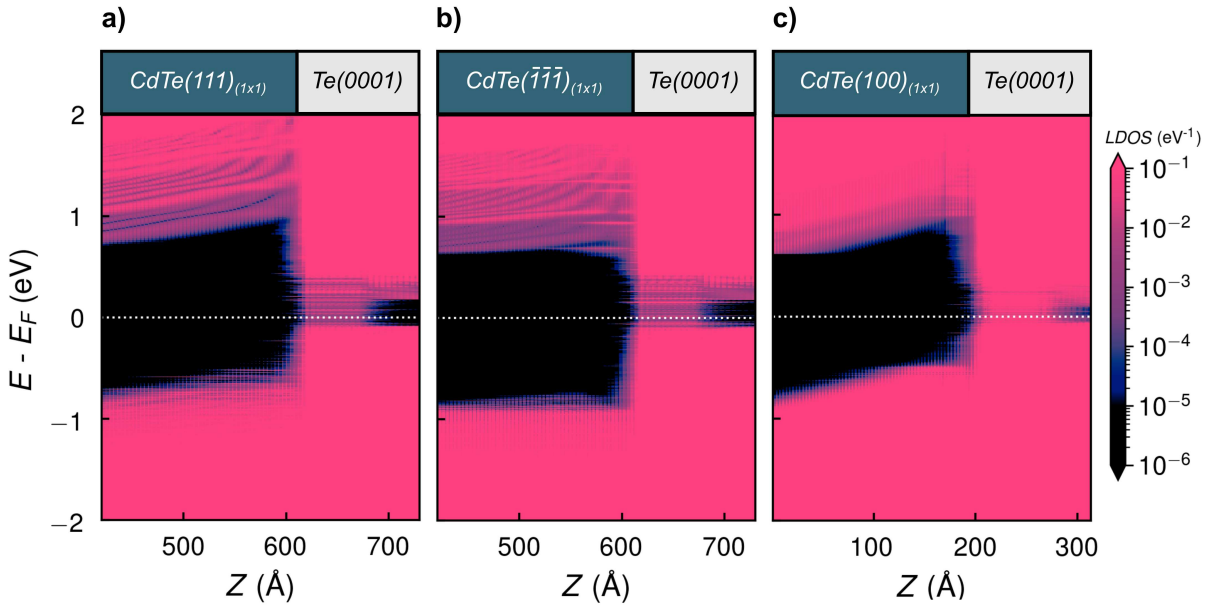

Figure 4.7: Two-probe model comparison of (a) zoomed-in CdTe(111)/Te(0001), (b) zoomed-in CdTe($\bar{1}\bar{1}\bar{1}$)/Te(0001) and (c) CdTe(100)/Te(0001) interface energy band alignments.

CdTe{111}/Te(0001) Interfaces

1. CdTe($\bar{1}\bar{1}\bar{1}$) layer is more energetically stable than the CdTe(111) layer during the formation of a relaxed interface with a Te back contact layer.

2. Unrelaxed and relaxed cases provide band alignment features that are not possible to distinguish within the Anderson Rule.

3. Calculated band offsets are in agreement with experimental results found in literature [34, 126].

4. Cusp energy potentials are present in both CdTe(111) and CdTe($\bar{1}\bar{1}\bar{1}$) facets of the CdTe/Te interface. No indication from Mulliken charge analysis is given that charge transfer between the Cd and Te atoms leads to the cusp feature. The cusp feature primarily develops due to the strain that exists within the CdTe region near the interface due to geometry optimization. The cusp is expected to contribute to enhanced hole transport by means of a tunneling effect to the Te back contact.

Surface vs. Interface-Derived Te(0001) Energy Band Alignments

1. Presence of electronic states in both the Te surface (one-probe) and CdTe/Te interface (two-probe model) calculations.

2. Extension of electronic states at the Te surface and Te side of the interface both caused strictly by relaxation effects.

3. Te thickness lower than 7-8 nanometers undergoes a change in conductivity type due to spatially-dependent electronic states.

CdTe{111}/Te(0001) vs. CdTe(100)/Te(0001) Interfaces

1. No discernable cusp feature present in the CdTe(100)/Te(0001) two-probe modeling case.

2. Greatest improvement to CdTe device performance expected to be cusp formation along the CdTe{111} side for tunneling effect to the Te back contact.

In conclusion, the spatially-dependent energy band alignment constructed by an atomistic modeling approach can accurately determine the complex features seen experimentally in CdTe surfaces and CdTe/Te interfaces. The DFT+GF computational method predicts various electronic attributes that give key insights into the possible mechanisms either enhancing or hindering CdTe PV device performance. DFT+GF one and two-probe models address the increasing importantly electronic phenomena residing at the surfaces and interfaces in semiconductor and PV technologies, which common theoretical models like the Anderson Rule cannot address.

Chapter 5

Conclusions/Proposed Future Work

Significant progress has been made since the inception of the current research work using DFT coupled with Green's function as a computational approach to calculate spatially-dependent energy band alignments for CdTe-based surfaces and interfaces. High-fidelity simulation tools based on first-principles are essential to understanding the fundamental concepts involved in the electronic structure of CdTe PV technologies. It must be stressed that atomistic modeling within the CdTe PV research community is under-utilized for studying interfacial properties where the most performance losses occur in CdTe PV devices [22]. As the device is often dictated by the interface [119], a huge committment is required to explore quantum mechanical-based characteristics in CdTe solar cell interface regions. The research work presented here, if anything, shows the possibility of examining some of the most problematic areas in CdTe PV with the intention of gently pushing the CdTe PV research field in a direction where the importance of CdTe interfacial analysis based on first-principles is recognized. As a result, all computational modeling efforts of CdTe PV surfaces and interfaces have culminated into the following high-level summary of results.

5.1 Summary of Results

The following section provides a high-level synopsis of the key findings in the various simulation models of the current research work.

5.1.1 Bulk Modeling of CdTe Semiconductor Crystal

The simple bulk electrode geometries needed to be converged in terms of structural and electronic properties prior to studying more difficult modeling domains. The overall summary for the DFT computational results while performing CdTe (and Te) bulk calculations is as provided below:

1. An extensive background and literary review of DFT concepts and applications to the CdTe semiconducting II-VI compound has been done in preparation for answering the motivating questions brought out in Section 1.3 of the dissertation.

2. The CdTe bulk structural and electronic properties using different XC functionals and additional parameters in the QuantumATK software have been thoroughly analyzed. An established set of parameters used to achieve the correct band gap values for CdTe-based materials has been found using the LDA-PZ XC functional along with the Hubbard-U correction.

3. The bulk electrode parameters agree with a number of experimental measurements [34, 77, 84] with an emphasis on electronic properties such as CdTe and Te band gap. The parameter were deemed appropriate to maintain transferability while moving toward more complex DFT modeling domains such as the one and two-probe modeling frameworks.

5.1.2 One-Probe Modeling of CdTe Surfaces

Atomic-scale modeling of the CdTe surface based on DFT+GF in the one-probe modeling framework was performed on a combination of plane orientations, terminated surfaces, surface relaxations and reconstructions to investigate the effects of certain CdTe surfaces during possible changes in the CdTe device fabrication process. The follow results were obtained for CdTe surfaces:

1. The underlying concepts associated with surface polarity and surface theory were clearly observed in the calculated results and provide further insights on mechanisms contributing to energy band alignment for CdTe surfaces.

2. A new key insight of cusp energy potentials due to strain from the relaxtion of the CdTe surface is gained with the cusp primarily developing for the CdTe{111} unreconstructed surfaces.

3. Formation layers such as Cl_{Te} and TeO_2 have shown useful yet complex explanations for how higher concentrations of Cl_{Te} eliminate Te dangling bonds, TeO_2 controls band bending

effects, and the combination of both leading to higher cusp energy potentials than the original CdTe(111) surface.

5.1.3 Two-Probe Modeling of CdTe/Te Interface

The atomistic modeling approach to studying the CdTe/Te interface has been accomplished for various conditions and parameters to evaluate what mechanisms are responsible for the resulting band alignment. A summary of the two-probe modeling results to date are provided below:

1. All models have generally constructed an energy band alignment for the CdTe/Te interface as a Type I heterojunction, which is the same type derived by the Anderson Rule. Yet the DFT+GF results provide intricate details on an atomic scale that the Anderson Rule neglects during the band diagram formation process.

2. The band offset measurements were in good agreement with outside characterization studies on experimental CdTe/Te energy band alignments [34, 84, 126, 130].

3. A qualitative assessment of interface states residing on the Te-side of the CdTe/Te interface proves that their extension across the Te band gap is commensurate to the GO region applied to the Te layer. The inversion of the CdTe layer experienced when a thinner Te layer is used [84] could possibly be due to the heavily concentrated defect states on the Te-side of the interface.

4. The development of a GO-dependent cusp region has been verified by other experimental research studies on the CdTe/Te heterojunction [34, 126] and is believed to contribute to improved hole carrier transport at the back of CdTe devices.

5. The CdTe plane orientation dictates whether the cusp energy potential will form or not, highlighting the importance of CdTe surface polarity in the CdTe/Te energy band alignment. Both the Cd and Te-terminated CdTe layers within the CdTe/Te interface have shown the presence of the cusp energy potential.

5.2 Verification of Hypotheses

After consideration of all key findings, validation statements have been made for the four original hypotheses developed in Chapter 1. The following statements address the verification of the formulated hypotheses:

Hypothesis 1: The CdTe{111} and {100} plane orientations will exhibit similar energy band alignment profiles as they both terminate along a plane of the same atomic species (either Cd or Te).

Verification of Hypothesis 1: The CdTe{111} and CdTe{100} facets do exhibit similar surface energy band alignments that are primarily dictated by the termination layer. The conclusion obtained from all surface energy band alignment results is supported by surface polarity and surface theory. However, the surface potential magnitudes for each plane orientation differ according to the surface charging effect. Thus, the polar CdTe{111} surfaces tend to create larger band bending effects than the {100} surfaces.

Hypothesis 2: The Cd-terminated CdTe surface will not have detrimental surface states present at the surface but will cause the bands to bend downward according to surface theory. On the other hand, Te is known to have dangling bonds, so atomistic modeling is expected to reflect the same features by creating several surface electronic states at the surface while bending the bands upward.

Verification of Hypothesis 2: The hypothesis is partially true in that the termination layer determines the band bending direction, the Cd-termination bending downward and the Te-termination bending upward. Yet, several noticeable surface states were present even after relaxation of the Cd-terminated surfaces. Evidently, empty dangling bonds from the cation (Cd) termination also lead to detrimental states, as do the filled dangling bonds from the anion (Te) termination layer. Furthermore, surface reconstruction provides a deeper understanding of how charge neutrality at the CdTe surface improves energy band alignment in comparison to the unreconstructed cases. Stable surface reconstruction for both Cd and Te-terminated CdTe surfaces resulted nearly free surface

electronic states, which can only be explained by the reconstructions satisfying the Electron Counting Rule.

Hypothesis 3: Chlorine is predicted to passivate the Te surface states due to its lower valency than Te. The density of states within the band gap near the surface are expected to be reduced in proportion to the amount of chlorine concentration present at the CdTe surface. A native tellurium dioxide layer is anticipated to further reduce the surface states in combination with chlorine.

Verification of Hypothesis 3: The hypothesis is validated for the DFT+GF surface modeling results that only include varied Cl_{Te} concentrations. Lower concentrations of Cl ($\sim$25%) for CdTe($\bar{1}\bar{1}\bar{1}$) surfaces eliminate some of the deleterious surface states present. Higher Cl concentrations ($\sim$50%) will significantly reduce surface states while removing the band bending features initially seen in the lower or no Cl_{Te} cases. However, the refuted part of the hypothesis is that the TeO_2 monolayer formation (with Te and O atoms strictly arranged in a conceptualized manner interpreted from outside literature [113, 115]) on the CdTe(111) surface does not further reduce surface states in combination with 50% or less Cl concentration. The energy band alignment after the inclusion of both TeO_2 + Cl_{Te} simply adopts the electronic features displayed by the original CdTe(111) surface with a higher cusp energy potential magnitude.

Hypothesis 4: The energy band alignment constructed from an atomistic modeling approach for the unrelaxed and relaxed CdTe/Te interfaces will adopt similar band bending and defect state features as calculated for the individual CdTe and Te surfaces. The interface region will simply be a superposition of the original unrelaxed/relaxed CdTe and Te surfaces with any additional charging effects that depends on termination layer (Cd or Te).

Verification of Hypothesis 4: The hypothesis is refuted within the DFT+GF two-probe model of the CdTe/Te interface although some of the electronic features obtained from surface models can translated to the interface simulations. The Cd-terminated CdTe surfaces adopted a downward band bending characteristic that for the CdTe/Te interface was no longer present. Instead, the CdTe(111)/Te(0001) interface exhibited an upward band bending on the CdTe side. For the Te-

terminated case, the large surface band bending magnitude determined from the CdTe($\bar{1}\bar{1}\bar{1}$) surface model was non-existent in the CdTe($\bar{1}\bar{1}\bar{1}$)/Te(0001) interface model apart from the cusp energy potential formation. One feature that was retained in both the surface and interface models was the cusp energy potential, irrespective of CdTe termination layer. Although the height of the cusp energy potential is experimentally unknown, other literature suggests that such a feature exists and contributes to a tunneling mechanism for hole majority carriers to the back of the CdTe PV device. The other electronic feature that remained independent of model type was the interface states residing on the Te back contact side of the model. In both the Te surface and CdTe/Te interface-derived energy band alignments, a high density of electronic states was clearly visible throughout the near-surface Te band gap and resembled a metallic-like continuity band. As long as the Te layer is above 7-8 nanometers, the back contact aids in the efficiency gains seen from the experimental J-V curve in Figure 4.1b for a typical CdTe PV device. In any case, a two-probe modeling approach to studying heterojunctions is necessary to accommodate all interfacial characteristics rather than simply superposing two one-probe surface models together.

5.3 Beyond the Current Research

The summary of results on CdTe-based surfaces and interfaces validate the efficacy of constructing energy band alignments using atomistic modeling. It is evident that the DFT+GF approach is suitable for non-uniform electronic structures throughout the surface and interface domains with high-fidelity performance in comparison to common theoretical models such as the Anderson Rule. The current research work is expected to make significant advancement to the understanding and procedural construction of energy band alignments in CdTe-based PV technologies that incorporate complex aspects related to geometry optimized regions, interfacial defects, terminated surfaces and plane orientations. However, further action needs to be taken that involves a synergistic method between computation, fabrication and characterization that efficiently translates to optimized CdTe PV device configurations. Thus, a brief discussion is presented as a general framework for achieving a research paradigm based on atomistic modeling.

The strategic framework for developing CdTe PV devices from an quantum mechanical understanding using DFT+GF simulations is laid out in five subsequent processing tasks that are described as follows: 1) use Monte Carlo (molecular dynamics, MD) simulations that initially predict deposition process conditions of materials at optimized control parameters; 2) implement quantum mechanical computational schemes that effectively describe electronic properties throughout the interface regions of the device architectures; 3) analyze simulated interface properties using data extraction algorithms that will then be used in numerical device modeling efforts for studying device performance; 4) verify the accuracy of simulation results by constructing device architectures in experimental apparatus and later characterizing their properties; 5) develop a database containing all optimized results for understanding the fundamental science associated with novel material architectures used in next generation technologies.

The first step consists of predicting the CdTe-based thin film layer deposition process by utilization of molecular dynamical simulations. Optimized control parameters in deposition processes are crucial for obtaining desirable interfacial characteristics in device technologies. However, the amount of time, financial, and material resources dedicated to optimizing the fabrication process prevents the user from exploring novel materials within various deposition regimes. MD offers the advantage of evaluating time and temperature dependent atomistic interactions that are involved in the growth behaviors of materials. The predicted structural characteristics of the atomic species calculated by MD simulations will be fed into the more sophisticated DFT+GF computational tool to accurately describe the electronic structures of materials and the interfaces between them. As a result, the coupling of computational methods can be systematically evaluated at various conditions that provide a deeper understanding of CdTe PV device properties while maintaining accuracy throughout the process.

The second procedure incorporates quantum mechanical computations of the atomistic models to understand the structural and electronic properties of materials from first principles. It is essential that an atomistic perspective be investigated in materials and devices as the key details gained from *ab initio* methods are directly related to device performance. DFT coupled with Green's

function as used in this work would be implemented to evaluate either the surface or interfacial characteristics that contribute to charge carrier transport.

An algorithmic data extraction procedure would be utilized for further analysis of the DFT+GF results. The efforts associated with the algorithm are primarily focused on obtaining the salient electronic properties of the interface and integrating them to numerical device models. The seamless transition between atomistic to continuum-based modeling bridged by the algorithmic process would provide key insights on the mechanisms influencing device performance.

Experimental verification of the device architectures should be acquired and compared to the device performance predicted by the previous four steps in the simulation framework. A physical instrumentation tool is necessary to validate the simulation results while being designed in a way that is versatile for multiple device configurations and materials. At the same time, characterization of the thin films is necessary to verify whether the predicted electronic structures are seen within CdTe-based PV technologies. Evaluations of the CdTe-based thin film in a comparative manner can be done by a number of characterization techniques to determine the surface and/or interface-dependent properties of the CdTe material [131].

The final step consists of optimizing the current device architectures in an iterative feedback loop and developing a database for them. The novel materials and devices database would include all quantified parameters within the simulation and deposition procedures that would be accessible to the entire science community. The steps beyond the current research work are expected to synergistically develop a quantum-enabled scientific understanding of materials that seamlessly translates into next generation CdTe PV technologies.

Bibliography

[1] SolarPower Europe, "Global Market Outlook 2019-2023." [Online]. Available: https://www.solarpowereurope.org/global-market-outlook-2019-2023/. Accessed: 2020-04-07.

[2] BloombergNEF, "Clean Energy Investment Exceeded $300 Billion Once Again in 2018." [Online]. Available: https://about.bnef.com/blog/clean-energy-investment-exceeded-300-billion-2018/. Accessed: 2019-08-09.

[3] Lazard, "Lazard's Levelized Cost of Energy Analysis - Version 11.0, November 2017." [Online]. Available: https://www.lazard.com/media/450337/lazard-levelized-cost-of-energy-version-110.pdf. Accessed: 2019-08-12.

[4] N. M. Haegel, H. Atwater, T. Barnes, C. Breyer, A. Burrell, Y.-M. Chiang, S. De Wolf, B. Dimmler, D. Feldman, S. Glunz, J. C. Goldschmidt, D. Hochschild, R. Inzunza, I. Kaizuka, B. Kroposki, S. Kurtz, S. Leu, R. Margolis, K. Matsubara, A. Metz, W. K. Metzger, M. Morjaria, S. Niki, S. Nowak, I. M. Peters, S. Philipps, T. Reindl, A. Richter, D. Rose, K. Sakurai, R. Schlatmann, M. Shikano, W. Sinke, R. Sinton, B. Stanbery, M. Topic, W. Tumas, Y. Ueda, J. van de Lagemaat, P. Verlinden, M. Vetter, E. Warren, M. Werner, M. Yamaguchi, and A. W. Bett, "Terawatt-scale photovoltaics: Transform global energy," *Science*, vol. 364, no. 6443, pp. 836–838, 2019.

[5] Forecast International, "Renewable Energy." [Online]. Available: http://fi-powerweb.com/Renewable-Energy.html. Accessed: 2020-04-07.

[6] V. Fthenakis and M. Raugei, "7 - Environmental life-cycle assessment of photovoltaic systems," in *The Performance of Photovoltaic (PV) Systems* (N. Pearsall, ed.), pp. 209–232, Woodhead Publishing, 2017.

[7] R. Wiser, D. Millstein, T. Mai, J. Macknick, A. Carpenter, S. Cohen, W. Cole, B. Frew, and G. Heath, "The environmental and public health benefits of achieving high penetrations of solar energy in the united states," *Energy*, vol. 113, pp. 472 – 486, 2016.

[8] A. H. Munshi, N. Sasidharan, S. Pinkayan, K. L. Barth, W. Sampath, and W. Ongsakul, "Thin-film CdTe photovoltaics – The technology for utility scale sustainable energy generation," *Sol. Energy*, vol. 173, pp. 511 – 516, 2018.

[9] Fraunhofer ISE, "Photovoltaics Report." [Online]. Available: https://www.ise.fraunhofer.de/content/dam/ise/de/documents/publications/studies/Photovoltaics-Report.pdf. Updated: 2019-11-14, Accessed: 2020-04-07.

[10] First Solar, "First Solar Sustainability Report 2018." [Online]. Available: www.firstsolar.com/-/media/First-Solar/Sustainability-Documents/FirstSolar_SustainabilityReport_Web_2018.ashx. Accessed: 2019-08-07.

[11] R. Rawat, S. Kaushik, O. Sastry, B. Bora, and Y. Singh, "Long-term Performance Analysis of CdTe PV module in real operating conditions," *Materials Today: Proceedings*, vol. 5, no. 11, Part 2, pp. 23210–23217, 2018. International Conference on Advances in Energy Research 2015 (ICAER-2015).

[12] M. Sorgato, K. Schneider, and R. Rüther, "Technical and economic evaluation of thin-film CdTe building-integrated photovoltaics (BIPV) replacing façade and rooftop materials in office buildings in a warm and sunny climate," *Renew. Energ.*, vol. 118, pp. 84 – 98, 2018.

[13] B. M. Başol and B. McCandless, "Brief review of cadmium telluride-based photovoltaic technologies," *J. Photonics Energy*, vol. 4, no. 1, pp. 1 – 11 – 11, 2014.

[14] M. M. Al-Jassim, F. S. Hasoon, K. M. Jones, B. M. Keyes, R. J. Matson, and H. R. Moutinho, "The morphology, microstructure and luminescent properties of CdS/CdTe thin film solar cells," in *Conference Record of the Twenty Third IEEE Photovoltaic Specialists Conference - 1993 (Cat. No.93CH3283-9)*, pp. 459–465, 1993.

[15] P. Paulson and V. Dutta, "Study of in situ $CdCl_2$ treatment on CSS deposited CdTe films and CdS/CdTe solar cells," *Thin Solid Films*, vol. 370, no. 1, pp. 299–306, 2000.

[16] H. R. Moutinho, R. G. Dhere, M. J. Romero, C.-S. Jiang, B. To, and M. M. Al-Jassim, "Electron backscatter diffraction of CdTe thin films: Effects of CdCl2 treatment," *J. Vac. Sci. Technol. A*, vol. 26, no. 4, pp. 1068–1073, 2008.

[17] O. Zywitzki, T. Modes, H. Morgner, C. Metzner, B. Siepchen, B. Späth, C. Drost, V. Krishnakumar, and S. Frauenstein, "Effect of chlorine activation treatment on electron beam induced current signal distribution of cadmium telluride thin film solar cells," *J. Appl. Phys.*, vol. 114, no. 16, p. 163518, 2013.

[18] J. Kephart, J. McCamy, Z. Ma, A. Ganjoo, F. Alamgir, and W. Sampath, "Band alignment of front contact layers for high-efficiency CdTe solar cells," *Sol. Energy Mater Sol. Cells*, vol. 157, pp. 266–275, 2016.

[19] A. H. Munshi, J. M. Kephart, A. Abbas, T. M. Shimpi, K. L. Barth, J. M. Walls, and W. S. Sampath, "Polycrystalline CdTe photovoltaics with efficiency over 18% through improved absorber passivation and current collection," *Sol. Energy Mater. Sol. Cells*, vol. 176, pp. 9–18, 2018.

[20] National Renewable Energy Laboratory, "Best Research-Cell Efficiency Chart." [Online]. Available: https://www.nrel.gov/pv/cell-efficiency.html. Accessed: 2019-08-07.

[21] W. Shockley and H. J. Queisser, "Detailed Balance Limit of Efficiency of *p-n* Junction Solar Cells," *J. Appl. Phys.*, vol. 32, no. 3, pp. 510–519, 1961.

[22] US-DOE Office of Energy Efficiency & Renewable Energy, "Photovoltaics Innovation Roadmap Request for Information Summary." [Online]. Available: https://www.energy.gov/sites/prod/files/2018/03/f49/PV\%20Innovation\%20Roadmap\%20RFI\%20Summary.pdf. Accessed: 2019-08-07.

[23] A. H. Munshi, J. Kephart, A. Abbas, J. Raguse, J. Beaudry, K. Barth, J. Sites, J. Walls, and W. Sampath, "Polycrystalline CdSeTe/CdTe Absorber Cells With 28 mA/cm^2 Short-Circuit Current," *IEEE J. Photovolt.*, vol. 8, no. 1, pp. 310–314, 2018.

[24] A. H. Munshi, A. H. Danielson, K. L. Barth, G. Gélinas, J. Beaudry, and W. S. Sampath, "Advanced Co-sublimation of Low Bandgap $CdSe_xTe_{1-x}$ Alloy to Achieve Higher Short-Circuit Current," in *2018 IEEE 7th World Conference on Photovoltaic Energy Conversion (WCPEC) (A Joint Conference of 45th IEEE PVSC, 28th PVSEC 34th EU PVSEC)*, pp. 0148–0152, Jun 2018.

[25] W. K. Metzger, S. Grover, D. Lu, E. Colegrove, J. Moseley, C. L. Perkins, X. Li, R. Mallick, W. Zhang, R. Malik, J. Kephart, C.-S. Jiang, D. Kuciauskas, D. S. Albin, M. M. Al-Jassim, G. Xiong, and M. Gloeckler, "Exceeding 20% efficiency with in situ group V doping in polycrystalline CdTe solar cells," *Nat. Energy*, vol. 4, pp. 837–845, 2019.

[26] S. Farrell, T. Barnes, W. K. Metzger, J. H. Park, R. Kodama, and S. Sivananthan, "*In Situ* Arsenic Doping of CdTe/Si by Molecular Beam Epitaxy," *J. Electron. Mater.*, vol. 44, no. 9, pp. 3202–3206, 2015.

[27] A. Kanevce, M. Reese, T. Barnes, S. Jensen, and W. Metzger, "The roles of carrier concentration and interface, bulk, and grain-boundary recombination for 25% efficient CdTe solar cells," *J. Appl. Phys.*, vol. 121, p. 214506, Jun 2017.

[28] D. Neamen, *Semiconductor physics and devices : basic principles*. New York, NY: McGraw-Hill, 2012.

[29] E. T.-W. Yu, *Physics and applications of semiconductor heterostructures : I. Measurement of band offsets in semiconductor heterojunctions. II. Theoretical and experimental studies of tunneling in semiconductor heterostructure devices*. PhD thesis, California Institute of Technology, Apr 1991.

[30] R. L. Anderson, "Experiments on Ge-GaAs heterojunctions," *Solid State Electron.*, vol. 5, no. 5, pp. 341–351, 1962.

[31] G. Margaritondo, *Electronic structure of semiconductor heterojunctions*. Milano Italy Dordrecht Boston: Jaca Book Kluwer Academic, 1988.

[32] G. Cook and R. H. Dickerson, "Understanding the chemical potential," *Am. J. Phys.*, vol. 63, no. 8, pp. 737–742, 1995.

[33] R. Scheer and H.-W. Schock, *Chalcogenide Photovoltaics : Physics, Technologies, and Thin Film Devices*. Weinheim Chichester: Wiley-VCH John Wiley distributor, 2011.

[34] J. Fritsche, A. Klein, and W. Jaegermann, "Thin Film Solar Cells: Materials Science at Interfaces," *Adv. Eng. Mater.*, vol. 7, no. 10, pp. 914–920, 2005.

[35] M. Aras and c. Kiliç, "Combined hybrid functional and DFT+U calculations for metal chalcogenides," *J. Chem. Phys.*, vol. 141, no. 4, p. 044106, 2014.

[36] P. Gopal, M. Fornari, S. Curtarolo, L. A. Agapito, L. Liyanage, and M. Buongiorno Nardelli, "Improved predictions of the physical properties of Zn– and Cd–based wide band-gap semiconductors: A validation of the ACBN0 functional," *Phys. Rev. B*, vol. 91, May 2015.

[37] Y. Wu, G. Chen, Y. Zhu, W.-J. Yin, Y. Yan, M. Al-Jassim, and S. J. Pennycook, "LDA+U/GGA+U calculations of structural and electronic properties of CdTe: Dependence on the effective U parameter," *Comput. Mater. Sci.*, vol. 98, pp. 18 – 23, 2015.

[38] S.-H. Wei and S. B. Zhang, "Chemical trends of defect formation and doping limit in II–VI semiconductors: The case of CdTe," *Phys. Rev. B*, vol. 66, p. 155211, Oct 2002.

[39] C. Feng, W.-J. Yin, J. Nie, X. Zu, M. N. Huda, S.-H. Wei, M. M. Al-Jassim, and Y. Yan, "Possible effects of oxygen in Te-rich $\Sigma 3$ (112) grain boundaries in CdTe," *Solid State Commun.*, vol. 152, no. 18, pp. 1744 – 1747, 2012.

[40] J. Ma, D. Kuciauskas, D. Albin, R. Bhattacharya, M. Reese, T. Barnes, J. V. Li, T. Gessert, and S.-H. Wei, "Dependence of the Minority–Carrier Lifetime on the Stoichiometry of CdTe Using Time-Resolved Photoluminescence and First-Principles Calculations," *Phys. Rev. Lett.*, vol. 111, p. 067402, Aug 2013.

[41] C. Buurma, *Application of ab-initio Methods to Grain Boundaries and Point Defects for Poly-CdTe Solar Cells*. PhD thesis, University of Illinois at Chicago, Jan 2015.

[42] M. A. Flores, W. Orellana, and E. Menéndez-Proupin, "First-principles DFT+GW study of the Te antisite in CdTe," *Comp. Mater. Sci.*, vol. 125, pp. 176 – 182, 2016.

[43] D. Krasikov and I. Sankin, "Defect interactions and the role of complexes in the CdTe solar cell absorber," *J. Mater. Chem. A*, vol. 5, pp. 3503–3513, 2017.

[44] W. Orellana, E. Menéndez-Proupin, and M. A. Flores, "Self-compensation in chlorine-doped CdTe," *Sci. Rep.*, vol. 9, p. 9194, Jun 2019.

[45] S. Gundel, A. Fleszar, W. Faschinger, and W. Hanke, "Atomic and electronic structure of the CdTe(001) surface: LDA and GW calculations," *Phys. Rev. B*, vol. 59, pp. 15261–15269, Jun 1999.

[46] B. Rerbal, G. Merad, H. Mariette, H. Faraoun, and J.-M. Raulot, "Ab initio investigation of the CdTe (001) surface," *Superlattices Microstruct.*, vol. 46, no. 5, pp. 733–744, 2009.

[47] J. Li, N. Kioussis, F. Aqariden, and C. Grein, "Thermodynamic and stoichiometric stability of the Cd-terminated CdTe (111) surface," *Phys. Rev. B*, vol. 85, p. 235306, Jun 2012.

[48] J. Li, J. Gayles, N. Kioussis, Z. Zhang, C. Grein, and F. Aqariden, "Ab Initio Studies of the Unreconstructed CdTe (111) Surface," *J. Electron. Mater.*, vol. 41, pp. 2745–2753, 2012.

[49] E. Naderi, S. Nanavati, C. Majumder, and S. V. Ghaisas, "Diffusion of Cd and Te adatoms on CdTe(111) surfaces: A computational study using density functional theory," *AIP Advances*, vol. 5, no. 1, p. 017134, 2015.

[50] K. Meinander and J. S. Preston, "A DFT study on the effect of surface termination in CdTe (111)/α-Al_2O_3 (0001) heteroepitaxy," *Surf. Sci.*, vol. 632, pp. 93–97, 2015.

[51] D. Odkhuu, M.-s. Miao, F. Aqariden, C. Grein, and N. Kioussis, "Atomic and electronic structure of CdTe/metal (Cu, Al, Pt) interfaces and their influence to the Schottky barrier," *J. Appl. Phys.*, vol. 120, no. 18, p. 185703, 2016.

[52] M. Ribeiro, L. R. C. Fonseca, T. Sadowski, and R. Ramprasad, "Ab initio calculation of the CdSe/CdTe heterojunction band offset using the local-density approximation-1/2 technique with spin-orbit corrections," *J. Appl. Phys.*, vol. 111, no. 7, p. 073708, 2012.

[53] A. Cao, T. Tan, H. Zhang, Y. Du, Y. Sun, and G. Zha, "Electronic structures and optical properties of the CdTe/CdS heterojunction interface from the first-principles calculations," *Physica B: Condens. Matter*, vol. 545, pp. 323 – 329, 2018.

[54] S. Smidstrup, T. Markussen, P. Vancraeyveld, J. Wellendorff, J. Schneider, T. Gunst, B. Verstichel, D. Stradi, P. A. Khomyakov, U. G. Vej-Hansen, M.-E. Lee, S. T. Chill, F. Rasmussen, G. Penazzi, F. Corsetti, A. Ojanperä, K. Jensen, M. L. N. Palsgaard, U. Martinez, A. Blom, M. Brandbyge, and K. Stokbro, "QuantumATK: An integrated platform of electronic and atomic-scale modelling tools," *J. Phys. Condens. Matter*, vol. 32, p. 015901, Oct 2019.

[55] A. Crovetto, M. L. N. Palsgaard, T. Gunst, T. Markussen, K. Stokbro, M. Brandbyge, and O. Hansen, "Interface band gap narrowing behind open circuit voltage losses in Cu_2ZnSnS_4 solar cells," *Appl. Phys. Lett.*, vol. 110, no. 8, p. 083903, 2017.

[56] J. Anderson, P. J. Burns, D. Milroy, P. Ruprecht, T. Hauser, and H. J. Siegel, "Deploying RMACC Summit: An HPC Resource for the Rocky Mountain Region," in *Proceedings of the Practice and Experience in Advanced Research Computing 2017 on Sustainability, Success and Impact*, PEARC17, (New York, NY, USA), pp. 8:1–8:7, ACM, 2017.

[57] M. C. Payne, M. P. Teter, D. C. Allan, T. A. Arias, and J. D. Joannopoulos, "Iterative minimization techniques for ab initio total-energy calculations: molecular dynamics and conjugate gradients," *Rev. Mod. Phys.*, vol. 64, pp. 1045–1097, Oct 1992.

[58] F. Giustino, *Materials modelling using density functional theory : properties and predictions*. Oxford: Oxford University Press, 2014.

[59] J. Junquera, O. Paz, D. Sánchez-Portal, and E. Artacho, "Numerical atomic orbitals for linear-scaling calculations," *Phys. Rev. B*, vol. 64, p. 235111, Nov 2001.

[60] K. Stokbro, M. Engelund, and A. Blom, "Atomic-scale model for the contact resistance of the nickel-graphene interface," *Phys. Rev. B*, vol. 85, p. 165442, Apr 2012.

[61] D. Stradi, U. Martinez, A. Blom, M. Brandbyge, and K. Stokbro, "General atomistic approach for modeling metal-semiconductor interfaces using density functional theory and nonequilibrium Green's function," *Phys. Rev. B*, vol. 93, p. 155302, Apr 2016.

[62] S. Smidstrup, D. Stradi, J. Wellendorff, P. A. Khomyakov, U. G. Vej-Hansen, M.-E. Lee, T. Ghosh, E. Jónsson, H. Jónsson, and K. Stokbro, "First–principles Green's-function method for surface calculations: A pseudopotential localized basis set approach," *Phys. Rev. B*, vol. 96, p. 195309, Nov 2017.

[63] M. Palsgaard, *Bridging first principles modelling with nanodevice TCAD simulations*. PhD thesis, Technical University of Denmark, Aug 2018.

[64] M. Brandbyge, J.-L. Mozos, P. Ordejón, J. Taylor, and K. Stokbro, "Density-functional method for nonequilibrium electron transport," *Phys. Rev. B*, vol. 65, p. 165401, Mar 2002.

[65] E. Artacho, E. Anglada, O. Diéguez, J. D. Gale, A. García, J. Junquera, R. M. Martin, P. Ordejón, J. M. Pruneda, D. Sánchez-Portal, and J. M. Soler, "The SIESTA method; developments and applicability," *J. Phys. Condens. Matter*, vol. 20, p. 064208, Jan 2008.

[66] QuantumATK P-2019.03, Synopsys QuantumATK.

[67] T. Ozaki, "Variationally optimized atomic orbitals for large-scale electronic structures," *Phys. Rev. B*, vol. 67, p. 155108, Apr 2003.

[68] T. Ozaki and H. Kino, "Numerical atomic basis orbitals from H to Kr," *Phys. Rev. B*, vol. 69, p. 195113, May 2004.

[69] M. Schlipf and F. Gygi, "Optimization algorithm for the generation of ONCV pseudopotentials," *Comput. Phys. Commun.*, vol. 196, pp. 36 – 44, 2015.

[70] G. Grosso and G. P. Parravicini, "Chapter 4 - The One-Electron Approximation and Beyond," in *Solid State Physics (Second Edition)* (G. Grosso and G. P. Parravicini, eds.), pp. 135–177, Amsterdam: Academic Press, second edition ed., 2014.

[71] J. P. Perdew and A. Zunger, "Self-interaction correction to density-functional approximations for many-electron systems," *Phys. Rev. B*, vol. 23, pp. 5048–5079, May 1981.

[72] M. Cococcioni, "The LDA+U Approach: A Simple Hubbard Correction for Correlated Ground States," in *Correlated electrons: from models to materials*, vol. 2, ch. 8, pp. 4–40, Jülich: Forschungszentrum Jülich, Zentralbibliothek, Verl, 2012.

[73] S. Lalitha, S. Karazhanov, P. Ravindran, S. Senthilarasu, R. Sathyamoorthy, and J. Janabergenov, "Electronic structure, structural and optical properties of thermally evaporated CdTe thin films," *Physica B Condens. Matter*, vol. 387, no. 1, pp. 227–238, 2007.

[74] J. P. Perdew, K. Burke, and M. Ernzerhof, "Generalized Gradient Approximation Made Simple," *Phys. Rev. Lett.*, vol. 77, pp. 3865–3868, Oct 1996.

[75] I. V. Kurilo, V. P. Alekhin, I. O. Rudyi, S. I. Bulychev, and L. I. Osypyshin, "Mechanical Properties of ZnTe, CdTe, CdHgTe and HgTe Crystals from Micromechanical Investigation," *Phys. Status Solidi A*, vol. 163, no. 1, pp. 47–58, 1997.

[76] E. Deligoz, K. Colakoglu, and Y. Ciftci, "Elastic, electronic, and lattice dynamical properties of CdS, CdSe, and CdTe," *Physica B Condens. Matter*, vol. 373, pp. 124–130, Mar 2006.

[77] V. Manivannan, R. A. Enzenroth, K. L. Barth, S. Kohli, P. R. McCurdy, and W. S. Sampath, "Microstructural features of cadmium telluride photovoltaic thin film devices," *Thin Solid Films*, vol. 516, no. 6, pp. 1209 – 1213, 2008.

[78] H. J. McSkimin and D. G. Thomas, "Elastic Moduli of Cadmium Telluride," *J. Appl. Phys.*, vol. 33, no. 1, pp. 56–59, 1962.

[79] A. Rubio-Ponce, D. Olguín, and I. Hernández-Calderón, "Calculation of the effective masses of II-VI semiconductor compounds," *Superficies y Vacío*, vol. 16, pp. 26–28, Jun 2003.

[80] D. T. F. Marple, "Effective Electron Mass in CdTe," *Phys. Rev.*, vol. 129, pp. 2466–2470, Mar 1963.

[81] A. P. Nicholson, A. H. Munshi, and U. P. W. S. Sampath, "First Principles Approach to CdTe/Te Interface Band Alignment Using Density Functional Theory and Nonequilibrium Green's Function," in *2018 IEEE 7th World Conference on Photovoltaic Energy Conversion (WCPEC) (A Joint Conference of 45th IEEE PVSC, 28th PVSEC 34th EU PVSEC)*, pp. 1932–1936, Jun 2018.

[82] M. Palsgaard, A. Crovetto, T. Gunst, T. Markussen, O. Hansen, K. Stokbro, and M. Brandbyge, "Semiconductor band alignment from first principles: A new nonequilibrium Green's function method applied to the CZTSe/CdS interface for photovoltaics," *International Conference on Simulation of Semiconductor Processes and Devices (SISPAD)*, pp. 377–380, 2016.

[83] C. Persson and S. Mirbt, "Improved Electronic Structure and Optical Properties of sp-Hybridized Semiconductors Using LDA+USIC," *Braz. J. Phys.*, vol. 36, pp. 286–290, Jun 2006.

[84] D. W. Niles, X. Li, P. Sheldon, and H. Höchst, "A photoemission determination of the band diagram of the Te/CdTe interface," *J. Appl. Phys.*, vol. 77, no. 9, pp. 4489–4493, 1995.

[85] J. Ren, L. Fu, G. Bian, M. Wong, T. Wang, G. Zha, W. Jie, T. Miller, M. Z. Hasan, and T.-C. Chiang, "Spectroscopic studies of $\mathrm{CdTe}(111)$ bulk and surface electronic structure," *Phys. Rev. B*, vol. 91, p. 235303, Jun 2015.

[86] C. H. Lee, E. B. Nam, M.-E. Lee, and S. U. Lee, "Unraveling the controversy over a catalytic reaction mechanism using a new theoretical methodology: One probe and non-equilibrium surface Green's function," *Nano Energy*, vol. 63, p. 103863, 2019.

[87] Y. An, Y. Hou, S. Gong, R. Wu, C. Zhao, T. Wang, Z. Jiao, H. Wang, and W. Liu, "Evaluating the exfoliation of two-dimensional materials with a Green's function surface model," *Phys. Rev. B*, vol. 101, p. 075416, Feb 2020.

[88] N. A. Lanzillo, O. D. Restrepo, P. S. Bhosale, E. Cruz-Silva, C.-C. Yang, B. Youp Kim, T. Spooner, T. Standaert, C. Child, G. Bonilla, and K. V. R. M. Murali, "Electron scattering at interfaces in nano-scale vertical interconnects: A combined experimental and ab initio study," *Appl. Phys. Lett.*, vol. 112, no. 16, p. 163107, 2018.

[89] F. Fuchs, S. Gemming, and J. Schuster, "Electron transport through $NiSi_2$-Si contacts and their role in reconfigurable field-effect transistors," *J. Phys. Condens. Matter*, vol. 31, p. 355002, Jun 2019.

[90] R. H. Williams, "Surface defects on semiconductors," *Surf. Sci.*, vol. 132, no. 1, pp. 122–142, 1983.

[91] M. D. Pashley, "Electron counting model and its application to island structures on molecular-beam epitaxy grown GaAs(001) and ZnSe(001)," *Phys. Rev. B*, vol. 40, pp. 10481–10487, Nov 1989.

[92] G. Srivastava, "The electron counting rule and passivation of compound semiconductor surfaces," *Appl. Surf. Sci.*, vol. 252, no. 21, pp. 7600–7607, 2006. Proceedings of the 4th International Workshop on Semiconductor Surface Passivation.

[93] E. P. Warekois, M. C. Lavine, A. N. Mariano, and H. C. Gatos, "Crystallographic Polarity in the II–VI Compounds," *J. Appl. Phys.*, vol. 33, no. 2, pp. 690–696, 1962.

[94] P. F. Fewster and P. A. C. Whiffin, "Crystallographic polarity and etching of cadmium telluride," *J. Appl. Phys.*, vol. 54, no. 8, pp. 4668–4670, 1983.

[95] D. B. Holt, "Surface polarity and symmetry in semiconducting compounds," *J. Mater. Sci.*, vol. 23, pp. 1131–1136, Mar 1988.

[96] P. Brown, K. Durose, G. J. Russell, and J. Woods, "The absolute determination of CdTe crystal polarity," *J. Cryst. Growth*, vol. 101, no. 1, pp. 211 – 215, 1990.

[97] H. C. Gatos and M. C. Lavine, "Characteristics of the $\{111\}$ Surfaces of the III–v Intermetallic Compounds," *J. Electrochem. Soc.*, vol. 107, no. 5, p. 427, 1960.

[98] K. Momma and F. Izumi, "*VESTA3* for three–dimensional visualization of crystal, volumetric and morphology data," *J. Appl. Crystallogr.*, vol. 44, pp. 1272–1276, Dec 2011.

[99] R. T. Tung, "Recent advances in Schottky barrier concepts," *Mat. Sci. Eng. R Rep.*, vol. 35, no. 1, pp. 1 – 138, 2001.

[100] T. Heinzel, *Mesoscopic electronics in solid state nanostructures*. Weinheim Germany: Wiley-VCH, 2007.

[101] W. A. Harrison, "Theory of polar semiconductor surfaces," *J. Vac. Sci. Technol.*, vol. 16, no. 5, pp. 1492–1496, 1979.

[102] M. O. Reese, C. L. Perkins, J. M. Burst, S. Farrell, T. M. Barnes, S. W. Johnston, D. Kuciauskas, T. A. Gessert, and W. K. Metzger, "Intrinsic surface passivation of CdTe," *J. Appl. Phys.*, vol. 118, no. 15, p. 155305, 2015.

[103] A. P. Nicholson, U. Martinez, A. Shah, A. Thiyagarajan, and W. S. Sampath, "Atomistic modeling of energy band alignment in CdTe(100) and CdTe(111) surfaces," *Appl. Surf. Sci.*, vol. 528, p. 146832, 2020.

[104] S. Tatarenko, F. Bassani, J. C. Klein, K. Saminadayar, J. Cibert, and V. H. Etgens, "Surface reconstructions of (001) CdTe and their role in the dynamics of evaporation and molecular-beam epitaxy growth," *J. Vac. Sci. Technol. A*, vol. 12, no. 1, pp. 140–147, 1994.

[105] S. Y. Tong, G. Xu, and W. N. Mei, "Vacancy-Buckling Model for the (2×2) GaAs(111) Surface," *Phys. Rev. Lett.*, vol. 52, pp. 1693–1696, May 1984.

[106] C. K. Egan, Q. Z. Jiang, and A. W. Brinkman, "Morphology and reconstructions of polar CdTe(111)A,B surfaces by scanning tunneling microscopy," *J. Vac. Sci. Technol. A*, vol. 29, no. 1, p. 011021, 2011.

[107] R. Duszak, S. Tatarenko, J. Cibert, K. Saminadayar, and C. Deshayes, "($\bar{1}\bar{1}\bar{1}$) CdTe surface structure: A study by reflection high energy electron diffraction, x-ray photoelectron spectroscopy, and x-ray photoelectron diffraction," *J. Vac. Sci. Technol. A*, vol. 9, no. 6, pp. 3025–3030, 1991.

[108] P. Lu and D. J. Smith, "Direct imaging of CdTe(001) surface reconstructions by high-resolution electron microscopy," *Surf. Sci.*, vol. 254, no. 1, pp. 119–124, 1991.

[109] A. E. Patrakov, R. F. Fink, K. Fink, T. C. Schmidt, and B. Engels, "Density-functional study on the migration of Cd and Te adsorbates on the (001) surface of CdTe," *Phys. Stat. Sol. B*, vol. 247, no. 4, pp. 937–944, 2010.

[110] C. Li, Y. Wu, J. Poplawsky, T. J. Pennycook, N. Paudel, W. Yin, S. J. Haigh, M. P. Oxley, A. R. Lupini, M. Al-Jassim, S. J. Pennycook, and Y. Yan, "Grain-Boundary-Enhanced Carrier Collection in CdTe Solar Cells," *Phys. Rev. Lett.*, vol. 112, p. 156103, Apr 2014.

[111] F. A. Ponce, R. Sinclair, and R. H. Bube, "Native tellurium dioxide layer on cadmium telluride: A high–resolution electron microscopy study," *Appl. Phys. Lett.*, vol. 39, no. 12, pp. 951–953, 1981.

[112] T. L. Chu, S. S. Chu, and S. T. Ang, "Surface passivation and oxidation of cadmium telluride and properties of metal–oxide–CdTe structures," *J. Appl. Phys.*, vol. 58, no. 8, pp. 3206–3210, 1985.

[113] B. Kowalski, B. Orłowski, and J. Ghijsen, "Oxide formation on the CdTe(111)A (1×1) surface," *Appl. Surf. Sci.*, vol. 166, no. 1, pp. 237–241, 2000.

[114] C. Perkins, T. Ablekim, T. Barnes, D. Kuciauskas, K. Lynn, W. Nemeth, M. O. Reese, S. Swain, and W. Metzger, "Interfaces Between CdTe and ALD Al_2O_3," *IEEE J. Photovolt.*, vol. 8, pp. 1858–1861, Sep 2018.

[115] C. L. Perkins, D. L. McGott, M. O. Reese, and W. K. Metzger, "SnO_2-Catalyzed Oxidation in High-Efficiency CdTe Solar Cells," *ACS Appl. Mater. Interfaces*, vol. 11, no. 13, pp. 13003–13010, 2019.

[116] E. Menéndez-Proupin, G. Gutiérrez, E. Palmero, and J. L. Peña, "Electronic structure of crystalline binary and ternary Cd-Te-O compounds," *Phys. Rev. B*, vol. 70, p. 035112, Jul 2004.

[117] N. Dewan, K. Sreenivas, and V. Gupta, "Properties of crystalline γ-TeO_2 thin film," *J. Cryst. Growth*, vol. 305, no. 1, pp. 237–241, 2007.

[118] S. Guo, Z. Zhu, X. Hu, W. Zhou, X. Song, S. Zhang, K. Zhang, and H. Zeng, "Ultrathin tellurium dioxide: emerging direct bandgap semiconductor with high-mobility transport anisotropy," *Nanoscale*, vol. 10, pp. 8397–8403, 2018.

[119] H. Kroemer, "Nobel Lecture: Quasi-electric fields and band offsets: Teaching electrons new tricks," in *Reviews of Modern Physics*, vol. 73, pp. 783–793, 2001.

[120] H. Kroemer, "Quasi-Electric and Quasi-Magnetic Fields in Non-Uniform Semiconductors," in *RCA Review*, vol. 18, pp. 332–342, 1957.

[121] S. Demtsu and J. Sites, "Effect of back-contact barrier on thin-film CdTe solar cells," *Thin Solid Films*, vol. 510, no. 1, pp. 320–324, 2006.

[122] A. M. Ali, K. Rahman, L. M. Ali, M. Akhtaruzzaman, K. Sopian, S. Radiman, and N. Amin, "A computational study on the energy bandgap engineering in performance enhancement of CdTe thin film solar cells," *Results Phys.*, vol. 7, pp. 1066–1072, 2017.

[123] V. B. Anzin, M. I. Eremets, Y. V. Kosichkin, A. I. Nadezhdinskii, and A. M. Shirokov, "Measurement of the energy gap in tellurium under pressure," *Phys. Status Solidi A*, vol. 42, no. 1, pp. 385–390, 1977.

[124] K. T. Butler, G. Sai Gautam, and P. Canepa, "Designing interfaces in energy materials applications with first-principles calculations," *npj Computational Materials*, vol. 5, no. 19, 2019.

[125] C. G. Van de Walle, "Band lineups and deformation potentials in the model-solid theory," *Phys. Rev. B*, vol. 39, pp. 1871–1883, Jan 1989.

[126] J. Fritsche, D. Kraft, A. Thißen, T. Mayer, A. Klein, and W. Jaegermann, "Band energy diagram of CdTe thin film solar cells," *Thin Solid Films*, vol. 403-404, pp. 252–257, 2002. Proceedings of Symposium P on Thin Film Materials for Photovoltaics.

[127] J. T. Devreese, "Polarons," *arXiv e-prints*, pp. cond–mat/0004497, Apr 2000.

[128] C. Kittel, *Introduction to solid state physics*. Hoboken, NJ: Wiley, 2005.

[129] R. Sarkar, S. Sarkar, A. Pramanik, P. Sarkar, and S. Pal, "Isoelectronically doped CdSe/Te nanoalloys as alternative solar cell materials: insight from computational analysis," *RSC Adv.*, vol. 6, pp. 86494–86501, 2016.

[130] D. Kraft, A. Thissen, J. Broetz, S. Flege, M. Campo, A. Klein, and W. Jaegermann, "Characterization of tellurium layers for back contact formation on close to technology treated CdTe surfaces," *J. Appl. Phys.*, vol. 94, no. 5, pp. 3589–3598, 2003.

[131] D. M. Mattox, *Chapter 2: Substrate ("Real") Surfaces and Surface Modification*. Elsevier Science Direct E-books., Norwich, N.Y: William Andrew, 2nd ed. ed., 2010.

LIST OF ABBREVIATIONS

PV	Photovoltaics
LCOE	Levelized Cost of Energy
GW	Gigawatts
kWh	Kilowatt-Hours
TW	Terawatts
DOE	Department of Energy
CdTe	cadmium telluride
FSLR	First Solar Inc.
VB	Valence Band
CB	Conduction Band
DFT	Density Functional Theory
GF	Green's Function
GB	Grain Boundary
KS	Kohn-Sham
SCF	Self-Consistent Field
LCAO	Linear Combination of Atomic Orbitals
PW	Plane-Wave
XC	Exchange-Correlation
LDA	Local Density Approximation
GGA	Generalized Gradient Approximation
FHI	Fritz-Haber Institute
OMX	OpenMX
PZ	Perdew-Zunger
PBE	Perdew-Burke-Ernzerhof
DOS	Density of States
ECR	Electron Counting Rule
CN	Charge Neutrality
GO	Geometry Optimization
PLDOS	Projected Local Density of States
VBM	Valence Band Maximum
CBM	Conduction Band Minimum
LDOS	Local Density of States
HDP	Hartree Difference Potential
MD	Molecular Dynamics
JV	Current Density vs. Voltage

PUBLICATIONS TO DATE

1. A. P. Nicholson, U. Martinez, A. Shah, A. Thiyagarajan, and W. S. Sampath, “Atomistic modeling of energy band alignment in CdTe(100) and CdTe(111) surfaces,” *Applied Surface Science* **528**, 146832 (2020). https://doi.org/10.1016/j.apsusc.2020.146832.

2. S. A. Pochareddy, A. P. Nicholson, A. Thiyagarajan, A. Shah, and W. S. Sampath, “Structural and Electronic Calculations of CdTe using DFT: Exchange-Correlation Functionals and DFT-1/2 Corrections,” pp. 1-6, 2020 (Submitted to *Journal of Electronic Materials*).

3. A. P. Nicholson, A. H. Munshi, and W. S. Sampath, “First Principles Approach to CdTe/Te Interface Band Alignment Using Density Functional Theory and Nonequilibrium Green’s Function,” *Proceedings of the Photovoltaic Specialist Conference (PVSC), 2018 IEEE 45th*, pp. 1-5, June 2018.

4. A. Nicholson and A. Thiyagarajan (2018). “First Principles Approach to Interface Modeling in CdTe Photovoltaics,” [Invited Talk]. National Renewable Energy Laboratory.

5. A. Nicholson and A. Thiyagarajan (2018). *Density Functional Theory Modeling of Cadmium Telluride Photovoltaics* [Video webinar]. Retrieved from https://www.youtube.com/watch?v=6Ha_yALP-6Q\&feature=youtu.be.

6. A. Nicholson, D. Hemenway, K. Barth, and W. Sampath, “Nucleation and growth of CuCl thin films on commercially available SnO_2 / glass substrates by the sublimation method," *Journal of Vacuum Science and Technology A: Vacuum, Surfaces, and Films* **35**, 041511 (2017).

7. A. Nicholson, “Analysis of CuCl Thin-Film Deposition and Growth by Close-Space Sublimation," Master’s thesis, Colorado State University, Fort Collins, CO, 2016.

8. D. Hemenway, A. Nicholson, K. Barth, and W. Sampath, “Using computational simulation to model CdS/CdTe processing in close-space sublimation," in *Proceedings of the Photovoltaic Specialist Conference (PVSC), 2015 IEEE 42nd*, pp. 1-6, June 2015.